University of Southampton

Faculty of Natural and Environmental Sciences

School of Ocean and Earth Science

Iron Speciation in Hydrothermal Plumes

by

Jeffrey Alistair Hawkes

Thesis for the degree of Doctor of Philosophy

September 2013

UNIVERSITY OF SOUTHAMPTON

ABSTRACT

FACULTY OF NATURAL AND ENVIRONMENTAL SCIENCES

Ocean and Earth Science

Doctor of Philosophy

IRON SPECIATION IN HYDROTHERMAL PLUMES

by Jeffrey Alistair Hawkes

This thesis considers the speciation of the transition metal iron (Fe) in hydrothermal vent plumes. Hydrothermal inputs have recently been recognised as important in the oceanic cycling of Fe, but understanding of the chemical forms of Fe in hydrothermal plumes remains very limited. By considering the abundance and distribution of various size and reactivity fractions of Fe in plumes it is possible to better constrain the true impact that hydrothermal Fe may have on ocean biogeochemistry.

A reverse titration voltammetric technique was developed to determine Fe binding ligands in seawater when ligands were over-saturated by high concentrations of Fe, and Fe binding ligands and Fe size fractions were assessed in two hydrothermal plumes in the Southern Ocean. The results indicated that at least 7.5% of total vented hydrothermal Fe was present in association with labile complexes in the plume, which may have been organic, inorganic or mixed in their nature. These complexes would be available for transport into the deep ocean, representing an important source of bioavailable Fe to marine environments. A large portion of Fe in the plumes was in the colloidal size fraction, leading to the conclusion that weak colloidal flocculates are important in the distribution of hydrothermal Fe.

The distribution and speciation of Fe was assessed in an island arc caldera. Fe oxy-hydroxide colloids were important in this environment, suggesting that the acid rich and often shallow hydrothermal venting found at island arcs should provide Fe as a micronutrient to surface waters. The interaction of Fe and several elements was assessed in the particulate phase in the three vent environments. Oxyanion (e.g. phosphorus) scavenging with Fe oxy-hydroxides was increased in the island arc and sulfide dominated vent sites, suggesting that factors other than phosphate concentration, such as Fe oxidation rate, could be important in how hydrothermal Fe oxy-hydroxides interact with seawater.

Contents

List of Figures

List of Tables

0.1 Author's declaration

I, Jeffrey A. Hawkes, declare that the thesis entitled "Iron Speciation in Hydrothermal Plumes" and the work presented in the thesis are both my own, and have been generated by me as the result of my own original research. I confirm that:

- this work was done wholly or mainly while in candidature for a research degree at this University;
- where any part of this thesis has previously been submitted for a degree or any other qualification at this University or any other institution, this has been clearly stated;
- where I have consulted the published work of others, this is always clearly attributed;
- where I have quoted from the work of others, the source is always given. With the exception of such quotations, this thesis is entirely my own work;
- I have acknowledged all main sources of help;
- where the thesis is based on work done by myself jointly with others, I have made clear exactly what was done by others and what I have contributed myself;
- parts of this work have been published separately as follows:

"Characterisation of iron binding ligands in seawater by reverse titration",

J. A. Hawkes, M. Gledhill, D. P. Connelly and E. P. Achterberg,

Analytica Chimica Acta **766**, 1412 (2013), pp. 53-60;

"The stabilisation and transportation of dissolved iron from high temperature hydrothermal vent systems",

J. A. Hawkes, D. P. Connelly, M. Gledhill and E. P. Achterberg,

Earth and Planetary Science Letters, **375** (2013), pp. 280-290.

In which my contribution was the development and handling of the reported analytical work, sample analysis, writing the papers with advice from the co-authors, producing the figures and leading the responses to the peer reviews.

Signed .....

Date .....

0.2 Acknowledgments

There are dozens of people to thank for their help throughout the production of this work, and I am indebted to all of them. My warmest thanks go to Eric Achterberg and Doug Connelly, who have been fantastic supervisors with brilliant complementary skills and a shared infectious enthusiasm for marine chemistry. More specifically I'd like to thank Eric for his encouragement and criticism of my written work and Doug for his hands-on attitude to the practical and sea-going side of the project, and for letting me win the occasional game of Scrabble at sea. Martha Gledhill, my pseudo-supervisor, has been an incredible source of motivation and thought-provoking ideas, and the direction of the project would not have been the same without her. Rachael James has provided excellent support and advice as the chair of my advisory panel.

I've been lucky enough to go to sea four times over the last few years, and for giving me these opportunities and for their tremendous leadership at sea I thank Paul Tyler, Alex Rogers, Jon Copley and Doug Connelly. I also thank the rest of the scientists, crew and ROV teams on these cruises (JC042, JC055, JC080 and JC082) for their help and motivation, and for making these voyages such fun.

This project has involved a lot of lab work, and the data would not have been produced without the help and advice of several people - in particular Darryl Green, Andy Milton, Matt Cooper, Carla Sands, Cathy Cole and Lizeth Avendaño. Veerle Huvenne has always been a very generous source of help with software and the provision of maps, thank you. I also thank Fred Mosselmans and Tina Geraki at the Diamond Light Source, Caroline Peacock for her advice with XAFS, Richard Pearce from the SEM laboratory at NOCS, and our Master's student Jack Hitch for all his help with spectroscopic characterisation.

I've benefitted greatly from scientific discussions and collaborations with many people, but I'd like to give special thanks to Cathy Cole, Will Homoky, Laura Hepburn, Rich Pancost, Will Reid, Alfred Aquilina, Jon Copley and Rachel Mills, in no particular order. Other, non-Ph.D. related activity has kept me happy, healthy and entertained, and I'm grateful (to name a few such activities) to everyone involved in the NOCS five-a-side football team, the coffee gang and the PG chronicle.

Finally, and perhaps most importantly, I thank my family (led by Zaza and her hens) for their life-long support of everything I've ever chosen to do. I owe my education to my parents and my primary school teacher, P.C., and I probably would never have been interested in science if not for my inspirational dad. I also thank Yoli for keeping me happy and distracted (when needed) during the final stages of writing this thesis.

0.3 Definitions and common abbreviations

Fe	Iron
DFe, PFe, CFe, SFe	Dissolved Fe, particulate Fe, colloidal Fe, soluble Fe
Fe'	Inorganic Fe
$\alpha_{Fe'}$	Inorganic Fe:free Fe^{3+} ratio
$\mathbf{Fe_{NN}}$	Fe bound to NN
$\mathbf{Fe_{NNmax}}$	Maximum Fe in a sample able to bind with a defined concentration of NN.
L	(Organic) ligand
AL	Added ligand
NN	1-nitroso-2-naphthol
$K'_{\mathbf{Fe^{3+}L}}$	Stability constant of the equilibrium between free Fe, L and FeL.
dFOB	Desferrioxamine B
(RT)-CLE-ACSV	(Reverse titration)-cathodic ligand exchange - adsorptive cathodic stripping voltammetry
i_p	Current
i_{pmax}	Maximum current in titration
$\mathbf{H_2S}$	Hydrogen sulfide
NPD sulfide	Non-purgeable dissolved sulfide
HMDE	Hanging mercury drop electrode
UVSW	Ultra violet radiation treated seawater
LDPE/HDPE	Low/high density polyethylene
PTFE	Polytetrafluoroethylene
SEM	Scanning electron microscopy
XRF	X-Ray fluorescence
XAFS	X-Ray adsorption fluorescence spectroscopy

SD	Standard deviation
LoD	Limit of detection
MAR	Mid Atlantic Ridge
EPR	East Pacific Rise
ESR	East Scotia Ridge
MOR	Mid-ocean ridge
BAB	Back-arc basin
E1-E10	Segments of the East Scotia Ridge
E2, E9N	Vent fields on the East Scotia Ridge
ICP-MS	Inductively coupled plasma - mass spectrometry
CTD profiler	Conductivity, temperature and depth profiler
ROV	Remotely operated vehicle
OTE bottle	Ocean Test Equipment bottle
SAPS	Stand Alone Pump System
LSS	Light scattering sensor
Eh	Reductive potential
M (nM, μM, mM)	Moles per kilogram, (nano-, micro-, milli-)
HCl	Hydrochloric acid
HNO_3	Nitric acid
REE	Rare earth elements
DIC	Dissolved inorganic carbon
DOC	Dissolved organic carbon

Chapter 1

Introduction

Contents

1.1 Introduction

Iron (Fe) is one of the most important elements in seawater as it is intricately linked with primary production as a dissolved micronutrient and with the co-precipitation and scavenging of several other elements into particulate phases. It therefore plays an important role in controlling marine elemental and biotic concentrations. The equilibrium conditions of Fe in seawater along with the available sources and sinks of Fe dictate concentrations, speciation (i.e. the chemical form of the element) and redox states, all of which control its microbiological availability (Hutchins et al., 1999; Rich and Morel, 1990; Shaked et al., 2005; Shaked and Lis, 2012; Wells, 1999). In areas with significant inputs of Fe (e.g. rivers, hydrothermal plumes, surface waters exposed to atmospheric dust deposition), the kinetics of Fe species formation and precipitation control the immediate fate of Fe and many other elements and compounds which interact with this metal.

Even though the understanding of Fe speciation and concentration in seawater is crucial to marine biogeochemistry, the tools necessary for this understanding have only recently been developed (over the last 20 years). This is largely due to the experimental difficulty of analysing Fe, which firstly is prone to contamination and secondly is greatly affected by pH, temperature and interaction with oxygen and organic matter - all of which can be difficult to control. This chapter describes the current understanding of Fe speciation in oceanic waters and the most recent attempts to assess the impact that hydrothermal activity has on the oceanic Fe cycle. First, I will introduce the concept of hydrothermal circulation as a source of Fe to the ocean.

1.2 Hydrothermal circulation and leaching of iron from host rocks

Hydrothermal circulation generally occurs around spreading centres of the Earth's crust; in mid-ocean ridges and back-arc basins (Figure 1.1). Deep ocean water percolates into cracks in volcanically formed pillow basalt, where it penetrates the crust

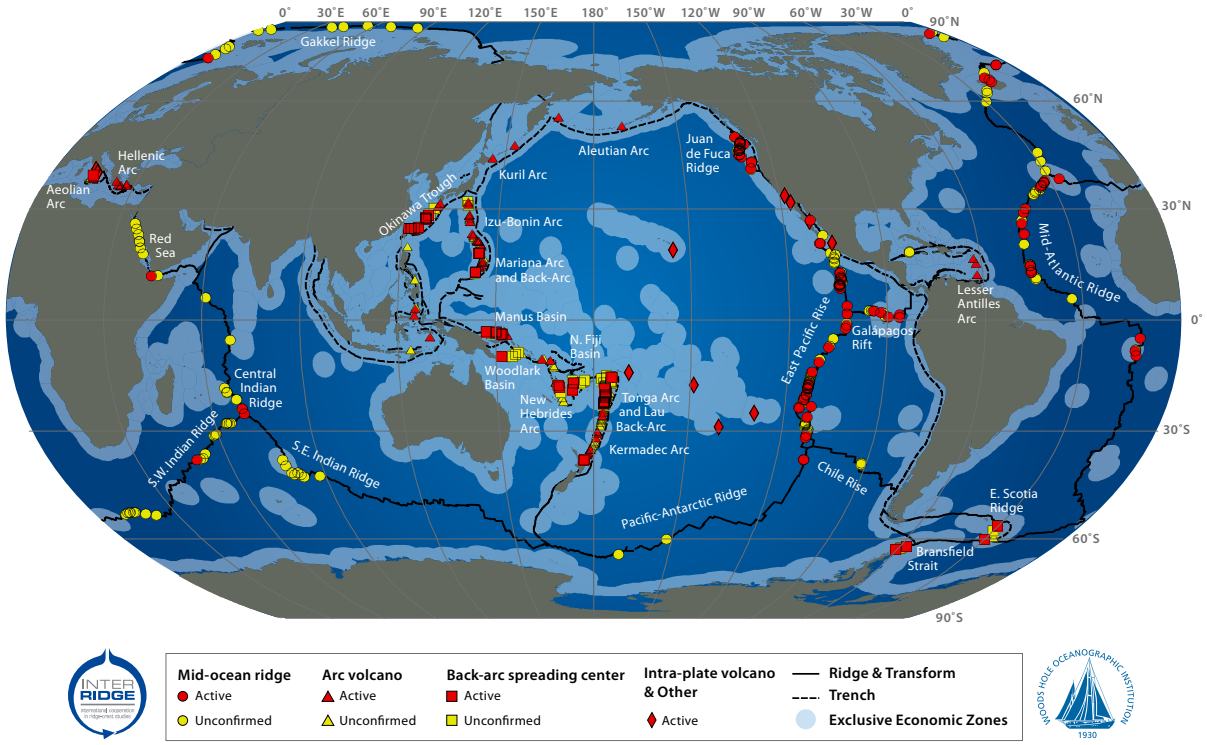

Figure 1.1: Locations of visually confirmed vent sites (red) and unconfirmed sites that have been found by water column anomalies (yellow). The South Atlantic Ocean and global high latitude areas are under-represented due to lack of exploration. From the InterRidge society (http://www.interridge.org).

and is exposed to the thermal influence of magma outcrops, which conductively heat the seawater and rock mixture to estimated temperatures of 450°C, allowing hydrothermal alteration of both phases in what is referred to as the 'reaction zone'. Alkalinity is lost, primarily through formation of anhydrite and smectite; processes which strip sulfate and magnesium from the water, respectively (Alt, 1995). This leaves the fluid highly protonated, with in situ pH levels of around 5-6 (German and Von Damm, 2004). The resulting acidity and temperature allows the dissolution of many metals from the host rocks. Of particular note are iron and manganese, which can be 10^6:1 enriched over deep seawater concentrations (Landing and Bruland, 1987; Statham et al., 1998; Von Damm, 1995), and the 'rare earth elements' (REEs), which are also highly enriched (Campbell et al., 1988; Michard et al., 1983). Volatile gases - primarily methane, carbon dioxide, helium-3 and hydrogen sulfide

are incorporated through a combination of magmatic degassing, inorganic synthesis and leaching from host rocks (Butterfield and Massoth, 1994; Kelley, 1996; Kelley and Fruh-Green, 2000; Lilley, 1993; Welhan and Craig, 1983; Welhan, 1988).

Phase separation of seawater can occur in the reaction zone, if the critical temperature/pressure point is passed. At typical hydrothermal vent depths (2000-3000 m), phase separation of seawater occurs above 400℃ (Bischoff and Rosenbauer, 1985). Under these conditions the fluid separates into a 'vapour' phase, rich in volatiles and a 'brine' phase, where chloride concentrations are higher, stabilising a higher portion of cations (German and Von Damm, 2004). Chloride makes up the majority of the anionic content of the water, as it is the only major anion not incorporated into minerals during hydrothermal alteration. No hydrothermal vents are known which do not show evidence of some phase separation, as made apparent by chloride concentrations, which are always different to seawater in hydrothermal fluids. Iron is thermodynamically more stable in the brine phase than the vapour phase due to the availability of chloride as an inorganic ligand.

Hydrothermal circulation returns to seawater when the fluid reaches sufficient buoyancy to force its way upwards through the crust and into the deep ocean. This happens dramatically in the case of 'black smokers', which are focussed points of hydrothermal discharge resulting in large mineral chimneys, as the reduced hydrothermal fluids (∼350℃) rapidly cool upon contact with cold, oxic seawater (<2℃). The rapid temperature drop results in the precipitation of large concentrations of reduced iron, copper and zinc, which form sulfide minerals (pyrite, sphalerite, etc.) with dissolved sulfide under the more oxidising, colder, higher pH conditions.

The discharge flux of hydrothermally altered seawater is thought to be more substantial in widespread areas of lower temperature diffuse flow, around the edges of the black smokers and on the ridge flanks of the axial spreading (i.e. in crust up to 65 Ma old; Mottl and Wheat, 1994). However, the impact of these regions on the oceanic Fe cycle is likely to be less important as the temperature and acidity of the fluids is not sufficient to mobilise Fe to such a large extent from host rocks, and the lower buoyancy of the fluids mean the hydrothermal effluent does not rise as high

in the water column for further distribution.

In high temperature hydrothermal fluids, Fe concentrations can range from 2 - 24,000 μM (the latter at Rainbow, MAR; cf. typical deep ocean water Fe <1 nM), and the large range in concentrations are the result of complex interactions between physical factors such as temperature and host geology with chemical factors such as pH, phase separation and concentrations of other ions and gases (see Chapter 2). The concentration of hydrogen sulfide and rival chalcophilic elements (copper and zinc) control the immediate fate of Fe upon contact with seawater, as the formation of FeS and FeS_2 provide an almost immediate sink of hydrothermal Fe into a kinetically stable solid phase (Hsu-Kim et al., 2008; Klevenz et al., 2011; Yücel et al., 2011). The remaining reduced Fe that escapes this first mass precipitation is subjected to the more typical chemical controls of cold, oxygenated seawater (Field and Sherrell, 2000; Mottl and McConachy, 1990). A large portion of hydrothermal circulation therefore only represents an alteration of solid phase Fe through a very brief mobilisation in a hot, acidic aqueous phase. However, high temperature hydrothermal flux is sufficiently large and typical seawater Fe concentrations are sufficiently low that even a small escape of Fe into the operationally defined 'dissolved' phase (usually <0.2 μm in size) would have a measureable impact on global Fe biogeochemistry (Bennett et al., 2008; Tagliabue et al., 2010).

1.3 The behaviour of iron in seawater

1.3.1 Redox controls on iron and inorganic speciation

Iron has two oxidation states, +2 and +3, which are close enough in energy (E_0 = 0.77 V) to both be important in the marine environment. In oxygenated seawater, Fe is almost exclusively present as Fe(III) (where the term 'Fe(III)' represents all inorganic species in seawater with an iron centre that has oxidation state +3). In environments with low oxygen (oceanic oxygen minimum zones, sediment pore waters, hydrothermal vent fluids), Fe(III) is chemically or biologically reduced to Fe(II) (Froelich et al., 1979; Pohl and Fernandez-Otero, 2012). Irradiation of seawater by

sunlight can also reduce Fe(III) to Fe(II) in oxygenated surface waters (Kuma et al., 1995, 1992; Pohl and Fernandez-Otero, 2012).

Fe(II) in pH 8 seawater is composed of free (76%) and carbonated (23%) Fe^{2+}. The other 1% of Fe(II) is complexed by hydroxyl, carbonate and bicarbonate ligands (Millero et al., 1995). At lower pH (i.e. in hydrothermal vent fluids), free Fe^{2+} represents a greater portion of total Fe(II), although in most natural marine anoxic environments the presence of sulfide and bisulfide have a great affect on Fe^{2+} speciation (Hsu-Kim et al., 2008; Luther et al., 2003; Rickard et al., 1999).

Free Fe^{3+} is insignificant in seawater, and represents roughly $1{:}10^{10}$ of Fe(III) species at pH 8 (Croot and Johansson, 2000; Kuma et al., 1996; Millero et al., 1995). Fe(III) is almost entirely complexed by hydroxyl ligands (OH^-) at seawater pH, as $[FeOH]^{2+}$, $[Fe(OH)_2]^+$, $Fe(OH)_3$ and $[Fe(OH)_4]^-$. At typical seawater pH (7.9 - 8.0), $[Fe(OH)_2]^+$ is the dominant aqueous species. $Fe(OH)_3$ is insoluble and precipitates in an amorphous morphology which later crystallises as ferrihydrite, goethite and other 'oxy-hydroxide' minerals. The solubility of Fe(III) in water of various ionic strengths, temperatures and acidities can be described using laboratory determined formation constants of the hydrolysis species (Liu and Millero, 2002; Appendix A).

1.3.2 Organic ligands and the organic speciation of Fe

The concentration of Fe(III) in seawater far exceeds its calculated theoretical solubility (Kuma et al., 1996; Liu and Millero, 2002), and this is due to the presence of strong Fe binding organic ligands which buffer the Fe(III) from the formation of insoluble $Fe(OH)_3$ oxy-hydroxides. The routine method for characterising Fe binding ligands in seawater is competitive ligand exchange - adsorptive cathodic stripping voltammetry (CLE-ACSV), which was first achieved for Fe(III) by Gledhill and van den Berg in 1994. In this procedure, a competition for Fe is established between an added, electroactive ligand (AL), the natural organic ligands in the sample and the natural inorganic ligands (i.e. hydroxyl groups). Iron is added as a titrant, and the concentration of Fe-AL is measured by stripping voltammetry. The concentration

and Fe binding strength of excess natural organic ligands can be inferred by consideration of the equilibrium (Croot and Johansson, 2000; Gledhill and van den Berg, 1994; Rue and Bruland, 1995).

Using this method, Fe binding organic ligands (L) have been found in many surface and deep waters, with FeL stability constants ($K'_{Fe^{3+}L}$) ranging from 10^{19}-10^{24} (see Gledhill and Buck, 2012 for comprehensive summary of results). Kinetic variations of the stripping voltammetry experiments have found similar stability constants ($K'_{FeL} = K_f/K_d$) for the FeL complexes (Gerringa et al., 2007; Witter and Luther, 1998; Wu and Luther, 1995). Some studies have advocated the presence of two distinct ligands classes: 'L_1' and 'L_2' (Cullen et al., 2006; Rue and Bruland, 1995, 1997), while others suggest that FeL complexes are more likely to be present in a continuum of stabilities (Hassler et al., 2013; Hiemstra and van Riemsdijk, 2006; Van Den Berg, 1995). Stronger ligands are generally thought to be biological in origin, present only in the surface mixed layer, and possibly produced strategically by microbial organisms to maintain Fe concentrations (e.g. chatecolate and hydroximate siderophores; Gledhill and Buck, 2012). The weaker ligands are thought to be more pervasive, and may be constituted by humic acids and other terrestrial substances (Hunter and Boyd, 2007; Kondo et al., 2012; Laglera and van den Berg, 2009) or high concentrations of large, weak Fe binding molecules such as polysaccharides (Aluwihare and Repeta, 1999; Cullen et al., 2006; Gerringa et al., 2007).

Some studies have considered the range of sizes of both Fe species and organic ligands in seawater (Bergquist et al., 2007; Boye et al., 2010; Cullen et al., 2006; Wu et al., 2001), usually finding that both Fe and L are more highly concentrated in an operationally defined colloidal fraction (typically 0.02 - 0.4 μm) than in the corresponding 'soluble' fraction (<0.02 μm). These studies suggest that 'FeL' complexes in natural environments may include aggregations of inorganic and organic ligands with Fe(III) in amorphous colloids, a theory that was championed very early in the voltammetric investigation of Fe speciation by Mackey and Zirino (1994). These workers suggested that the labile Fe measured by the CLE-ACSV procedure might in fact be stripped from these aggregates over the course of the equilibration period

of the method rather than being distinct FeL complexes.

The importance of Fe as a micronutrient (Martin and Fitzwater, 1988) has led several researchers to investigate the bio-availability of the various Fe species described above. 'Reductive uptake' of Fe(III) appears to be an important mechanism for the acquisition of Fe by phytoplankton (Shaked and Lis, 2012), and both FeL phases and Fe(III) colloids can provide nutrition to primary producers (Chen et al., 2003; Hassler and Schoemann, 2009; Morel et al., 2008).

1.4 Iron in hydrothermal plumes and introduction to the thesis

1.4.1 Iron oxy-hydroxide particle formation

After the initial dispersal of hydrothermal material into seawater and removal of dissolved hydrogen sulfide, the remaining Fe^{2+} may be oxidised to Fe^{3+} and both Fe(II) and Fe(III) are subjected to coordination reactions with inorganic and organic ligands. Although some studies have shown that Fe(II) particles may be transported away from vent sites (Toner et al., 2009; Yücel et al., 2011), Fe(III) particles are generally more common in hydrothermal plumes (Feely et al., 1996; Field and Sherrell, 2000). The oxidation of hydrothermal Fe(II) to Fe(III) is of critical importance to the chemistry of hydrothermal plumes as the gradual formation of Fe(III) oxy-hydroxide phases leads to the co-precipitation and scavenging of many dissolved elements including oxyanions such as phosphorus, vanadium and uranium (Edmonds and German, 2004; Feely et al., 1991) and the rare earth elements (German et al., 1990; Klinkhammer et al., 1983). Hydrothermal activity has thus been shown to have a significant impact on the dissolved concentrations of these elements in ocean waters (Elderfield and Schultz, 1996; German et al., 1990; Wheat et al., 1996).

The rate of oxidation of Fe(II) depends on dissolved oxygen concentration, temperature, pH (and $p[OH]^-$) and solution ionic strength (Millero et al., 1987) according

to pseudo first-order equation:

$$\frac{-d[\mathrm{Fe(II)}]}{dt} = k_1[\mathrm{Fe(II)}] \tag{1.1}$$

Where

$$k_1 = k[\mathrm{O_2}][\mathrm{OH^-}]^2 \tag{1.2}$$

$$\log k = \log k_0 - 3.29\mathrm{I}^{1/2} + 1.52\mathrm{I} \tag{1.3}$$

$$\log k_0 = \mathrm{l}21.56 - 1545/\mathrm{T} \tag{1.4}$$

Where I is the ionic strength and T is the temperature in degrees Kelvin. In hydrothermal plumes, the pseudo first order oxidation half life of Fe(II) varies between 2.1 minutes to 6 hours depending on the ocean basin (Field and Sherrell, 2000; Rudnicki and Elderfield, 1993; Statham et al., 2005; Wang et al., 2012).

1.4.2 Iron(III) 'stabilisation' by organic ligands and in colloids

Hydrothermal vents have only recently been considered as an important source of Fe to the ocean due to work by Bennett et al. (2008) who showed that Fe was complexed by organic ligands on the edges of hydrothermal plumes, preventing the loss of a small portion of hydrothermal Fe to oxy-hydroxide phases. Before this, all hydrothermal Fe was presumed to precipitate as sulfides or $Fe(OH)_3$ and settle from hydrothermal plumes (Feely et al., 1987; German et al., 1990; Mottl and McConachy, 1990). Colloidal forms of Fe (including organic and inorganic colloids) may also allow transport of some hydrothermal Fe (Sands et al., 2012; Yücel et al., 2011), and several researchers have suggested that deep ocean Fe anomalies are caused by the distribution of hydrothermal Fe off-axis (Klunder et al., 2012; Kondo et al., 2012; Nishioka et al., 2013; Tagliabue et al., 2010; Wu et al., 2011).

This thesis addresses the speciation, distribution and fate of Fe in the hydrothermal plumes of three recently discovered vent sites in the Southern Ocean. The sites, which are described in Chapter 2, are two fairly typical back-arc basin vent sites (E2

and E9N; Rogers et al., 2012; James et al., in prep.) and an extremely sulfidic island arc volcano caldera (Kemp Caldera; Connelly et al., in prep.). Several methods have been used to elucidate the concentration, speciation and size fractionation of this crucial element in a range of samples, and the variation of Fe is compared with other hydrothermal and seawater derived elements in order to compare the impact of Fe in these newly discovered sites with that described elsewhere previously in the literature.

1.4.3 Introduction to the thesis

In Chapter 2 I briefly describe the geology and geochemistry of the hydrothermal vent sites and fluids studied in this thesis. This provides context for the other results, considering that hydrothermal venting is so varied globally. Chapter 3 outlines the reverse titration - competitive ligand exchange - adsorptive cathodic stripping voltammetry technique, which was developed for the analysis of Fe speciation in high Fe environments. This technique was used in conjunction with size fraction analysis in Chapter 4 to examine Fe speciation in the hydrothermal plumes of the East Scotia Ridge. In Chapter 5, Fe speciation the Kemp Caldera island arc hydrothermal system is described and discussed, and in Chapter 6 the hydrothermal precipitates of all three sites are described and discussed. The chapters together provide a wide-ranging analysis of the forms of Fe in hydrothermal environments, and each chapter aims to consider the results presented in a global context, thus improving the understanding of the impact that hydrothermal Fe may have on global marine biogeochemistry.

Chapter 2

Study Areas

Contents

2.1 Introduction

Three vent sites were sampled for this work, all in the Scotia Sea in the Atlantic sector of the Southern Ocean (Figure 2.1). The vent sites are referred to throughout this work as 'E2', 'E9N' and the 'Kemp Caldera'. The E2 and E9N vent sites are located on the East Scotia Ridge, a back arc spreading centre, which is comprised of ten spreading segments named E1-E10 (Leat et al., 2004). The E2 and E9 segments are the only two that have been visually observed to host high temperature hydrothermal activity (Rogers et al., 2012), and the vent sites were named after the ridge segment names (divided into north and south sites at E9). The Kemp Caldera was discovered in 2009 on the shoulder of the Kemp Seamount (Larter and others, in prep.), an island arc seamount situated ∼50 km west south west of Thule Island, the southernmost island of the South Sandwich island arc. Island arc hydrothermal activity is generally distinguished from spreading centre activity by stronger magmatic influence, which leads to more acidic and gaseous fluids (Baker et al., 2008; Butterfield et al., 2011; de Ronde et al., 2005, 2011; Leybourne et al., 2012; Resing et al., 2009). This chapter aims to give a brief geological description of the sites and to compare their vent fluid compositions with other published data in order to give an impression of how typical the sites are in a global context.

2.2 Geological setting

2.2.1 E2 and E9 on the East Scotia Ridge

The East Scotia Ridge (ESR) is a back-arc spreading centre running north to south between the Scotia Plate and the narrow and young South Sandwich Plate in the Atlantic sector of the Southern Ocean (Figure 2.1B). Spreading at the ESR was initiated over 15 Ma ago (Leat et al., 2004) and is currently proceeding at an intermediate rate of 65-70 mm yr^{-1} (Bruguier and Livermore, 2001). The ESR is made up of ten second-order ridge segments, designated E1-E10, which are offset (in the east-west direction) by non-transform discontinuities. The northern and southern ends of the ESR are influenced by slab edge subduction of the South American

Plate and Antarctic Plate and increased mantle interaction, changing the magmatic composition (Leat et al., 2000, 2004; Livermore, 2003). The E2 and E9 segments are distinguished from the other segments by being elevated to ∼2500 m depth by volcanic inflation (Leat et al., 2004). E3-E8 have deep rift valley floors, and the seafloor is generally deeper than 3500 m (c.f. E2 ∼2600 m, E9N ∼2400 m). The E2 and E9 segments are also noteworthy as they are, or have been, underlain by axial magma chambers, as shown by seismic reflection (Bruguier and Livermore, 2001; Livermore et al., 1997). The ESR hosts a relative low abundance of hydrothermal activity, possibly due to the distance of most of the ridge from the subduction arc (Baker et al., 2005). High temperature hydrothermal vent sites with black smoker chimneys and faunal assemblages have been observed and sampled at both E2 and E9 (north and south; Rogers et al., 2012) after initial discovery of hydrothermal plumes a decade previously (German et al., 2000).

The E2 site (located at 56.089°S, 30.317°W) is bathymetrically rough with large vertical displacements running north to south (Figure 2.2A). The E9N site (located at 60.043°S, 29.982°W) is comparatively flat (Figure 2.2B) and represents a local topographic elevation, a result of magmatic inflation in the centre of the ridge (Bruguier and Livermore, 2001).

2.2.2 The Kemp Caldera on the South Sandwich island arc

The Kemp Caldera is situated at 59.700°S, 28.317°W and is a volcanic caldera on the South Sandwich island arc (Figure 2.1A). It has a maximum depth of 1600 m and diameter of 7 km (Larter and others, in prep.). The caldera rim is roughly circular and the caldera contains a resurgent cone rising ∼250 m from the caldera floor (Figure 2.3). Hydrothermal venting was discovered on the east south-eastern flank of the resurgent cone, and mainly consisted of diffusive, sulfur rich areas of roughly 20-30℃ fluid (background temperature 0.2℃). Several higher temperature 'white smoker' features were found venting fluids up to 212℃ (Connelly and others, in prep.).

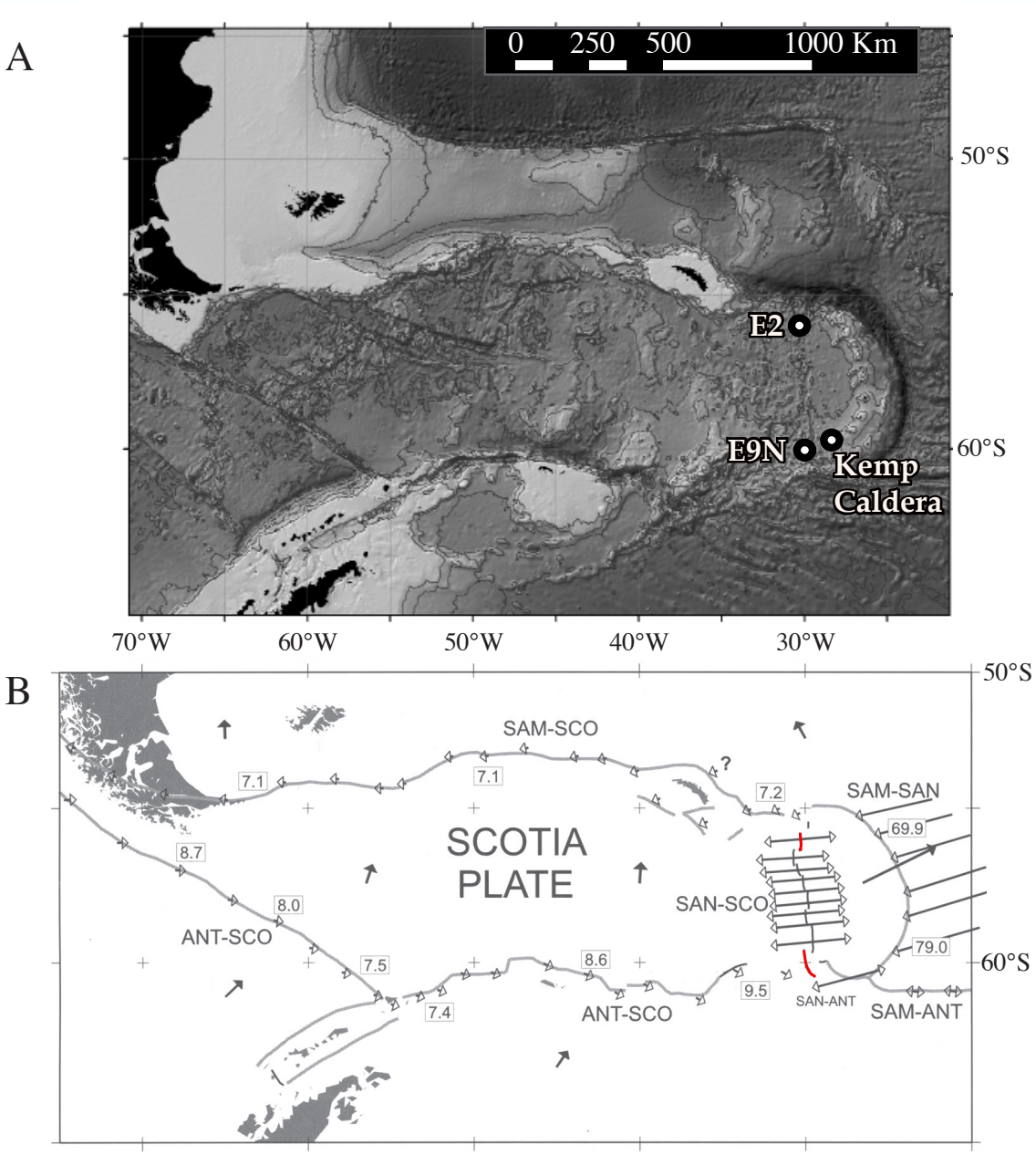

Figure 2.1: A: Location of the E2, E9N and Kemp Caldera vent sites in the eastern Scotia Sea, Southern Ocean. B: Map of tectonic plates surrounding the Scotia Sea (adapted from Livermore, 2003 and Thomas et al., 2003). The motions of the plates are indicated by open arrows (relative movements compared with the Scotia Plate, rates shown as numbers in boxes in mm yr^{-1}) and closed arrows (absolute movements). SAM = South American Plate, ANT = Antarctic Plate, SAN = Sandwich Plate, SCO = Scotia Plate. The E2 and E9 segments of the ESR are highlighted in red.

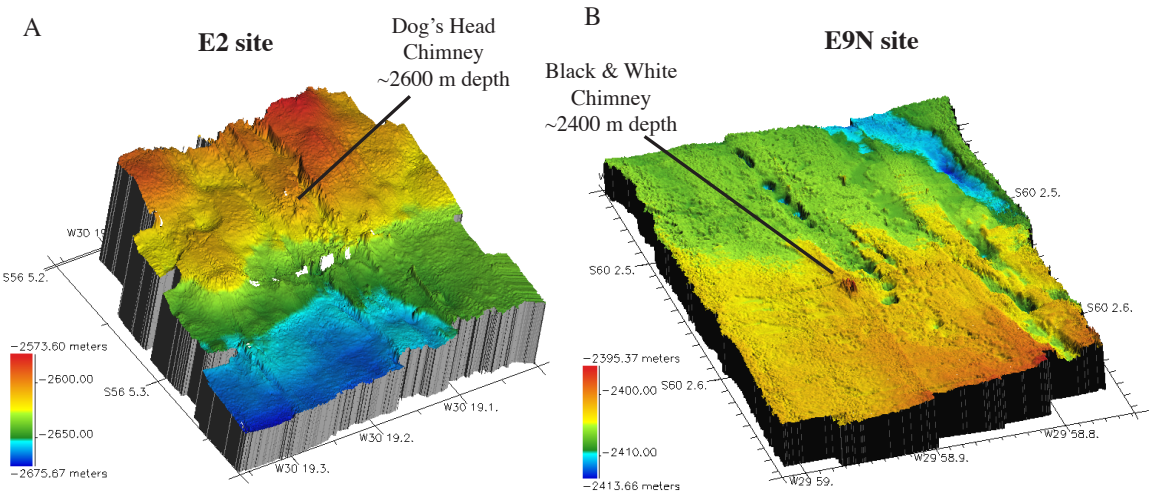

Figure 2.2: Bathymetry of the East Scotia Ridge vent sites. A: E2 with the Dog's Head Chimney location indicated, B: E9N with the Black & White Chimney location indicated.

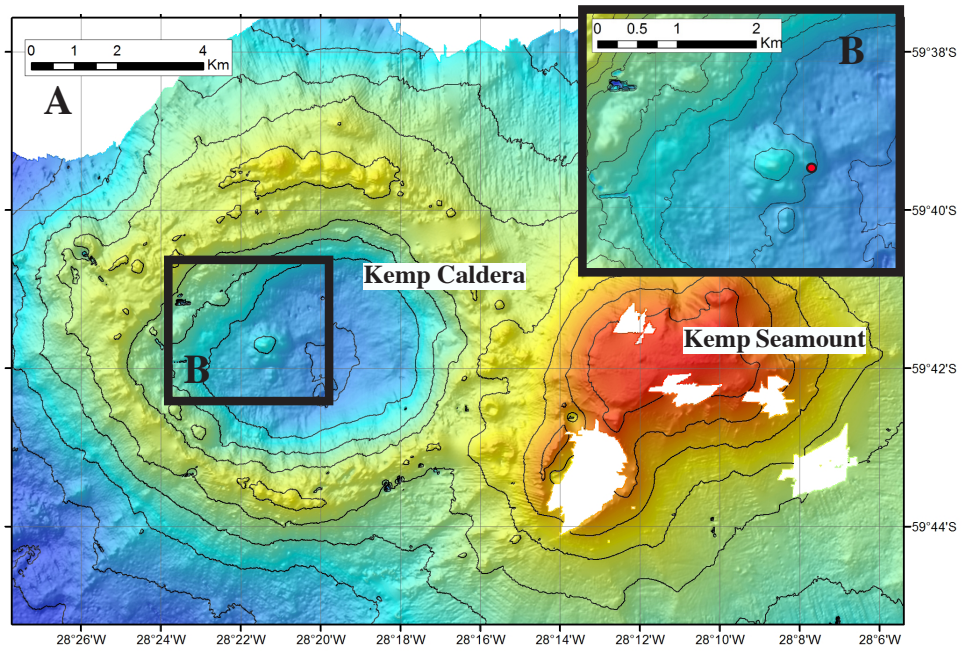

Figure 2.3: Bathymetry of the Kemp Caldera site (maximum depth ∼1600 m). A: The Kemp Caldera vent site location on the side of the Kemp Seamount, B: Expanded view of the resurgent cone, with the location of hydrothermal activity marked by a red dot.

2.3 Vent fluid composition and water masses

2.3.1 E2 and E9N

At the time of sampling (see James et al., in prep.), the E2 and E9N vent fluids had intermediate Fe concentrations in a global context (Figure 2.4). The hydrogen sulfide concentrations were high (Figure 2.4B), likely due to the influence of the fluid/volatile rich subduction plate on the mantle - a process typical at back arc spreading centre sites (Gamo et al., 2006; Ishibashi et al., 1995; Mottl et al., 2011; Yang and Scott, 2002). At E9N, a vapour phase was sampled, as demonstrated by depleted chloride concentrations (Figure 2.4D). This diminishes the metal (e.g. Fe) carrying capability of the fluid, and leads to higher concentrations of volatiles (such as H_2S; Von Damm, 1990). The fate of Fe in hydrothermal venting environments is initially controlled by H_2S (Mottl and McConachy, 1990), and a greater proportion of Fe should be precipitated as sulfides from the E9N (vs. E2) fluids upon entry into seawater. There is also some evidence of sub-surface cooling of the fluids at E2 (James et al., in prep.) which led to a sub-surface loss of Fe and possibly some stabilisation of Fe (as nano-particulate sulfides?) in the fluids - few particulate Fe dregs were found in the samplers at E2 in comparison with E9N. Overall, the two sites vent more sulfidic, hotter fluids than 'average', but given the global range of [Fe], [H_2S], pH and other important vent fluid constituents, the vent sites may be considered typical (not extreme) examples of hydrothermal venting (Figure 2.4).

The two vent sites are situated in similar water masses, which are mixtures of Weddell Sea Deep Water (WSDW) and Lower Circumpolar Deep Water (LCDW) (Figure 2.5). Summaries of the major vent fluid and seawater compositions are presented in Table 2.1.

2.3.2 The Kemp Caldera

The samples taken from the Kemp Caldera sites were not pure end-member fluids, and contained a minimum of 74-80% seawater based on magnesium and sulfate con-

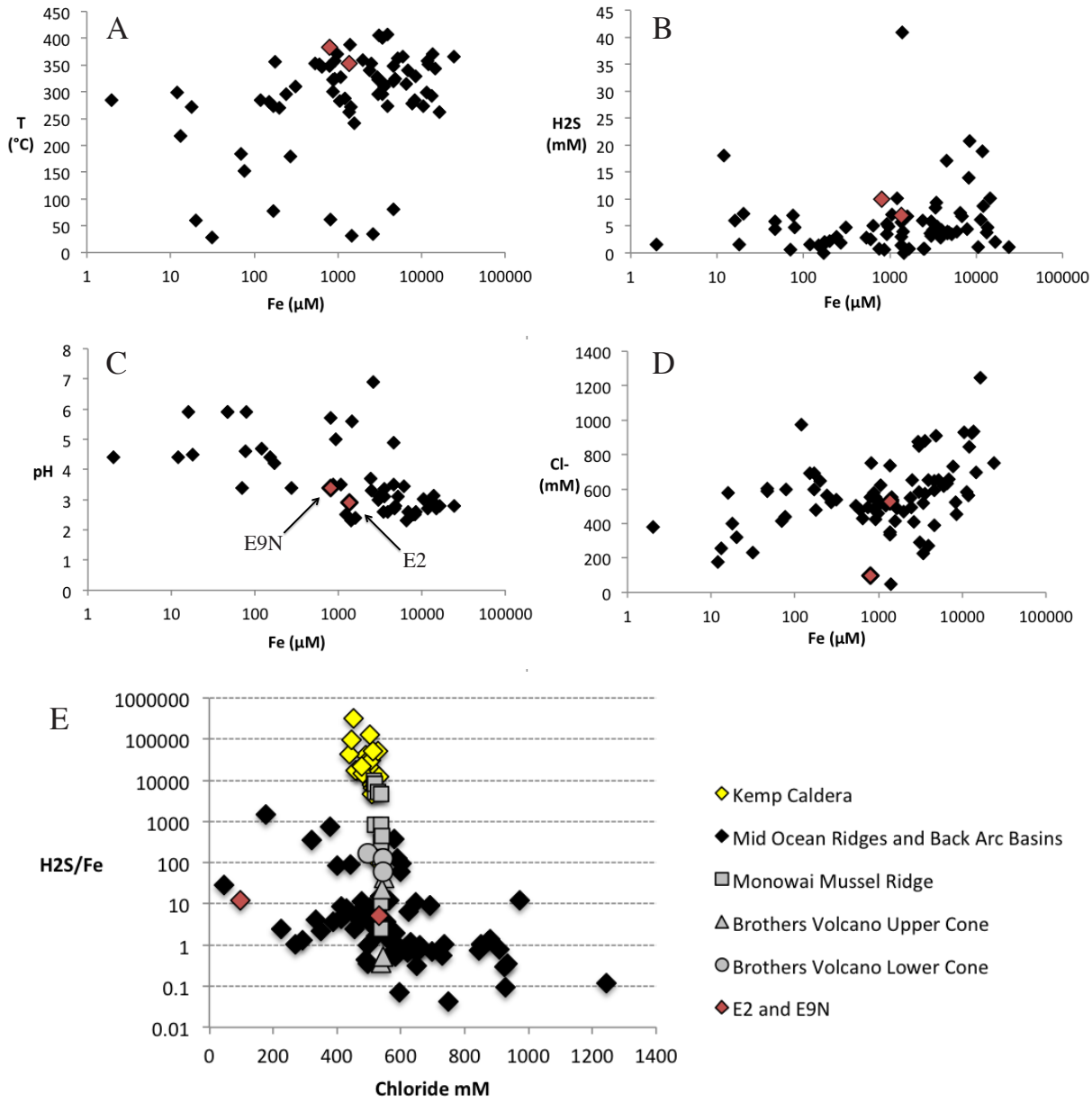

Figure 2.4: The compositions of the E2, E9N and Kemp Caldera vent fluids compared with reported values from other vent sites. A-D: Temperature, H_2S, pH and Cl^- for mid ocean ridge (MOR) and back-arc basin (BAB) sites (Butterfield and Massoth, 1994; Butterfield et al., 1990, 1994; Campbell et al., 1988; Connelly and others, in prep.; Douville et al., 2002; Gallant and Von Damm, 2006; James et al., in prep.; Koschinsky et al., 2008; Mottl et al., 2011; Reeves et al., 2011; Sedwick et al., 1992; Von Damm et al., 1997, 1985). E9N is the less Fe rich of the two red data points. Note that [Fe] is presented on a logarithmic scale. E: H_2S/Fe vs. Cl^- for the Kemp Caldera samples shown along with other island arc vent sites (de Ronde et al., 2011; Leybourne et al., 2012) and compared with MOR and BAB end-member fluids. Note that the island arc sites are shown as measured and not extrapolated to a zero magnesium end-member.

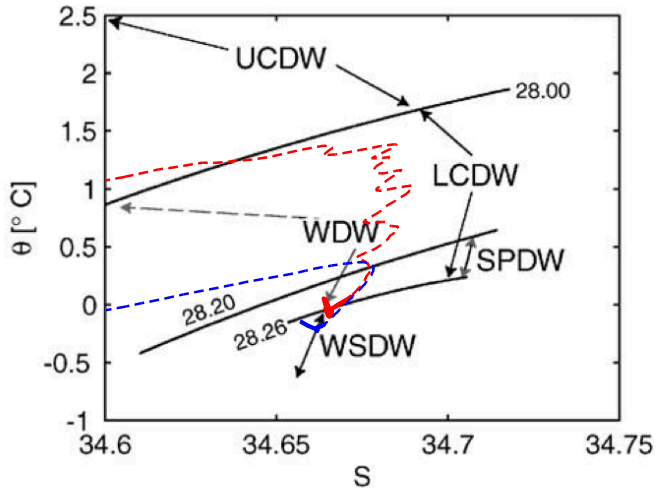

Figure 2.5: Potential temperature plotted against salinity for E2 (red) and E9N (blue). The data is overlain on the data reported in Naveira-Garabato et al. (2002) showing Weddell Sea Deep Water (WSDW) and Lower Circumpolar Deep Water (LCDW). The data are presented as dashed lines for the water column (>250 m depth) and solid lines greater than plume depth (>∼2000 m).

centrations. This was largely due to a lack of vent orifices and the friability of the vent chimneys, which were mainly composed of a mixture of anhydrite, sphalerite and elemental sulfur (Stock, 2012). It is also common to find extensive sub-surface mixing of hydrothermal fluids/gases and seawater at island arc hydrothermal sites (Butterfield et al., 2011; Leybourne et al., 2012), possibly due to the more vesicular nature of the crust in regions with high magmatic gas input (Fouquet et al., 1991). Island arc vent fluids can also be enriched in magnesium or sulfate due to high acidity and the disproportionation of magmatic sulfite (Gamo et al., 1997). Despite being highly mixed with seawater, the fluids collected were extremely concentrated in hydrogen sulfide (up to 41.7 mM, Table 2.1). Elemental sulfur was also present in many parts of the caldera floor and chimneys, likely indicating the sub-surface disproportionation of magmatic sulfite (Butterfield et al., 2011; de Ronde et al., 2011). The high concentration of sulfide may be a secondary product of hydrothermal fluid interaction with rock and seawater due to a long sub-surface reaction pathway (de Ronde et al., 2011; Leybourne et al., 2012), and the extremely variable temperatures and compositions (spatially and temporally) measured suggest that

several phases are being actively vented at this site (Connelly and others, in prep.). The high hydrogen sulfide combined with pervasive elemental sulfur certainly make the site unusual amongst other reported island arc sites, and the Kemp Caldera is definitely not a typical hydrothermal vent environment in a global context. This should be bared in mind in Chapter 5 - but it should also be considered that the water column characteristics in the Kemp Caldera are fairly typical (Table 2.1), and so the controls on the development of Fe may be more universally applicable than the vent fluid compositions (Field and Sherrell, 2000).

Table 2.1: Hydrothermal and seawater end-member composition at E2, E9N and the Kemp Caldera. Vent fluid data from Rogers et al. (2012), James et al. (in prep.) and Connelly and others (in prep.), N/A = not assessed. Data in brackets signifies that the value is not extrapolated to end-member, but is highest or lowest measured.

	E2	E9N	East Scotia Sea (>1800 m depth)	Kemp Focussed	Kemp Diffuse	Kemp Caldera (>1000 m depth)
Max temperature (°C)	353	383	~0	(212)	(28)	0.2
pH (total scale, at 25°C for vent fluids)	2.9	3.4	7.9 (in situ)	(4.3)	(5.9)	7.85
Cl^- (mM)	536	98	541	(438)	(511)	541
H_2S (mM)	6.7	9.5	0	(41.7)	(8.6)	0
DFe (M)	1.28×10^{-3}	0.80×10^{-3}	1.7×10^{-9}	(1.75×10^{-6})	(1.96×10^{-6})	$>15 \times 10^{-9}$
DMn (M)	2.05×10^{-3}	0.20×10^{-3}	0.5×10^{-9}	(164×10^{-6})	(22.8×10^{-6})	$>35 \times 10^{-9}$
H_2S:Fe	5.2	11.9	0	<100,000	< 10,000	0
Dissolved O_2 (μmol kg^{-1})	N/A	N/A	200 (E2), 172 (E9N)	N/A	N/A	348
Dissolved inorganic carbon (DIC; μmol kg^{-1})	(7815)	N/A	2256	(7184)	(3256)	2266
Total alkalinity (TA; μmol kg^{-1})	-0.920	-0.580	2360	(380)	(2660)	2339
Total P (μmol kg^{-1})	N/A	N/A	2.15 (E2), 2.21 (E9N)	N/A	N/A	2.47
Total Si (mmol kg^{-1})	17.7	8	0.12	(3.13)	(1.06)	N/A

Chapter 3

Reverse Titration - Competitive Ligand Exchange - Adsorptive Cathodic Stripping Voltammetry (RT-CLE-ACSV)

Contents

Abstract

Here we demonstrate the use of reverse titration - competitive ligand exchange - adsorptive cathodic stripping voltammetry (RT-CLE-ACSV) for the analysis of iron (Fe) binding ligands in seawater. In contrast to the forward titration, which examines excess ligands in solution, RT-CLE-ACSV examines the existing Fe-ligand complexes by increasing the concentration of added (electroactive) ligand (1-nitroso-2-naphthol) and analysis of the proportion of Fe bound to the added ligand. The data manipulation allows the accurate characterisation of ligands at equal or lower concentrations than Fe in seawater, and disregards electrochemically inert dissolved Fe such as some colloidal phases. The method is thus superior to the forward titration in environments with high Fe and low ligand concentrations or high concentrations of inert Fe.

We validated the technique using the siderophore ligand ferrioxamine B, and observed a stability constant $K'_{Fe^{3+}FoB}$ of 0.74 - 4.37 x 10^{21} mol^{-1}, in agreement with previous results. We also successfully analysed samples from coastal waters and a deep ocean hydrothermal plume. Samples from these environments could not be analysed with confidence using the forward titration, highlighting the effectiveness of the RT-CLE-ACSV technique in waters with high concentrations of inert Fe.

3.1 Introduction

Iron is a biologically important element that limits primary productivity in large parts of the world's oceans due to its low concentrations (typically <0.1 - 1 nM) (Boyd et al., 2007; Martin and Fitzwater, 1988). Iron is particle reactive and has a short residence time ranging from weeks to months in the surface, to hundreds of years in the deep ocean (Bergquist and Boyle, 2006). The element has a low solubility of 0.01 nM (at 25°C) or 0.19 nM (at 5°C) in NaCl solutions (Liu and Millero, 2002), however dissolved Fe is present in seawater at concentrations averaging 0.79 nM at depth greater than 500 m (Johnson et al., 1997). The increased solubility has been attributed to complexation by organic ligands (Liu and Millero, 2002), but the presence of colloidal phases (1-200 nm size) may also contribute to the stabilisation of Fe concentrations in seawater (Bergquist et al., 2007; Cullen et al., 2006; Nishioka et al., 2001; Ussher et al., 2010; Wu et al., 2001). Organic ligands and colloids hence prevent the formation of insoluble Fe oxy-hydroxides and studies have reported that >99% of dissolved Fe is complexed by strong ligands at pH 8 (Rue and Bruland, 1997; Van Den Berg, 1995) with conditional Fe-binding stability constants ($K'_{Fe^{3+}L}$) ranging from 10^{19}-10^{23} mol^{-1} (Gledhill and Buck, 2012).

The most commonly used technique for determination of iron binding ligands in seawater is competitive ligand exchange - adsorptive cathodic stripping voltammetry (CLE-ACSV). In this electrochemical procedure, an electroactive ligand (AL) with a known Fe-AL complex stability constant ($K'_{Fe^{3+}AL}$) is added to the sample, followed by addition of increasing concentrations of Fe. Following an equilibration period (typically overnight), the increase in FeAL is determined and competition for Fe by natural ligands in the sample is inferred by the difference between $[Fe]_{total}$ and [FeAL] (Croot and Johansson, 2000; Gledhill and van den Berg, 1994; Rue and Bruland, 1995; Wu and Luther, 1995).

The CLE-ACSV technique has been successful in studies of ocean waters, which generally have very low concentrations of Fe (<1 nM) and an excess of organic ligands over Fe (see Gledhill and Buck, 2012, for a comprehensive compilation of

results). However, CLE-ACSV does not allow for an accurate analysis of samples when ligands occur at concentrations lower than Fe (Laglera et al., 2013; Witter et al., 2000). This becomes problematic in regions with large Fe inputs or high concentrations of inert Fe that is not bound to organic ligands (Buck et al., 2007; Croot and Johansson, 2000; Gerringa et al., 2007; Wu and Luther, 1995). Such regions include coastal waters, surface waters adjacent to ice sheets, hydrothermal plumes, and ocean waters exposed to dust deposition or sediment re-suspension (Gledhill and Buck, 2012).

In this study, we outline the 'reverse titration' for marine Fe(III) – a method that has previously been described only for copper (Cu) and riverine Fe(II) (Nuester and van den Berg, 2005; Statham et al., 2012). The technique characterises ligands already bound to naturally present Fe in the sample by incrementally increasing the concentration of the electroactive competing ligand and gradually removing the Fe from the natural ligands. The concentration of added ligand required is related to the binding strength of the added ($\beta_{\mathrm{Fe^{3+}[AL]_n}}$) and natural ($\mathrm{K'_{Fe^{3+}L}}$) ligands according to the equations:

$$\mathrm{nAL' + FeL} \underset{K'_{\mathrm{Fe^{3+}L}}}{\overset{\beta_{\mathrm{Fe^{3+}[AL]_n}}}{\rightleftharpoons}} \mathrm{FeAL_n + L'} \tag{3.1}$$

$$\beta_{\mathrm{Fe^{3+}[AL]_n}} = \frac{[\mathrm{FeAL_n}]}{[\mathrm{Fe^{3+}}][\mathrm{AL'}]^n} \tag{3.2}$$

$$K'_{\mathrm{Fe^{3+}L}} = \frac{[\mathrm{FeL}]}{[\mathrm{Fe^{3+}}][\mathrm{L'}]} \tag{3.3}$$

Here we show that reverse titrations using the added ligand 1-nitroso-2-napthol (NN) can be used to determine natural ligands that are present in concentrations both equal to and lower than Fe. The concentration of Fe that is reactive to NN was also quantified during the titrations, allowing comparison with total dissolved Fe (which is an arbitrary physical definition). In order to validate the RT-CLE-ACSV technique, we used North Atlantic seawater with and without an added strong Fe binding ligand (desferrioxamine B (dFOB)). We also demonstrate the application of a curve fitting procedure using the open source software "R" to determine the Fe binding constant and concentration of natural ligands.

In order to demonstrate the key advantages of the method over the forward titration, we analysed near shore seawater from Southampton and hydrothermal plume water from the East Scotia Ridge. Samples from these environments were chosen because they are typically problematic to analyse using the forward titration method due to their high Fe concentrations.

3.2 Materials and methods

3.2.1 Reagents

All deionised water used was purified by reverse osmosis and ion exchange (18 $M\Omega cm^{-1}$, MilliQ, Millipore). Ultra pure hydrochloric acid (UpA, Romil, UK) (1% diluted in deionised water) was used for cleaning the cell between titrations. Borate buffer was prepared by dissolution of boric acid (Fisher Scientific, UK) in 0.3 M ammonia (Romil, UK) to make a 1 M solution. The pH buffer was adjusted using ultra pure HCl and ammonia (Romil, UK) to obtain a pH of 8.05 (NBS scale) at a final borate concentration of 50 mM in seawater. Iron contamination in the buffer was removed by overnight equilibration with 10 μM 2-(2-Thiazolylazo)-p-cresol (TAC) to bind Fe, and passing of the solution through two solid phase extraction columns (SepPak C18, Waters, USA) to remove $Fe(TAC)_2$. Stock solutions of the siderophore desferrioxamine B (dFOB; Sigma Aldrich, UK) were prepared by dissolution in deionised water. 1-nitroso-2-naphthol (Sigma Aldrich, UK) stock solutions for titration (0.2, 1 and 4 mM) were prepared by dissolution in methanol (HPLC grade, Fisher Scientific, UK). Iron standards were prepared from hydrated Fe chloride (Fisher Scientific, UK) into 0.1% acid (UpA HCl in deionised water). The Fe standard concentrations were confirmed by Inductively Coupled Plasma - Mass Spectrometry (Thermo Scientific X-Series).

3.2.2 Equipment

Voltammetric measurements were conducted using a μAutolab potentiostat (Ecochemie, NL) with a hanging mercury drop working electrode (HMDE, surface area 0.38 mm^2; VA663 Stand (Metrohm, NL)), a double junction Ag/AgCl reference

electrode filled with 3 M KCl, and a glassy carbon counter electrode. All bottles used were Low/High Density Polyethylene (LDPE/HDPE), cleaned by soaking in 2% Decon 90 (Decon, UK) (2 days), 50% HCl (analytical grade, Fisher UK, 1 week) and 50% HNO_3 (analytical grade, Fisher UK, 1 week) followed by rinsing with deionised water (MilliQ). Where indicated, seawater was UV treated with a 400 W mercury lamp (Photochemical Reactors Ltd, UK) for 4 h (either at ambient pH or pH 2) prior to analysis to destroy Fe binding organic ligands (Achterberg et al., 2001).

3.2.3 Sample collection

A batch of low metal seawater was collected from the surface (3 m depth) of the North Atlantic Ocean, filtered (0.2 μm, Sartorius Sartobran P300) at sea and stored at 4℃ in Southampton. Aliquots of this water were re-filtered (0.2 μm, Sartorius Sartobran P300) no more than 1 day before analysis and were used for preparation of ligand free seawater by UV digestion (herein termed UVSW) and dFOB spiked UVSW.

Surface water samples were taken from a pontoon in Southampton (referred to as 'near shore', salinity = 30.6) using an acid cleaned LDPE bottle. The samples were filtered (0.2 μm, Sartorius Sartobran P300) and prepared for titration immediately.

A sample from a plume of the E2 hydrothermal vent field in the East Scotia Sea was collected using an externally sprung Ocean Test Equipment (OTE) bottle mounted on a titanium frame with a Seabird +911 Conductivity, temperature and depth (CTD) profiler system. Two aliquots were taken from the OTE bottle into acid cleaned LDPE bottles by filtration (0.2 μm polycarbonate membrane filter, Whatman). One was acidified (pH 2, UpA HCl) and stored at room temperature; this was treated by UV radiation before analysis. The other was stored at -20℃ and left untreated. The frozen aliquot was defrosted overnight at 4℃ (close to the in-situ temperature) and shaken vigorously before preparation of the titration. A third aliquot was acidified in a LDPE bottle for analysis of dissolved Fe (DFe). DFe

was measured using Inductively Coupled Plasma - Mass Spectrometry (ICP-MS; Thermo Scientific X-Series) after pre-concentration by mixed ligand extraction into chloroform and dissolution into nitric acid. (Bruland et al., 1979)

3.2.4 Procedure for RT-CLE-ACSV

1 ml of borate buffer (1 M) was added to each 200 ml seawater sample (final concentration 50 mM) to stabilise the pH at 8.05 (NBS scale, 7.90 on total scale). 15 ml aliquots of the seawater were pipetted into 12 polytetrafluoroethylene (PTFE) vials, and the stock solutions (0.2, 1, 4 mM) of NN were added to the vials to achieve final concentrations in the range of 0.25 – 40 μM. For UVSW/dFOB spiked samples, Fe was added to each vial to achieve a concentration of 20 nM. No Fe was added to the natural samples. The solutions were left to equilibrate overnight as in the forward titration CLE-CSV method (Croot and Johansson, 2000). One vial was left with a very low [NN] (< 0.5 μM) to quantify the blank signal (typically about 1 nA) for each titration. In order to allow the vials to equilibrate with the solutions, they were pre-conditioned twice as above and then rinsed with deionised water.

In order to remove dissolved oxygen in the sample, each sample was purged with nitrogen gas (zero grade, BOC UK) for 5 min prior to deposition. The solution was stirred with a PTFE rod during the purging and deposition steps. A deposition potential of -0.05 V was applied for 120 - 600 s (depending on [Fe_{NNmax}]) and then the voltage scanned from -0.15 to -0.65 V at 15 Hz, 50 mV s^{-1} using sampled DC. The $Fe(NN)_3$ peak occurred at a potential of -0.42 to -0.50 V. Peak fitting software (Peakfit, Seasolve) was used to separate the $Fe(NN)_3$ peak from the unknown peak which occurs at $\sim$ -0.53 V (Boye et al., 2001). Samples were measured in order of increasing NN concentration, and the cell was not rinsed between vials to keep the cell conditioned to NN and Fe.

The concentration of $Fe(NN)_3$ at the highest NN concentration was quantified by standard addition of Fe. This concentration is herein defined as [Fe_{NN}], a measure of 'labile' Fe. [Fe_{NN}] does not necessarily include all dissolved Fe (Figure 3.1).

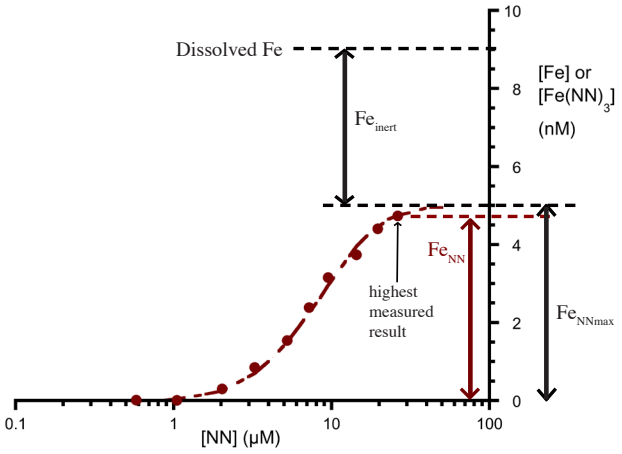

Figure 3.1: Typical reverse titration data (red circles) over a range of concentrations of NN. The highest measured current response corresponds to Fe_{NN} and the modelled response at i_{pmax} corresponds to all Fe in equilibrium with the ligands (Fe_{NNmax}). The rest of the dissolved Fe (DFe) is classed as inert (Fe_{inert}). In this example DFe = 9 nM and Fe_{NNmax} = 5 nM.

3.2.5 Calculation of $\beta_{Fe^{3+}[NN]_3}$ and $K'_{Fe^{3+}L}$ with UV treated seawater

Low metal seawater was treated by UV radiation (UVSW) at ambient pH. The sample was buffered and measured into 15 ml aliquots as above. 20 nM Fe was added to each vial, then NN was added and the samples were left overnight and analysed as above. This was repeated with 10 nM, 15 nM and 20 nM desferrioxamine B (dFOB) for characterisation of this siderophore ligand and validation of the method. Values for $\beta_{Fe^{3+}[NN]_3}$ and $K'_{Fe^{3+}L}$ were calculated using the experimental data and the mass balance of Fe, as described below.

3.2.6 Foward titration

A CLE-ACSV Fe titration was conducted on the near shore seawater sample for comparison with RT technique. Eleven conditioned PTFE vials were pipetted with 15 ml buffered sample followed by NN (for a final concentration of 6 μM). Iron was added to achieve the following concentrations (in addition to ambient Fe): 0, 0, 1, 2, 3, 4, 6, 8, 10, 12, and 19 nM. The vials were left to equilibrate overnight and were analysed using the same voltammetric settings as for the reverse titration.

3.3 Theory

In a reverse titration the electroactive competing ligand added to the sample is increased and the amount of metal bound to natural inorganic and organic ligands is progressively decreased. The increased peak height of the metal-electroactive ligand complex is measured by ACSV. In the case of Fe, at high added ligand concentrations, the peak height levels off towards a maximum current (i_{pmax}) where all Fe reactive to the added ligand (AL) occurs as $Fe(AL)_n$. All other measurements are normalised to this value ($X = i_p/i_{pmax}$), eliminating the effect of salinity, pH or total Fe concentration on sensitivity (Nuester and van den Berg, 2005). If i_{pmax} is not reached during the titration (the current does not level off), then i_{pmax} and the total Fe concentration in equilibrium with ligands (Fe_{NNmax}) can be modelled by non-linear regression (see below). FeAL is measured at a high AL concentration, and in cases where i_{pmax} is not reached, Fe_{NNmax} is estimated by non-linear regression modelling (Figure 3.1). The normalised current response, X, equals the concentration of Fe bound to AL ($[Fe(AL)_n]$) divided by all Fe species in equilibrium:

$$X = \frac{i_p}{i_{pmax}} = \frac{[Fe(AL)_n]}{[Fe_{NNmax}]} = \frac{[Fe(AL)_n]}{[Fe(AL)_n]+[Fe'] + \sum [FeL_i]} \tag{3.4}$$

The $Fe(AL)_n$ concentration is the product of the concentration of unbound Fe ($[Fe^{3+}]$) and the α coefficient of the FeAL species, and the AL occurs in large excess over Fe, so the majority of the AL is in unbound form, and $\alpha_{Fe(AL)_n}$ can be approximated to the product of the AL concentration and the stability constant (Equation 3.5):

$$Fe(AL)_n = \alpha_{Fe(AL)_n}[Fe^{3+}] = \beta_{Fe(AL)_n}[AL]^n[Fe^{3+}] \tag{3.5}$$

Natural ligands are not in large excess and are generally present at concentrations similar to Fe, so the mass balance of L_i needs to be considered (L' is unbound ligand):

$$L_i = L' + FeL \tag{3.6}$$

Where the ligand–Fe complex (FeL) has a conditional stability constant $K'_{Fe^{3+}L}$ (3.3). Substitution of Equation 3.6 into Equation 3.3 leads to Equation 3.7 (the Langmuir isotherm) by rearrangement:

$$[FeL] = \frac{[L_i]K'_{Fe^{3+}L}[Fe^{3+}]}{1 + K'_{Fe^{3+}L}[Fe^{3+}]} \tag{3.7}$$

Substituting Equation 3.7, 3.5 and the inorganic side reaction coefficient of Fe ($\alpha_{Fe'} = [Fe']/[Fe^{3+}]$) into Equation 3.4 and cancelling $[Fe^{3+}]$, Equation 3.8 is obtained (where L_i are various naturally occurring ligands):

$$X_1 = \frac{\alpha_{Fe(AL)_n}}{\alpha_{Fe(AL)_n} + \alpha_{Fe'} + \sum_i \frac{[L_i]K'_{Fe^{3+}L_i}}{1+K'_{Fe^{3+}L_i}[Fe^{3+}]}} \tag{3.8}$$

In UV treated seawater with no organic ligands, Equation 3.8 is simplified to Equation 3.9:

$$X_2 = \frac{\alpha_{Fe(AL)_n}}{\alpha_{Fe(AL)_n} + \alpha_{Fe'}} \tag{3.9}$$

$\alpha_{Fe(AL)_n}$ is varied (from $\sim$ 6.5x10^7 to $\sim$ 3.5x10^{13}) in the titration as calculated by Equation 3.5 using the obtained value of $\beta_{Fe(AL)_n}$ from UVSW analyses. $\alpha_{Fe'}$ constitutes the ratio of inorganic Fe (Fe′) to free Fe (Fe^{3+}) ($10^{9.80}$; see Appendix A). Fe^{3+} can be expressed as a polynomial function (Nuester and van den Berg, 2005) in terms of the α coefficients Equation (3.10) so that only $K'_{Fe^{3+}L}$ and [L] are unknown. These parameters are adjusted to fit Equation (3.8) to the experimental values of X.

$$\begin{aligned} &K'_{Fe^{3+}L}(\alpha_{Fe(AL)_n} + \alpha_{Fe'})[Fe^{3+}]^2 \\ &+(\alpha_{Fe(AL)_n} + \alpha_{Fe'} + \alpha_{FeL} - K'_{Fe^{3+}L}[Fe_{NNmax}])[Fe^{3+}] \\ &-[Fe_{NNmax}] \\ &= 0 \end{aligned} \tag{3.10}$$

3.3.1 Fe mass balance when Fe is in excess of ligands

If a natural ligand binds Fe in a 1:1 molecular ratio and is in deficit of the Fe_{NNmax}, then only a portion of the Fe can be bound by the ligand. The rest of the Fe_{NNmax} is bound to inorganic ligands or the AL. This is a crucial feature of this method that leads to the current response curve being the sum of two curves (see Figure 3.4 for an example). In this case, Equation 3.8 is split into two parts, including L in only one part:

$$X_3 = (1-j)\frac{\alpha_{Fe(AL)_n}}{\alpha_{Fe(AL)_n} + \alpha_{Fe'}} + j\frac{\alpha_{Fe(AL)_n}}{\alpha_{Fe(AL)_n} + \alpha_{Fe'} + \sum \frac{[L_i]K'_{Fe^{3+}L}}{1+K'_{Fe^{3+}L}[Fe^{3+}]}} \tag{3.11}$$

Where j is the fraction (0-1) of iron equal to the concentration of L. A second, weaker ligand can be added to both parts of the equation, leading to a cubic function for calculation of $[Fe^{3+}]$. Two ligands are not always observed by traditional CLE methods (Buck and Bruland, 2007; Buck et al., 2007; Hunter and Boyd, 2007), which may be due to the limits of the detection window and the biased competition between the strong and weak ligands for added Fe in the forward titration method, but may also be due to environmental differences between the distributions of strong and weak ligands (Kondo et al., 2012). In the examples used in this study, little evidence was found for the presence of a second ligand within the applied detection window.

3.3.2 Data fitting

A code package for the statistical analysis software R has been written to simultaneously solve the Langmuir isotherm (Equation 3.7), Equation 3.8 (for one saturating ligand) and Equation 3.11 (both for one unsaturated ligand and for two ligands where one is in deficit of Fe). The non-linear regression models progressively increase the starting value of $K'_{Fe^{3+}L_1}$ and compute values for $[L_1]$, $[L_2]$, $K'_{Fe^{3+}L_2}$ and i_{pmax}. When the residuals of the non-linear regression cease to improve, the iteration ends and the results are reported. More information is presented in Appendix B.

In the simplest form of the model, [Fe_{NN}] is measured after the current has levelled off and the ligand is in equal concentration with [Fe_{NN}] (and [Fe_{NNmax}]). In this case, L and i_{pmax} are known and only $K'_{Fe^{3+}L}$ has to be fitted to the data. If the current response has not reached i_{pmax} by the end of the titration, R can model the true i_{pmax} by scaling the data by a factor f until a good fit can be achieved. [Fe_{NNmax}] is then calculated as [Fe_{NN}]/f. If L is also in deficit of [Fe_{NNmax}], [L] is added as a third parameter with an upper limit of [Fe_{NNmax}]. A second ligand L_2 would add two more unknown parameters, $K'_{Fe^{3+}L_2}$ and [L_2]. The more parameters that have to be fitted, the larger the errors will be in the non-linear regression model. For the forward titration data manipulation we used a van den Berg/Ružić linearization of the data (Ruzic, 1982; Van Den Berg, 1982).

3.4 Results and discussion

3.4.1 Modelled change in X in response to increased [AL]

We used Equation (3.8), (3.9) and (3.11) to model normalised current response (X) in seawater with variations in $K'_{Fe^{3+}L}$, [Fe]:[L] and salinity.

3.4.1.1 Comparison with Cu RT-CLE-ACSV

The RT-CLE-ACSV response for UV treated seawater (Equation (3.9)) shows a Michaelis-Menten type curve with a sharp increase in X starting at [NN] = 1 μM (3.2). $\alpha_{Fe(NN)_3}$ is higher ($\sim$ 5 x 10^8) at this point than at the corrsponding point in the reverse Cu titration (Nuester and van den Berg, 2005), $\alpha_{Cu(SA)_2}$ = 0.915, due to the comparatively higher inorganic side reaction coefficient of Fe ($\alpha_{Fe'}$ =$10^{9.80}$, $\alpha_{Cu'}$ = 35). The high $\alpha_{Fe'}$ sets the lower limit of the detection window for the method, as ligands with α_{FeL} within an order of magnitude of $\alpha_{Fe'}$ will not be easily distinguished from the inorganic species (Figure 3.3A). The titration curve is sharper for [$FeNN_3$] than [$CuSA_2$] due to the presence of non-electroactive CuSA in solution, which flattens the Cu titration curve, particularly at low concentrations of SA where CuSA represents a greater proportion of Cu species. This is also the reason that a maximum of 96% of i_{pmax} is measured for Cu within the range of

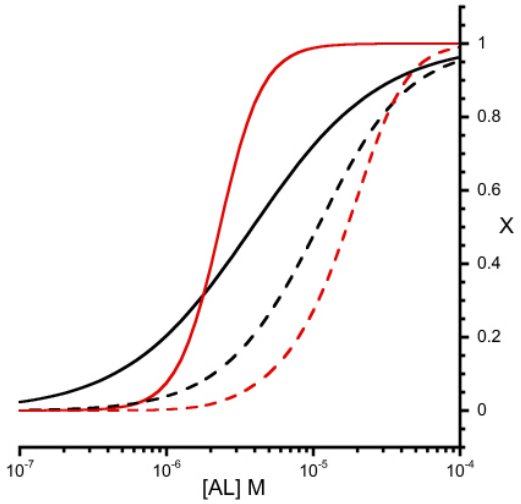

Figure 3.2: Comparison of the modelled response of Cu with salicylaldoxime (black; Nuester and van den Berg, 2005) and iron with 1-nitroso-2-naphthol (red; this study). Solid lines represent the curve for UV treated seawater (no ligand) and dashed lines seawater with a typical ligand saturating the metal ($\log(K'_{CuL}) = 13.3$ and $\log(K'_{FeL}) = 21.0$).

concentrations used (Nuester and van den Berg, 2005). Other FeNN species ($FeNN_2$ or FeNN) do not compete with $FeNN_3$ in solution, allowing i_{pmax} to be reached.

3.4.1.2 Sensitivity to $K'_{Fe^{3+}L}$, salinity and $[Fe_{NN_{MAX}}]$ when $[Fe_{NN_{MAX}}]=[L]$

We modelled the response in X over a range of concentrations of NN based on Equation 3.8. Changes to $K'_{Fe^{3+}L}$ by an order of magnitude have a large effect on X (Figure 3.3A), as higher concentrations of the AL are required to outcompete L (Equation 3.8). The model indicates that if [Fe] and [L] = 5 nM, all natural ligands with $\log(K'_{Fe^{3+}L}) = 19$ - 21 will be outcompeted when NN = 100 μM. As explained later, we conducted our titrations up to 40 μM NN giving a detection window of $\alpha_{Fe^{3+}L} = 9.5$ - 13.0 for Fe, L = 5 nM. Salinity has a small effect on X over the typical oceanic range (32-36) due to small changes to $\beta_{Fe^{3+}[NN]_3}$ (Gledhill and van den Berg, 1994) and $\alpha_{Fe'}$ (Figure 3.3B). At lower salinities (<20) $\beta_{Fe^{3+}[NN]_3}$ and $\alpha_{Fe'}$ both increase more substantially (by 4 and 2 times, respectively, at S = 10), and this leads to a higher upper limit of detection of $K'_{Fe^{3+}L}$. Conversely, as

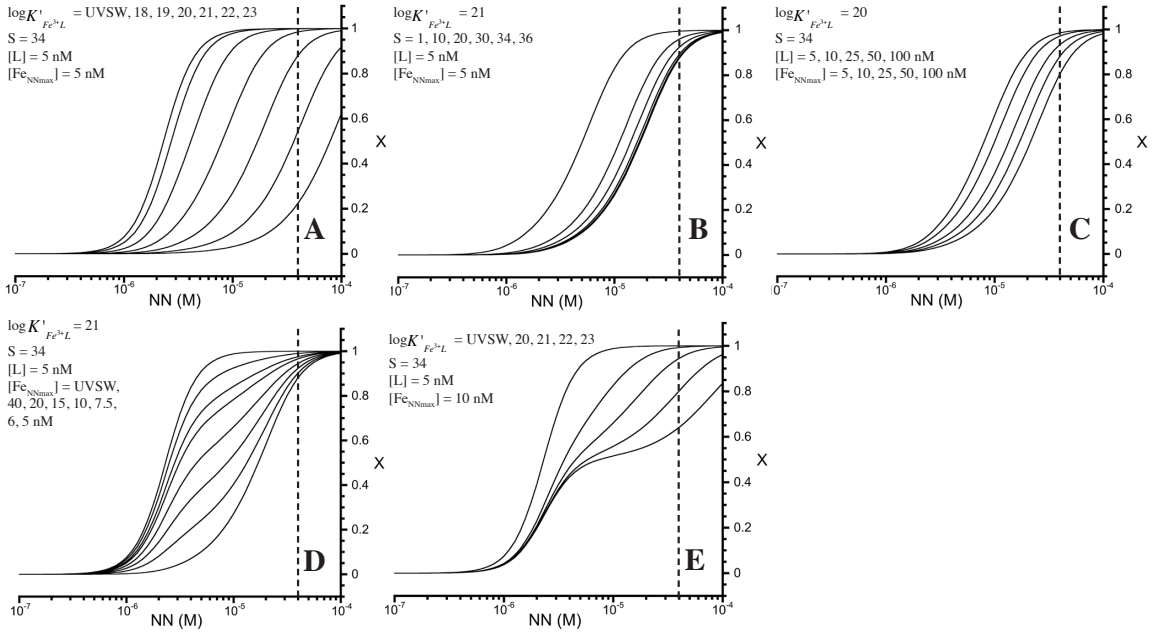

Figure 3.3: Modelled effect of various parameters on the normalised current response, X. The vertical dotted line represents the highest concentration of NN used in this study (40 μM). A: Change as a function of $K'_{Fe^{3+}L}$. B: As a function of salinity. C: As a function of $[Fe_{NNmax}]$ when $[Fe_{NNmax}] = [L]$. D: As a function of $[Fe_{NNmax}]$ when $[Fe_{NNmax}] > [L]$. E: As a function of $K'_{Fe^{3+}L}$ when $[Fe_{NNmax}] = 2$ x [L].

$[Fe_{NNmax}]$ and [L] increase (typical in lower salinity waters) the detection window of $K'_{Fe^{3+}L}$ is lowered by a comparable order (Figure 3.3C). The combined effect of these changes is likely to keep the detection window similar for $K'_{Fe^{3+}L}$ in most marine samples.

3.4.1.3 Effect of $[Fe_{NNmax}]$ and $K'_{Fe^{3+}L}$ when $[Fe_{NNmax}]>[L]$

Using Equation 3.11, we modelled the response in X over a range of $[Fe_{NNmax}]$:[L] ratios (Figure 3.3D) and modified $K'_{Fe^{3+}L}$ when the ligand was in deficit of Fe_{NNmax} (Figure 3.3E). The curve shape was sensitive to change in both parameters, suggesting that the model should be able to determine ligands at lower concentrations than Fe_{NNmax}. In principle, two distinct ligands can be determined by this technique, but it is unlikely that two ligands will be discernable from each other and the inorganic species within the detection window for NN.

3.4.1.4 RT-CLE-ACSV when $[L]>[Fe_{NNmax}]$

RT-CLE-ACSV cannot be used to determine ligands which are in excess of NN labile Fe. Only existing FeL complexes are outcompeted in the titration and unbound ligands are not included in the equilibrium calculations. If excess L is present, the concentration of $[Fe^{3+}]$ is lower, but the effect on X is not noticeable over typical oceanic concentrations of L and Fe. For this reason the RT-CLE-ACSV method is not a suitable replacement for the forward titration for analysis of systems where L is in excess of Fe. In the calculation of $K'_{Fe^{3+}L}$, the value of L used is set to be less than or equal to $[Fe_{NNmax}]$, and excess L has an insignificant effect on the calculated $K'_{Fe^{3+}L}$. Therefore RT-CLE-ACSV is limited to assessing FeL and not excess L, whereas the forward titration is limited to assessing excess L and can only infer information about FeL.

3.4.2 Detection limit and linearity

The limit of detection (3σ of response) for a deposition time of 5 min was 0.55 nM Fe at 2 μM NN and 0.38 nM Fe at 20 μM NN. Data analysis becomes less accurate at the limit of detection, and this method is best suited for samples with

$[Fe_{NNmax}]$ >2 nM (using a 5 min deposition time). The detection limit may be improved by adding a catalyst such as bromate (Aldrich and van den Berg, 1998), however the use of a catalyst can potentially affect the Fe speciation (Rue and Bruland, 1995), particularly due to oxidation of Fe complexes. For a 5 min deposition time, the current response was linear for concentrations of Fe up to 30 nM. Current response was also linear over the range of NN concentrations used in this study when deposition times were increased up to 20 min, indicating that for the conditions used in these experiments, NN did not compete for adsorption sites on the surface of the Hg drop. Unlike Nuester and van den Berg (2005), we performed the reverse titration after overnight equilibration of the aliquots. These workers found that equilibration was achieved after 30 min for Cu binding ligands and added salicylaldoxime, but initial tests for Fe suggested equilibration times closer to 3 h, making titration in a single cell impractical. It is likely that slow FeL dissociation rates ($k_d = 10^{-5} - 10^{-7}$ s^{-1}) control the equilibration time, and some complexes may be so strong that they do not dissociate at all in these experimental timescales (Luther III and Wu, 1997; Witter et al., 2000; Witter and Luther, 1998; Wu and Luther, 1995). Overnight equilibration is used in most Fe ligand forward titrations (Boye et al., 2001; Croot and Johansson, 2000; Gerringa et al., 2007; Gledhill and van den Berg, 1994), and following this routine allows the best comparison with previous results. The upper limit of $[Fe_{NNmax}]$ is set by the necessity for the added ligand to be in large excess, and we suggest that samples with $[Fe_{NNmax}]$ >50 nM are diluted, as reported previously (Buck et al., 2007; Nagai et al., 2004).

Regarding the range of NN concentrations used, we encountered problems with high background currents obscuring the $Fe(NN)_3$ peak at [NN] >40 μM (the vertical dotted lines in Figure 3.3), leading to a smaller than theoretical detection window. Care should be taken if i_{pmax} is not reached within the applied concentration range of AL, as modelling the value of i_{pmax} in addition to $K'_{Fe^{3+}L}$ and [L] leads to greater uncertainty in the results.

3.4.3 Calibration of $\beta_{Fe^{3+}[NN]_3}$ with UVSW

Low metal seawater was irradiated with UV light to remove all organic ligands and the sample was subsequently analysed (with added 20 nM Fe) by RT-CLE-ACSV. The UVSW titration data were used to calculate $\beta_{Fe^{3+}[NN]_3}$ as follows.

An $\alpha_{Fe'}$ of $10^{9.80}$ was obtained at 22.5℃ (analysis temperature), pH 7.90 (as measured on the total scale) and ionic strength = 0.71 M, using experimentally determined inorganic stability constants (Byrne and Kester, 1976; Byrne et al., 2005; Millero and Pierrot, 2007) (see Appendix A). Assuming that all ligands are destroyed during UV treatment, $\alpha_{Fe'} = \beta_{Fe^{3+}[NN]_3}[NN]^3$ at X = 0.5 in UVSW (Equation 3.9). In our experimental data, X = 0.5 when [NN] = 2.31 x 10^{-6} M, so $\beta_{Fe^{3+}[NN]_3}$ = 5.12 x 10^{26} mol^{-3}. Previously, $\beta_{Fe^{3+}[NN]_3}$ has been reported as 6.31 x 10^{27} mol^{-3} (Wu and Luther, 1995), 2.51 x 10^{28} mol^{-3} (Van Den Berg, 1995) and 5.37 x 10^{28} mol^{-3} (Laglera et al., 2011). The value determined for $\beta_{Fe^{3+}[NN]_3}$ in this study is thus lower than previously reported values. Our value is calculated from a comparison with the inorganic side reaction coefficient alone, while previous results have used added ethylenediaminetetraacetic acid (EDTA) in a type of reverse titration with NN. The pH used here (7.90) has a large effect on the result as this affects $\alpha_{Fe'}$ substantially. However, the difference between our calculated value for $\beta_{Fe^{3+}[NN]_3}$ and those found previously are likely to be within the limits of error for both approaches. $\beta_{Fe^{3+}[NN]_3}$ here (and $K'_{Fe^{3+}L}$ later) are calculated as a function of $\alpha_{Fe'}$, so all results can be scaled according to the calcuated thermodyanmics of the inorganic side reaction. We proceed with $\beta_{Fe^{3+}[NN]_3}$ = 5.12 x 10^{26} mol^{-3}.

3.4.4 Reverse titration of UVSW with added desferrioxamine B

The siderophore ligand desferrioxamine B (dFOB) was added to UVSW to determine the decrease in current response in the presence of a strong ligand. We prepared three titrations with dFOB in equal and lower concentrations than Fe, and using the non-linear regression model in R to calculate $K'_{Fe^{3+}FoB}$, [dFOB] and i_{pmax}, we determined a conditional stability constant ($K'_{Fe^{3+}FoB}$) of 0.74 - 4.37 x 10^{21}

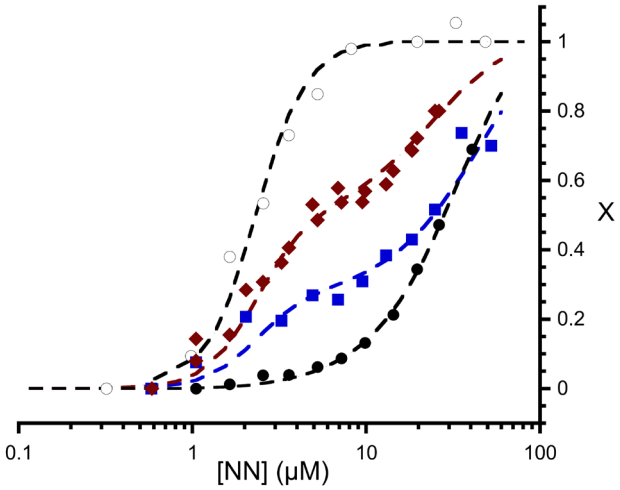

Figure 3.4: Demonstration of the reverse titration using 1-nitroso-2-naphthol (NN) as the added ligand and ferrioxamine B (dFOB) as a competing ligand. Empty circles: UV treated seawater; red diamonds: 10 nM dFOB, 20 nM Fe (two titrations shown); blue squares: 15 nM dFOB, 20 nM Fe; black circles: 20 nM dFOB, 20 nM Fe. i_{pmax} is not reached for the dFOB spiked samples, and is calculated using the measured [Fe] at the highest NN concentration and the non-linear regression model in R. Dashed lines are the model output.

mol^{-1} for the three titrations (Figure 3.4, Table 3.1). These are slightly lower than (but compare reasonably well with) literature values of 3.94 and 3.98 x 10^{21} mol^{-1} (van den Berg, 2006; Witter et al., 2000) and indicate that the procedure allows the determination of ligand characteristics at concentrations lower than Fe.

In the titrations with FoB, 69-80% of i_{pmax} was reached (Table 3.1) at the highest experimental concentration of NN ($20 - 40$ μM). At higher [NN] the background current obscured the $Fe(NN)_3$ peak, and therefore NN is not recommended for the determination of ligands stronger than dFOB. The detection window and sensitivity of other ligands could be modelled for future work (Laglera et al., 2013).

3.4.5 Analysis of seawater samples

3.4.5.1 Near shore samples

We analysed two seawater samples which would be problematic to study using the forward titration due to high concentrations of Fe. The first sample was taken from a near shore area in Southampton and was analysed by forward and reverse titra-

Table 3.1: Calculated $K'_{Fe^{3+}FoB}$ and [FoB] values using the non-linear regression model in R. The error in calculation increases when i_{pmax} is not reached

Sample	$K'_{Fe^{3+}FoB}/mol^{-1}$		[FoB]/nM		i_{pmax}
	Calculated	Expected	Calculated	Expected	scaling
FoB = 20 nM, Fe = 20 nM	0.74 ±0.08 x 10^{21}	3.96 x 10^{21}	Saturated	–	0.69
FoB = 15 nM, Fe = 20 nM	4.37 ±1.56 x 10^{21}	3.96 x 10^{21}	14.7 ±0.65	15.0	0.70
FoB = 10 nM, Fe = 20 nM	1.32 ±0.32 x 10^{21}	3.96 x 10^{21}	11.1 ±0.37	10.0	0.80

tions. Mathematical manipulation of forward titration data requires knowledge of the initial concentration of Fe in the sample, and this is often determined following sample storage at pH 2 followed by flow injection analysis (e.g. Boye et al., 2001), graphite furnace atomic adsorption spectroscopy (e.g. Gerringa et al., 2007), microwave digestion and CLE-ACSV (e.g. Buck et al., 2007) or UV digestion and CLE-ACSV (e.g. Van Den Berg, 1995). These techniques determine total dissolved Fe (DFe) and thus may include inert Fe that is not in equilibrium with AL. The use of DFe in the data treatment therefore leads to overestimation of [L] and $K'_{Fe^{3+}L}$ (Gledhill and Buck, 2012; Laglera et al., 2011).

Here we suggest that determination of an operationally defined Fe concentration that is in equilibrium with ligands under the conditions of our experiment (Fe_{NNmax}) will provide a better estimate of the initial Fe concentration in the sample and thus yield a better estimation of the ligand concentration and conditional stability constant. We used a concentration of 40 μM NN to determine Fe_{NN}, at which point the current response had levelled off in the reverse titration (Figure 3.5C). The side reaction coefficient for NN ($\alpha_{Fe^{3+}(NN)_3}$) at 40 μM is 3.3 x 10^{13}, almost two orders of magnitude higher than that commonly used for the forward titration (8.5 x 10^{11}; Buck et al., 2012). The detection window for the forward titration at this concentration of Fe is between $\log(\alpha_{Fe^{3+}L})$ = 10.9 - 12.9, compared with 10.8 - 12.8 for the NN reverse titration. Using $[Fe_{NN}]$ = 9.23 nM (as measured at [NN] =

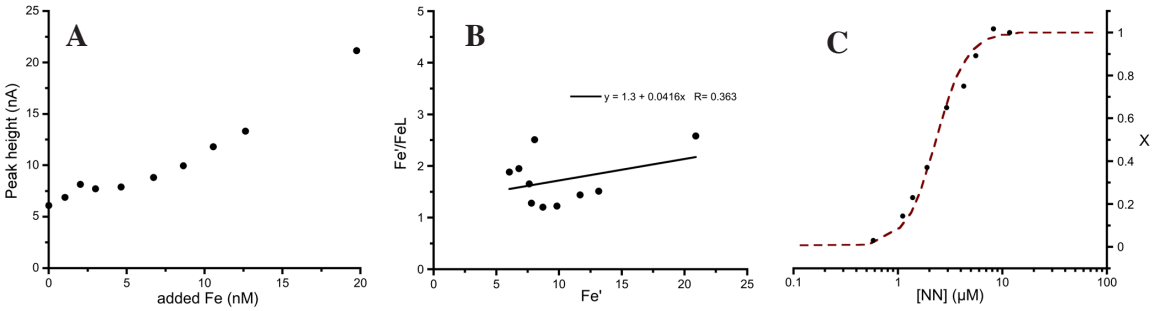

Figure 3.5: (A) Forward titration of a near shore sample (B) van den Berg/Ružić linearization of the data, using $[Fe_{NNmax}]$ = 9.23 nM as the Fe concentration at no Fe addition. (C) Reverse titration of the near shore sample (black circles) with the expected response for a sample with no ligands (red dashed line).

40 μM) as the initial Fe concentration in the titration, we find a very weak linear trend (r^2 = 0.132) in Fe′ vs Fe′/FeL for the forward titration data (Figure 3.5B). The poor fit for the linearisation leads to a high estimate for [L] of 24.0 nM and a weak conditional stability constant of $\log(K'_{Fe^{3+}L}) = 19.25$ ($\log(\alpha_{Fe^{3+}L}) = 11.6$). RT-CLE-ACSV of an aliquot of the same sample showed that any ligands present were weaker than the applied detection window in the method - i.e. the response resembled the curve for UVSW. This is consistent with previous results that showed that weak ligands below typical CLE-ACSV detection limits are important in coastal areas (Gerringa et al., 2007). The result is also consistent with the concept that at higher Fe concentrations, weaker but more highly concentrated ligands become more important in the stabilisation of Fe (Hiemstra and van Riemsdijk, 2006).

Given the poor fit of the forward titration linearisation and the low $\alpha_{Fe^{3+}L}$ (within an order of magnitude of the inorganic side reaction coefficient), it is quite likely that a false positive for the presence of ligands was obtained by forward titration for this data. In contrast, the RT-CLE-ACSV indicates that the equilibrium established between Fe and the AL could be described with confidence without invoking complexation by any other ligand (within the timeframe and detection window of the analysis). Our analysis shows that RT-CLE-ACSV is likely to give more convincing data than the forward titration for this type of sample (high ambient Fe) and we propose that RT-CLE-ACSV should be considered a very useful tool in the

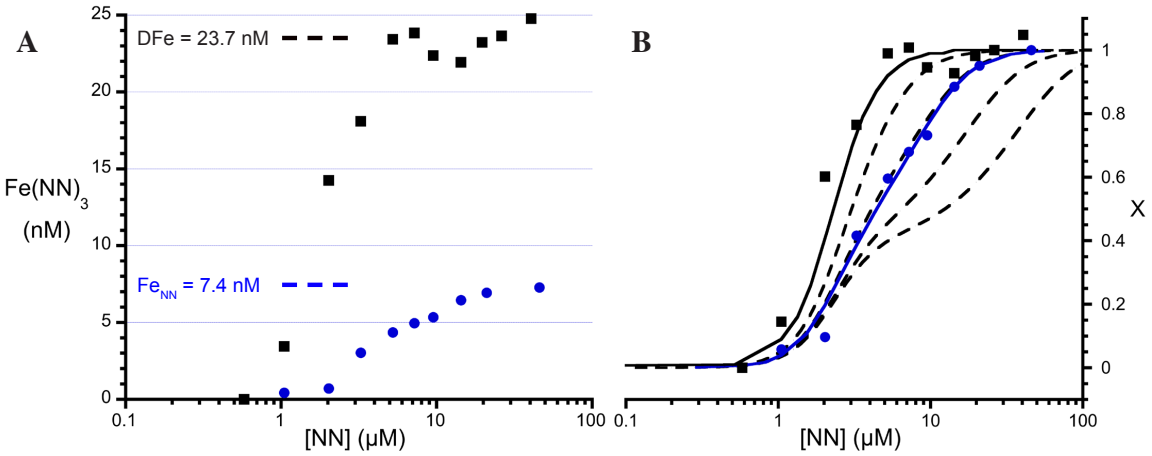

Figure 3.6: (A) Measured concentration of $Fe(NN)_3$ at varying concentrations of NN for a hydrothermal plume sample with different treatments. Black squares: stored at room temperature (pH 2) and UV irradiated; blue circles: stored frozen untreated. (B) The same titrations normalised to i_{pmax} for data fitting. The black line is the model output for seawater with no ligands, the blue line is the fitted curve for the untreated aliquot data. The dashed black lines are the model outputs for Fe_{NNmax} = 7.35 nM, [L] = 4.4 nM, $\log(K'_{Fe^{3+}L})$ = 19, 20, 21, 22.

assessment of Fe speciation in these types of waters.

3.4.5.2 Hydrothermal plume sample

An aliquot of the hydrothermal plume sample was stored at pH 2, UV-irradiated, adjusted to pH 7.90, buffered and analysed by RT-CLE-ACSV, resulting in a typical UVSW curve (Figure 3.6). The $Fe(NN)_3$ concentration estimated at i_{pmax} was equivalent to 23.7 nM Fe. This agrees well with the ICP-MS measured DFe concentration (22.5 ± 2.3 nM). A second aliquot was left untreated (frozen) before defrosting and analysis. The resulting RT-CLE-ACSV data had a flatter reverse titration curve (Figure 3.6B), and the model fitted the data with one ligand class with $K'_{Fe^{3+}L}$ = 1.10 ±0.59 x 10^{20} mol^{-1} and a ligand concentration of 4.38 ±0.64 nM Fe. Fe_{NN} (at 40 μM NN) was 7.39 nM, just 33% of the total dissolved Fe. A large portion of the DFe was thus inert to complexation with NN. The measured ligands were in deficit of Fe_{NN} and greatly in deficit of DFe, and analysis of this sample would not be possible by forward titration. The determined $K'_{Fe^{3+}L}$ is within the range of previously reported values for the deep sea (Gledhill and Buck, 2012;

Laglera and van den Berg, 2009) and is well within the detection window of the technique, so we have no reason to doubt the plausibility of this result. The implications of this work to hydrothermal Fe stabilisation will be discussed in a separate publication (Hawkes et al., 2013a).

3.5 Conclusions

We have demonstrated the reverse titration for Fe, and fitted experimental data to the theoretical equations using a model written in R. The model was most reliable when the ligand saturated the Fe_{NNmax} present in the sample, and when i_{pmax} was reached. However, an estimation of complex stability constant and ligand concentration was obtained when the ligand was in deficit of Fe_{NNmax} and when i_{pmax} was not reached in the titration. Only labile Fe (Fe_{NNmax}) is considered in the data manipulation, leading to a more accurate determination of the Fe ligand characteristics than use of DFe. If Fe_{NNmax} were routinely used in CLE-ASCV, estimated ligand binding constants and concentrations would tend to be lower.

All calculated stability constants in this work are slightly lower than previous reports (including the deep sea sample), but this is largely due to the different calibration calculation for the stability constant of $Fe(NN)_3$. The relative magnitude of other ligands (desferrixoamine B, deep sea ligands) to $Fe(NN)_3$ are very similar to previous reports, validating this technique as an alternative method of Fe speciation determination in high Fe environments.

1-nitroso-2-naphthol was used as the added, electroactive ligand as this ligand only binds with Fe as $Fe(NN)_3$, making the chemical equilibrium simple to model. In early tests with the ligand 2-(2-Thiazolylazo)-p-cresol (TAC), we found that interference of the $Fe(TAC)_1$ complex (Croot and Johansson, 2000) may have competed with $Fe(TAC)_2$ for Fe. Also, i_{pmax} was not reached in UV treated seawater after overnight equilibration ([TAC] = 40 μM, $\alpha_{Fe^{3+}TAC_2}$ = 3.6 x 10^{13}). Additionally, in experiments with added Fe, 30-70% of the added Fe was not labile to TAC after overnight equilibration (possibly due to hydrolysis/precipitation in the titration vials; Gerringa et al., 2007), while no losses were observed for NN.

Further experiments with more sensitive ligands or oxidative catalysts could be conducted to improve the detection limit of the method, and using an added ligand with a wider detection window would help in the determination of two ligands in a sample. Generally the limit of detection using NN is suitable for marine samples where [Fe] is greater than [L].

Chapter 4

The stabilisation and transportation of dissolved iron from high temperature hydrothermal vent systems

Contents

Abstract

Iron (Fe) binding phases in two hydrothermal plumes in the Southern Ocean were studied using a novel voltammetric technique. This approach, reverse titration - competitive ligand exchange - adsorptive cathodic stripping voltammetry, showed that on average 30 ± 21% of dissolved Fe in the hydrothermal plumes was stabilised by chemically labile binding to ligands. The conditional stability constant ($\log K'_{Fe^{3+}L}$) of the observed complexes was 20.61 ± 0.54 (mean ± 1 SD) for the two vent sites, intermediate between previous measurements of deep ocean ligands (21.4 - 23; Kondo et al., 2012) and dissolved weak estuarine ligands (< 20; Gerringa et al., 2007).

Our results indicate that approximately 7.5% of all hydrothermal Fe was stabilised by complexation with ligands. Furthermore, 47 ± 26% of the dissolved Fe in the plume existed in the colloidal size range (0.02 - 0.2 μm). Our data suggests that a portion (∼7.5%) of hydrothermal Fe is sufficiently stabilised in the dissolved size fraction (<0.2 μm) to make an important impact on deep ocean Fe distributions. Lateral deep ocean currents transport this hydrothermal Fe as lenses of enhanced Fe concentrations away from mid ocean ridge spreading centres and back arc basins.

4.1 Introduction

Iron (Fe) is an important and often limiting micronutrient in the world's oceans (Martin and Fitzwater, 1988). Dissolved Fe (DFe) concentrations in the surface ocean are typically <0.3 nM, and range between ∼0.2 - 1.2 nM in the deep ocean (>1000 m); the iron is buffered by strong organic ligands (De Baar and De Jong, 2001; Hunter and Boyd, 2007). The study of the sources, sinks and speciation of Fe is crucial to our understanding of the transport and bioavailability of this element. The supply of Fe to the world's oceans is poorly constrained, with atmospheric dust, rivers, sediments and remineralisation of sinking particles forming the main sources (De Baar and De Jong, 2001). Hydrothermal sources of stable DFe have recently been considered due to several observations of high DFe concentrations in the deep ocean close to tectonic spreading centres, often in regions containing elevated (hydrothermally sourced) ^{3}He (Fitzsimmons et al., 2013; Klunder et al., 2011; Kondo et al., 2012; Nishioka et al., 2013; Wu et al., 2011).

Iron is highly enriched in high temperature hydrothermal fluids as it is leached from host rocks during hydrothermal circulation of seawater. End-member concentrations can range from <2 μM (e.g. Menez Gwen, Mid Atlantic Ridge; Douville et al., 2002) to >10 mM Fe (e.g. Edmond vent site, Central Indian Ridge; Gallant and Von Damm, 2006). The total (dissolved and particulate) contribution of Fe to the deep ocean by high temperature hydrothermal vents is estimated to be 7.2 - 450 Gmol Fe yr^{-1} (Baker et al., 1993; Bennett et al., 2008; Elderfield and Schultz, 1996; Tagliabue et al., 2010), while the total DFe inventory of the ocean is estimated to be 800 - 1600 Gmol (De Baar and De Jong, 2001). The impact of hydrothermal vents on global DFe distributions is still poorly understood due to the high spatial (German and Von Damm, 2004) and temporal (Butterfield and Massoth, 1994; Campbell et al., 1988; Yücel and Luther, 2013) variability in hydrothermal fluid emissions, and the complexity of Fe speciation and removal in seawater.

A large portion of hydrothermal Fe is deposited close to vent sources as sulfide mineral phases (Mottl and McConachy, 1990) and the remaining Fe(II) is rapidly

oxidised and forms oxy-hydroxide particles (Feely et al., 1987; Field and Sherrell, 2000; German et al., 1990). However, Fe is often observed to oxidise or precipitate more slowly in hydrothermal plumes than predicted by laboratory kinetic studies, and this has been attributed to stabilisation of Fe(II) with organic matter and sulfides (Statham et al., 2005; Toner et al., 2009; Wang et al., 2012) and also stabilisation of Fe(III) in the dissolved phase by complexation with organic ligands (Bennett et al., 2008). Fine Fe containing particles (or 'colloids') are also considered to contribute to the observed enhanced dissolved (usually <0.2 or <0.45 μm) Fe concentrations (Field and Sherrell, 2000), and both oxy-hydroxide (Fe(III)) colloids and pyrite nano-particles (Fe(II)) have been detected in hydrothermal vent systems (Sands et al., 2012; Yücel et al., 2011).

The only study that has considered DFe complexation in hydrothermal plumes was restricted to analysis of samples from the edges of the distal plume. It was suggested that a small percentage (∼4%, 0.3 Gmol yr^{-1} globally) of hydrothermal Fe was transported to the deep ocean as DFe (Bennett et al., 2008). Here, we used a new voltammetric speciation technique (Chapter 3) to enable investigation of Fe speciation in the core of two hydrothermal plumes, where Fe is potentially saturating organic complexes. We also considered the differences between 'dissolved' Fe (<0.2 μm), 'soluble' Fe (<0.02 μm) and 'chemically labile' Fe (the Fe fraction that is complexed with an added electro-active ligand) - thus combining the study of physical and chemical speciation of Fe for the first time in hydrothermal plume systems.

The two vent sites (E2 and E9N; Rogers et al., 2012) are situated on the East Scotia Ridge (ESR) in the Southern Ocean and were sampled in 2010 for DFe ligand complexes. E9N was re-visited in 2011 to collect samples to determine the colloidal Fe (DFe minus soluble Fe) distributions. Sampling was conducted over a range of seawater to vent fluid mixing ratios (∼200 - 160,000). However, due to the rapid dilution of vent fluid in hydrothermal buoyant plumes, the sample matrix (major ions, pH, temperature, etc.) was only ever slightly different from ambient seawater. Our aim was to investigate whether Fe in hydrothermal plumes is complexed by

'ligand' phases that are co-diluted with Fe from the vent or by ambient ligands already present in the local deep seawater. We discuss the implications of our results for the transport of hydrothermal Fe to the deep ocean.

4.2 Materials and methods

4.2.1 Hydrothermal plume detection and sampling

The East Scotia Ridge (ESR) and the E2 and E9N vent sites are described in Chapter 2. Samples were collected and filtered on board the RRS *James Cook* during two cruises in the Southern Ocean, along the East Scotia Ridge (ESR) in 2010 (E2 and E9N; cruise JC042) and 2011 (E9N only; cruise JC055). The hydrothermal plume was detected and sampled using a Seabird +911 conductivity, temperature and depth (CTD) profiler system that was mounted on a titanium frame that holds 24 trace metal clean 10 litre OTE (Ocean Test Equipment) water sampling bottles. The frame was also equipped with a light scattering sensor (LSS) and a bespoke Eh detector (Ko-ichi Nakamura).

The buoyant part of the hydrothermal plume was identified by positive temperature and particle anomalies and a negative Eh anomaly, while the neutrally buoyant plume was identified by a positive particle anomaly and negative temperature and Eh anomalies at 350-400 m above the seafloor (Figure 4.1). The plumes appeared to change position and intensity daily (based on the LSS anomaly, see various CTD profiles in Figure 4.1), probably due to variations in deep water current speed and direction. The ESR does not have an axial valley, so there is no seafloor feature to confine the neutrally buoyant plume, enabling it to disperse in varying directions according to complex deep-sea currents. As a result, the hydrothermal plumes can be sampled at many levels of dilution over small spatial areas above the two vent fields.

Four 'near vent' plume samples were taken from diffuse flow areas and the first few meters of buoyant plume rise (identified visually) using five 1.2 litre Ocean Test Equipment (OTE) bottles on the remotely operated vehicle (ROV) *Isis*. The five

bottles were closed simultaneously and combined (6 litres) into one large OTE bottle and treated identically to the CTD profiler bottles, as described below.

A background CTD cast was also conducted at 59°40.898 S, 33°06.181 W, where no water column anomalies were observed. This site had a similar water depth (∼2500 m) to the hydrothermal sites, but was >50 km to the west of the ESR, and presumably beyond any strong influence of the dispersing plume. Samples were taken at depths equivalent to those of the buoyant and neutrally buoyant plumes at E9N (2350 and 2000 m, respectively). The background deep seawater Fe concentration averaged 1.7 nM in 6 OTE bottles (range 0.94 - 2.59 nM), which is consistent with other studies further to the east and west in the deep southern Atlantic (0.4 - 0.6 nM at 0°W (Klunder et al., 2011), 0.4 - 2.8 nM at 6°W (Loscher et al., 1997) and 1.6 - 4.2 nM close to the South Orkney islands at 48.23°W (Nolting et al., 1991).

4.2.2 Assessment of in-situ pH using alkalinity and dissolved inorganic carbon

Dissolved inorganic carbon (DIC) and alkalinity were measured using a VINDTA 3C analyser (Miranda). Nutrients (phosphate and silicate) were measured by Seal QuAAtro, and these data were used to calculate in situ pH using CO2sys (Lewis and Wallace, 1998).

4.2.3 Filtration and analysis of size fractions of Fe and Mn

Dissolved (500 ml, <0.2 μm) and particulate (>0.2 μm) metals were separated by filtration of seawater using a polycarbonate membrane filter (0.2 μm, Whatman) under gentle pressure using filtered oxygen free nitrogen gas. Separate aliquots of filtered seawater were frozen for reverse titration - competitive ligand exchange - adsorptive cathodic stripping voltammetry (RT-CLE-ACSV) analysis (see Chapter 3). The entire bottle contents (10 litres) was filtered for particulate material, and the OTE bottles were shaken before filtration finished to attempt to recover all material. It is still possible that larger material settled to the bottom of the OTE

bottle (beneath the tap fixture) and was not recovered. On cruise JC055 (2011) at the E9N site, 'soluble' (<0.02 μm) metals were separated by filtration using syringe filters (Anotop; Whatman) by peristaltic pumping at < 1 ml min^{-1}. We note that the actual cut-off size of these filters may be significantly samller than 0.02 μm (Chen and Wang, 2004). The following wash and sampling was conducted through two syringe filters (0.1 μm and 0.02 μm) in series: a pre-wash of 30 ml pH 2 de-ionised water (MQ, Millipore, >18.2 mΩ cm^{-1}; acidified with ultrapure HCl) followed by rinsing with de-ionised water for at least 4 hours before sampling, then 20 ml of sample seawater was flushed through the filters and discarded and 40 ml of sample seawater was collected. pH 8 adjusted de-ionised water was filtered in the same way, and the extracted Fe concentration was below the detection limit (2.33 nM). Colloidal Fe was assumed to be the difference in 'dissolved' and 'soluble' Fe, as in other studies (e.g. Wu et al., 2001).

All filtered seawater samples from the CTD profiler were acidified to pH 1.9 with sub-boiled nitric acid (Optima, Fisher Scientific). On shore, dissolved metals were pre-concentrated from 100 ml of sample (30 ml for soluble Fe) by mixed ligand extraction (Bruland et al., 1979) and analysed using inductively couple plasma mass spectrometry (ICP-MS; Thermo Scientific X-series). De-ionised water was used to determine the procedural blank (Mn = 0.08 nM, Fe = 0.62 nM), the limit of detection (L.O.D.) (3σ of blank, n = 27) for Mn and Fe was 0.14 and 0.70 nM, respectively. For the lower volume soluble (<0.02 μm) Fe samples, the L.O.D. was 2.33 nM. The vast majority of dissolved and soluble samples were higher than the L.O.D. for Fe. Accuracy was assessed using NASS-5 certified seawater (measured Fe: 3.74 $\pm$ 0.62 nM (n = 7), certified 3.70 $\pm$ 0.625) and precision was determined with NASS-5 and an in-house standard (8.5 - 16.6% depending on Fe concentration). The near vent samples taken by the ROV *Isis* had very high concentrations of Fe and Mn and were directly analysed by ICP-MS (X-series, Thermo Fisher Scientific) following dilution (100x) into 3% sub-boiled nitric acid containing an internal standard of Be and In (20 ppb and 10 ppb).

Particulate material (from 10 L of seawater) was stored frozen on the polycarbonate

membrane filters, which were cut in half with ceramic scissors, and one half of each was digested for 3 days at 150℃ in sub-boiled concentrated nitric acid in a PTFE bomb (German et al., 1991) (the other half was stored for additional analysis). Filter material remaining after the acid digestion was soaked with a further 10 ml of sub-boiled concentrated nitric acid. The acid was removed by drying in a PTFE bomb on a PTFE coated hot plate set at 90℃, then the dried samples were diluted in 3% sub-boiled nitric acid and analysed by ICP-MS. The L.O.D. (3σ of average blank filter) for Mn and Fe were 1.4 and 78.4 pM, respectively.

4.2.4 Determination of Fe speciation by RT-CLE-ACSV

The forward titration technique is typically used to determine Fe binding ligands in seawater but is not appropriate for use in environments with excess Fe or large quantities of inert dissolved Fe (Gledhill and Buck, 2012; Laglera and van den Berg, 2009), and as such has limited use in hydrothermal environments (Bennett et al., 2008). The reverse titration -CLE-ACSV approach allows analysis of ligands at equal or lower concentrations than chemically labile Fe (Chapter 3). The theory has been previously described for analysis of Cu, Fe(II) and Fe(III) binding ligands (Hawkes et al., 2013b; Nuester and van den Berg, 2005; Statham et al., 2012).

Samples (250 ml) were filtered (0.2 μm pore size, polycarbonate, Whatman) and stored frozen at ambient pH. On shore they were defrosted at 4℃ (close to their in-situ temperature) and shaken vigorously before preparation of the titration. The titration was carried out and Fe_{NNmax} was determined as described in Chapter 3.

The near vent samples taken using the ROV *Isis* all had DFe concentrations in excess of 100 nM (range 290 - 1430 nM). The method had to be modified in these cases because the data manipulation relies on [NN] being in large excess over [Fe_{NNmax}]. These samples were diluted in de-ionised water to three different salinities (20x, 10x and 5x dilution) and analysed in the same way as described above (with a 120 s deposition time). The change in salinity was not found to affect the calculated value of $K'_{Fe^{3+}L}$, but did affect the calculated (i.e. zero dilution) concentrations of

Fe_{NNmax} and L - which increased at lower salinity. The full data can be found in Appendix D, here we present the calculated average result for $K'_{Fe^{3+}L}$ and values for [Fe_{NNmax}] and [L] calculated from the 5x dilution.

4.2.5 Data fitting

The experimental data were all fitted to Equations 3.8 and 3.11 (Chapter 3) using a non-linear regression code package in the open source software R. This process is described in detail in Appendix B. The code is available online (Hawkes et al., 2013b). $\beta_{Fe(NN)_3}$ (Equation 3.2) was 5.12 x 10^{26} under our typical experimental conditions (Chapter 3), and the value was adjusted to account for salinity (Gledhill and van den Berg, 1994) in the high Fe samples that were diluted.

4.3 Results

The temperature, LSS and Eh profiles for the two hydrothermal plumes E2 and E9N are shown in Figure 4.1. The E2 neutrally buoyant plume (NBP) had a weaker LSS anomaly that was generally more variable than for the plume of E9N. These differences may be due to differences in Fe oxy-hydroxide and sulfide abundance (which have different light attenuation properties) rather than vent output (Baker and Massoth, 1987). The plume rise was ∼400 m at E2 and ∼350 m at E9N, both of which are consistent with the obtained end-member temperatures (Table 2.1) and water column densities (data not shown) using the plume rise model of Turner (1973). Iron binding phases were successfully determined within the applied detection window using RT-CLE-ACSV in samples from both the E2 and E9N plumes, including the near vent samples. The average ligand concentration was 25 ± 15% of the DFe concentration at E2 and 39 ± 27% of DFe at E9N. The stability constant ($\log K'_{Fe^{3+}L}$) of the Fe-ligand complexes averaged 20.51 ± 0.45 (mean ± 1 SD) at E2 and 20.79 ± 0.65 at E9N (see Figure 4.2 for three examples of titration data). No trend in $\log K'_{Fe^{3+}L}$ was observed with dilution of the vent fluid (Figure 4.3), including in the near vent samples, meaning that the binding strength of the Fe-ligand complexes was not related to their concentration or distance from the

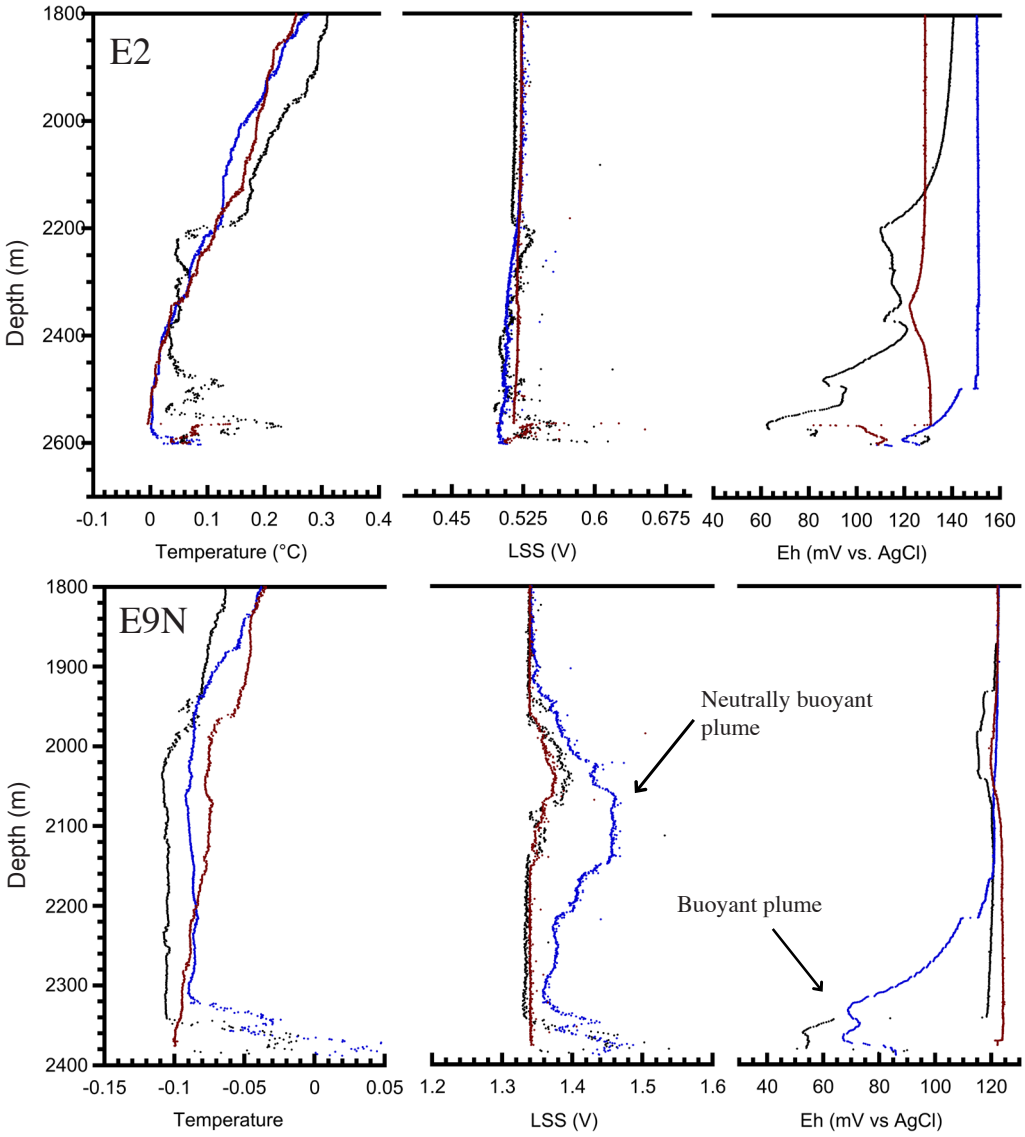

Figure 4.1: Temperature, LSS and Eh profiles at depth >1800 m for three CTD casts (indicated by different colours) at different times but similar positions from E2 and E9N. The negative temperature anomaly in the neutrally buoyant plume is due to entrainment of colder seawater from deeper in the water column. The light attenuation anomaly is due to the presence of particles, and the negative Eh anomaly due to the presence of reduced species (HS^-, Mn^{2+}, Fe^{2+}).

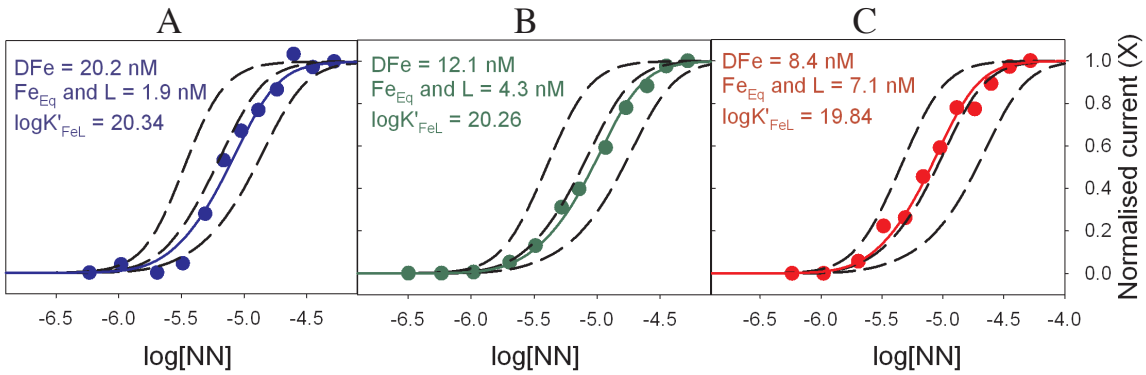

Figure 4.2: RT-CLE-ACSV data and model outputs for three samples: A: E2 buoyant plume, B: E2 neutrally buoyant plume, C: E9N buoyant plume. Circles show the experimental data and the solid lines the model fit. Dashed lines show the model fit for $\log K'_{Fe^{3+}L}$ = 19, 20 and 21 (left to right) for the same concentration of Fe and L.

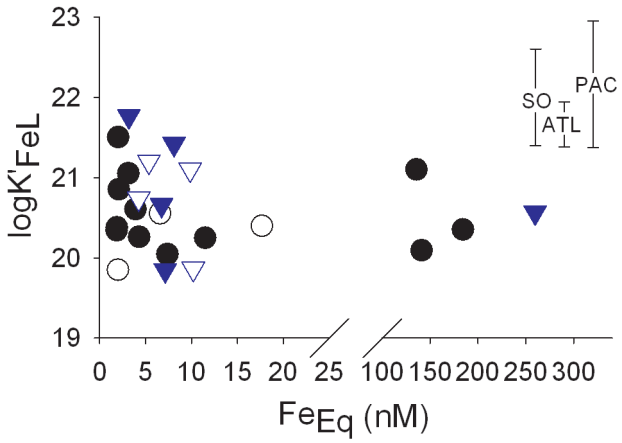

Figure 4.3: $\log K'_{Fe^{3+}L}$ plotted against electrochemically labile Fe (Fe_{NNmax}) in the plume and near vent samples. We found no trend in stability constant with Fe concentration. Black circles: E2, blue triangles: E9N. Data which were poorly fitted by the RT-CLE-ACSV model are included as unfilled symbols. The range of results previously reported in the (non-hydrothermal) deep sea from the Southern Ocean (SO), Atlantic (ATL) and Pacific (PAC) are shown for comparison. (Boye et al., 2010; Croot et al., 2004; Cullen et al., 2006; Kondo et al., 2012; Rue and Bruland, 1995).

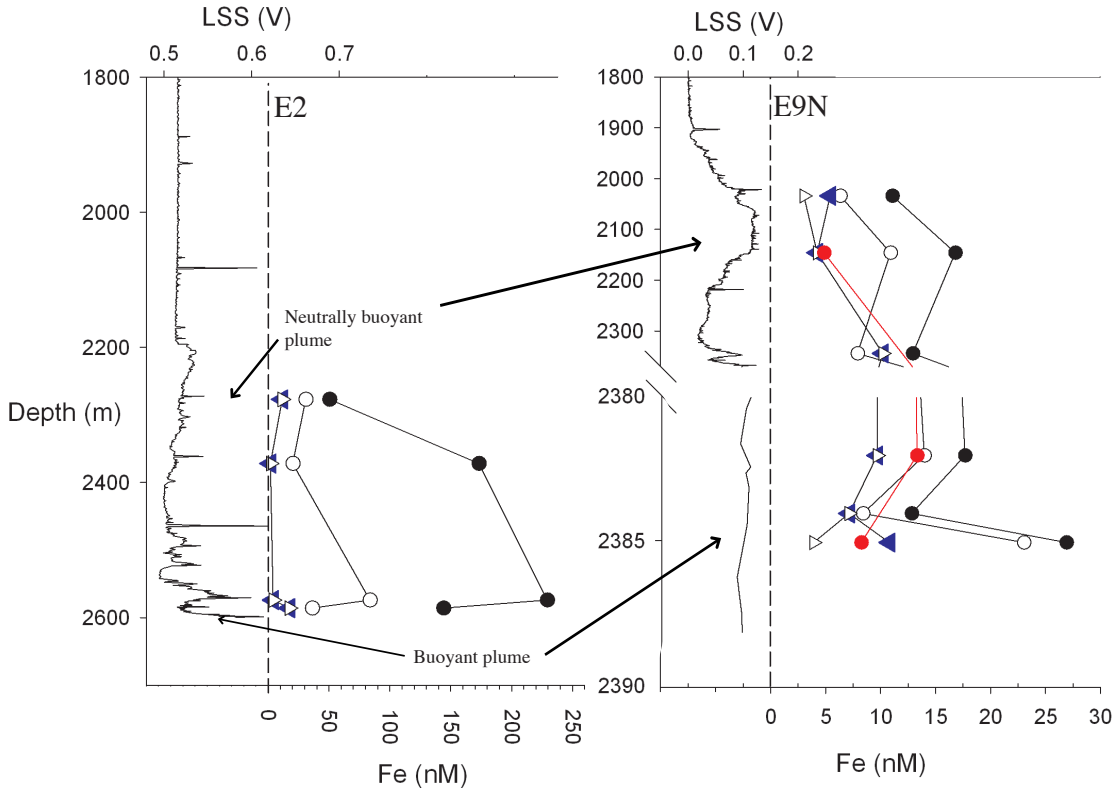

Figure 4.4: Example profiles of LSS and Fe at E2 (Station CTD3) and E9N (Station CTD424). Filled black circles: total (dissolved + particulate) Fe, unfilled black circles: dissolved Fe, filled red circles: soluble Fe, filled blue triangles: Fe_{NNmax}, unfilled black triangles: Fe binding ligands. Note the break in scale on the depth axis for E9N.

vents. The E2 plume contained a far greater concentration of Fe in the dissolved and particulate phases than E9N (Figure 4.4), but the E2 and E9N sites were not statistically different in $\log K'_{Fe^{3+}L}$ or L:Fe ratio (as demonstrated by a large overlap of values), suggesting these factors may be independent of DFe and total Fe concentrations between sites. The percentage of CFe (0.02 μm - 0.2 μm) in the DFe pool at E9N ranged between 5 and 82%, and averaged 47 $\pm$ 25%. The concentration of CFe was highest in the middle (47% of DFe) and lower (82%) portion of the NBP compared with the top (26%) - which contained a larger portion of soluble Fe (Figure 4.5). The labile Fe concentration (Fe_{NNmax}, occasionally higher than L) averaged 26 $\pm$ 15% of DFe at E2 and 47 $\pm$ 27% of DFe at E9N.

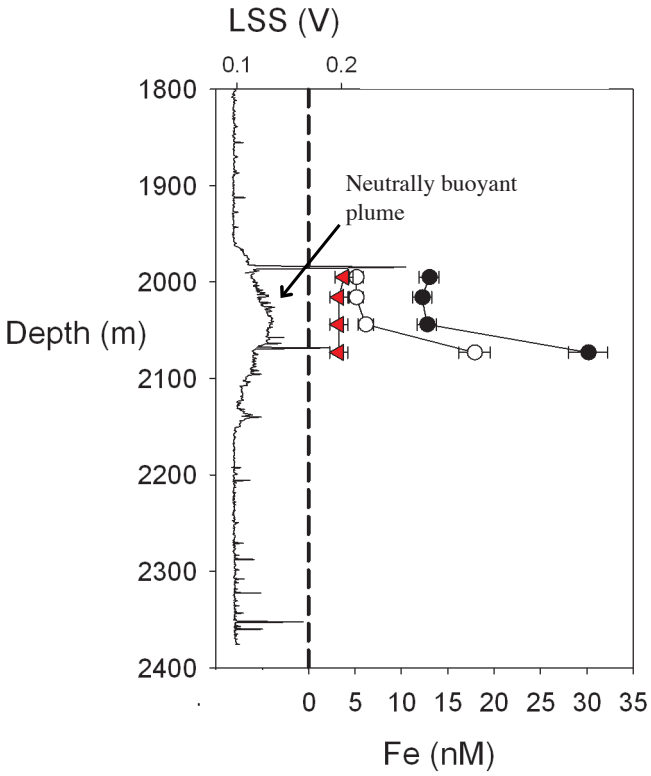

Figure 4.5: Depth profile of Fe size fractions in the neutrally buoyant plume at E9N (Station CTD428). Filled black circles: total (dissolved + particulate) Fe, unfilled black circles: dissolved Fe, red triangles: soluble Fe.

4.4 Discussion

4.4.1 Fe speciation in the hydrothermal plumes

The typical Fe concentrations in the plume were low in comparison with many other vent sites which have been studied for Fe speciation (e.g. the 5°S Mid Atlantic Ridge plumes; Bennett et al., 2008, the Edmond vent plume; Sands et al., 2012, the Rainbow vent plume; Edmonds and German, 2004), and this may be the result of relatively high sulfide concentrations in the East Scotia Ridge vent fluids, removing a large portion of the Fe in the early buoyant plume (Field and Sherrell, 2000; Klevenz et al., 2011; Mottl and McConachy, 1990). This was particularly the case at E9N, where low chloride concentrations suggest a vapour phase was sampled after subseafloor phase separation. This process favours gases such as hydrogen sulfide over cations such as Fe, and may also lead to a higher proportion of Fe being precipitated as sulfides in the early plume.

Our results showed that a portion of DFe was complexed by ligands in all parts of the hydrothermal plumes. Iron binding phases were typically equal to (or more concentrated than) Fe_{NNmax}, and Fe_{NNmax} was generally substantially less than DFe (Figure 4.4), showing that not all DFe was electrochemically labile under our experimental conditions. The observed Fe_{NNmax} fraction is operationally defined by the concentration of added ligand used (here: 40 μM NN), the binding strength of NN to Fe (β_{FeNN_3}; 5.12 x 10^{26} mol^{-1}) and also the kinetics allowed during of overnight equilibration. Natural complexes with a binding coefficient α_{FeL} ($[L]K'_{Fe^{3+}L}$) which are much greater than α_{FeNN_3} ($[NN]_3\beta_{FeNN_3}$) or have similar strength to the inorganic species of Fe (e.g. hydrolysis products) will not be detected. This may include sulfide ligands (e.g. SH^-, see below) and the very weak class of ligands previously detected in estuarine environments (Gerringa et al., 2007), which is a comparable marine environment (i.e. with steep chemical gradients; Figure 4.6). Ligands that are too strong to be detected by this technique may also have been important in stabilising Fe - and crystalline colloidal phases and nano-pyrite particles are likely to constitute the 'inert' Fe pool. The $\log K'_{Fe^{3+}L}$ values averaged 20.51 at E2 and 20.79

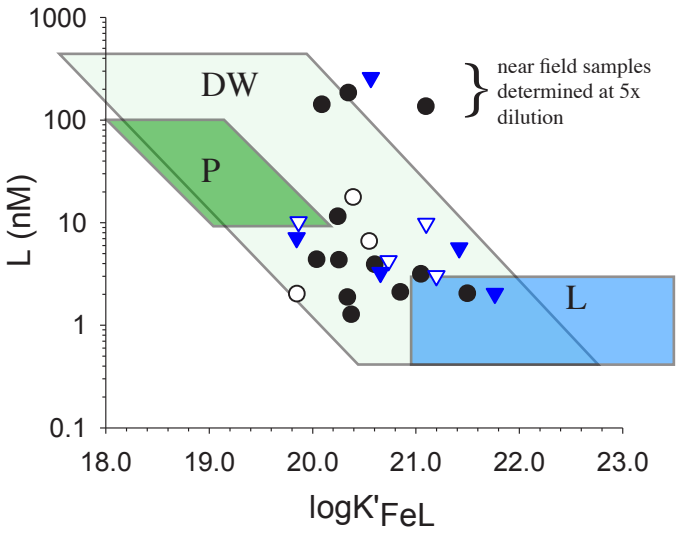

Figure 4.6: Concentrations of Fe binding phases plotted against stability constant at E2 and E9N. In addition to the data (black circles: E2, blue triangles: E9N), typical ranges of the same factors are shown for L in the deep Southern Ocean (Boye et al., 2001; Croot et al., 2004) and for 'P' the weak ligand suggested to exist in high concentrations in an estuary in Gerringa et al. (2007).

at E9, 20.61 combined, and these are lower than most of the complexes reported for the deep ocean (Figure 4.3, Boye et al., 2010; Croot et al., 2004; Cullen et al., 2006; Kondo et al., 2012; Rue and Bruland, 1995). Marine Fe binding ligands exist in an un-interrupted continuum of Fe binding strengths, and those detected may only depend on the detection window of the technique used (Hassler et al., 2013; Hiemstra and van Riemsdijk, 2006). In this study our detection window ($\alpha_{\mathrm{FeL}} \sim 10^{9.8}$ - $10^{13.7}$) is bound by the concentration of Fe in the sample and by the range of $\mathrm{FeNN_3}$ concentrations that can practically be determined. We constrain this detection window by requiring 80% of i_{pmax} to be reached over the course of the titration for data fitting purposes. Our detection window is thus lower than that commonly applied in forward titrations ($\alpha_{\mathrm{FeL}} \sim 10^{12.6}$ - $10^{14.6}$). However, previous studies have reported an inverse relationship between ligand binding strength and ligand concentration (Hiemstra and van Riemsdijk, 2006; Stockdale et al., 2011), so that at higher Fe concentrations, such as those observed in this study, weaker ligands become more important for stabilising Fe in solution. The ligand phases reported here for hydrothermal plumes are indeed weaker than typically detected open ocean

ligands, and make up the weakest of the 'L2' set of ligands which are often measured in the deep ocean (Gledhill and Buck, 2012; Hunter and Boyd, 2007; Laglera and van den Berg, 2009; Rue and Bruland, 1995). However, differences between the forward and reverse titration techniques may preclude direct comparison of the obtained $K'_{Fe^{3+}L}$. The important implications of our findings are that some portion of hydrothermal DFe was found to be sufficiently labile to exchange with NN and that the obtained $K'_{Fe^{3+}L}$ did not appear to change as the plumes developed or between the two sites.

4.4.2 The effect of Fe oxidation state, pH and hydrothermal constituents on the in-situ speciation

The in-situ speciation of Fe may potentially be different than that detected under our experimental conditions, in which the temperature, pH and pressure are all modified and any reduced species (e.g. Fe^{2+}, $H_2S_{(aq)}$) were given time to oxidise. The ambient pH in the deep Scotia Sea was 7.90 (very similar to the buffered pH) but temperature was ∼23℃ colder, thereby reducing the inorganic side reaction coefficient (Hassler et al., 2013; Schlosser et al., 2012). The samples were also frozen, potentially allowing aggregation of colloidal phases (Schlosser et al., 2011). The hydrothermal fluid constituents of the plume may also affect the Fe speciation, as the fluid is acidic and has a very different ionic composition. However, only hydrothermal constituents that are highly enriched ($> 10^5$ x) over seawater have significantly higher concentrations in the plume, particularly once it has been emplaced to neutral buoyancy ($\sim 10^4$ x dilution; Lupton et al., 1985). As a result, only pH is sufficiently different from ambient seawater to have an important affect on the Fe speciation. The range of pH of the plume samples in this study (calculated from dissolved inorganic carbon and total alkalinity; Lewis and Wallace, 1998) was 7.5 - 7.9 (total scale). The lowest near vent sample had an in-situ pH of 7.0. The solubility and speciation of Fe(III) is critically dependent on pH (Gledhill et al., 1998; Millero et al., 2009; Shi et al., 2010) due to competition for Fe^{3+} by L^- and OH^-. At lower pH Fe hydrolysis is decreased (Liu and Millero, 2002) and more free iron (Fe^{3+}) is available for ligand complexation. Ligands that have acidic binding groups that are not protonated

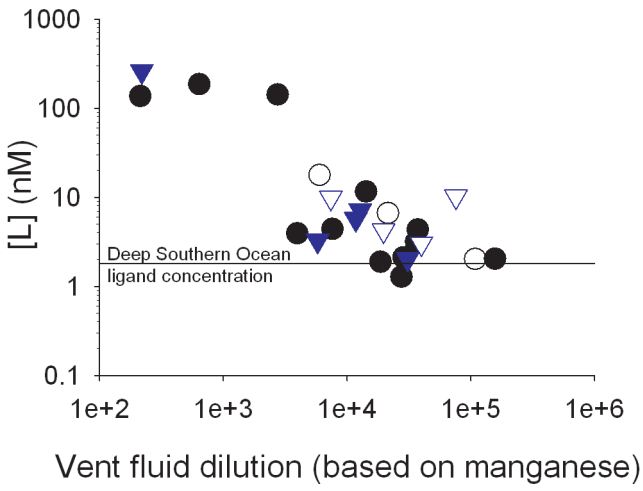

Figure 4.7: Concentration of Fe binding phases (L) plotted against dilution of pure vent fluid with seawater (based on dissolved manganese). Black circles: E2, blue triangles: E9N. Data which were poorly fitted by the RT-CLE-ACSV model are included as unfilled symbols. Note that [L] for the near vent samples was calculated from a sample which was diluted 5x with de-ionised water. Typical deep southern ocean ligands are shown as a horizontal line (from Croot et al., 2004).

in seawater form stronger complexes, whereas no change in conditional stability constant is observed for protonated ligands (Shi et al., 2010). When the samples are buffered and free Fe^{2+} is allowed to oxidise over the course of preparation, they are driven towards thermodynamic equilibrium and more typical seawater conditions. The experimental results are therefore more representative of the eventual products of the reaction of hydrothermal fluid with seawater rather than the speciation at the exact time and location of sample collection in the plume.

4.4.3 The source and nature of FeL

Our results showed that the amount of bound Fe (FeL) increased with dissolved Mn, indicating that the hydrothermal vents act as a source of FeL (Figure 4.7). The observation that FeL is diluted with the plume and thus appears to have a plume source raises questions about the nature of FeL. Firstly we consider the hydrothermal Fe binding phases in vent plumes to be classically organic in nature (Bennett et al., 2008) with a 1:1 Fe:L binding ratio. The source of these ligands is unlikely to

be directly from the high temperature vent, but rather lower temperature diffusive areas of venting which are found adjacent to high temperature hydrothermal vents and may contribute up to 98% of the total hydrothermal mass flux (Baker et al., 1993). Higher concentrations of dissolved organic carbon (DOC) compared with ambient deep seawater and end-member fluid (i.e. 48 μM compared with 36 μM and 15 μM, respectively, Lang et al., 2006) have been observed in these areas. It has been suggested that this material is more labile (more reactive and with a greater variety of functional groups) than the typically recalcitrant deep ocean DOC (Karl, 1995; Lang et al., 2006), and may have the functionality to chelate vent sourced DFe (Bennett et al., 2008). Various studies have considered the distribution and activity of bacterial populations in hydrothermal plumes (e.g. Bennett et al., 2013; De Angelis et al., 1993; Karl, 1995) usually concluding that bacteria metabolise methane in hydrothermal plumes, producing particulate and dissolved organic matter (POM, DOM). Some of the resulting DOM may have a capacity to bind Fe, and, furthermore, some bacteria may actively produce dissolved organic ligands as a mechanism for sequestering Fe (Gledhill and Buck, 2012). While the actual amount of organic matter produced by bacteria from methane is probably as low as that entrained from diffusive areas of venting (Bennett et al., 2013), these mechanisms may well be important in the chemically rich plume. If the DOC composition reported in Lang et al. (2006) are typical and a maximum of 98% of the hydrothermal input to the plume was from lower temperature venting then the ratio of hydrothermal C to Fe in the plume could be up to 1.4:1 (Equation 4.1).

$$\frac{[\mathrm{C}_{plume}]}{[\mathrm{Fe}_{plume}]} = \frac{[\mathrm{C}_{HT}]x_{HT} + [\mathrm{C}_{LT}]x_{LT}}{[\mathrm{Fe}_{HT}]x_{HT} + [\mathrm{Fe}_{LT}]x_{LT}} \tag{4.1}$$

Where x is the fractional mass proportion of high temperature (HT) and low temperature (LT) fluids. This level of DOC input (< 1 μM) would not typically be detected by DOC analysis; e.g. Bennett et al. (2011), and could help to support some stabilisation of Fe. However, the actual concentration of ligand molecules which could be provided (requiring several carbon atoms) may be low, and there is some dispute about the amount of diffuse water that is entrained into buoyant

plumes (German et al., 2010). It is therefore unlikely that FeL is dominated by compounds that can be considered classically organic.

A second explanation for the apparent presence of increased FeL levels in the hydrothermal plumes is that deep ocean water contains a relatively high concentration (10-100 nM) of weak organic or inorganic ligands, which are not typically detected by cathodic stripping voltammetry techniques (Croot and Heller, 2012; Gerringa et al., 2007). After overnight equilibration of our samples, any such ligand phase (which would often be in excess of Fe_{NNmax}) would enter into binding competition with the added ligand for Fe_{NNmax}. This may explain the low stability constant detected in our experiments. If this is the case, the relative kinetics of Fe ligand binding (Croot and Heller, 2012; Witter et al., 2000; Wu and Luther, 1995) and Fe precipitation may play a crucial role in the amount of Fe actually complexed in hydrothermal plumes before hydrolysis and precipitation.

Sulfide ligands may also be important in these environments, where reduced sulfur species can temporarily exist in the presence of oxygenated seawater. The ligand bisulfide (SH^-) has complexing capacity for several metals including Fe(II) (Luther et al., 1996) but the stability constant for $FeSH^+$ ($\log\beta_1$ = 5.1-5.5) and $Fe_2SH_3^+$ ($\log\beta_2$ = 10.1-11.8) are weak in comparison to the ligands detected in this study (Luther and Ferdelman, 1993; Luther et al., 1996). Additionally, the Fe and sulfide in some kinetically labile complexes may oxidise over the course of sampling, storage and equilibration during the preparation of the titration. These complexes may therefore be important in the early stages of venting, where Fe and S^{2-} are in similar concentrations, but less important as the plume disperses into the deep sea and under our analytical laboratory conditions.

Iron sulfide compounds (e.g. pyrite nanoparticles) are now recognised to be important in the dissolved phase in hydrothermal plumes (Yücel et al., 2011), particularly in high sulfide vent sites. These particles probably form a large part of the 'inert' and possibly some of the 'labile' DFe fraction, although the reactivity of Fe(II) in nano-particulate pyrite and organic matrices (Toner et al., 2009; Yücel et al., 2011) is unknown. The chemical reactivity of Fe sulfide phases deserves further atten-

tion, given their apparent pervasiveness in hydrothermal environments (Gartman and Luther, 2013).

Lastly, we consider a mechanism similar to the 'onion' concept of Mackey and Zirino (1994), which describes Fe binding involving aggregates with multiple layers of coordination bonds. A portion of Fe may form weakly bound aggregates (colloids) that are electrochemically labile, but are not technically bound in individual coordination bonds with singular 'organic ligands' as described in other theories (Croot and Johansson, 2000; Gledhill and van den Berg, 1994; Rue and Bruland, 1995). Colloids form when dissolved metal ions rapidly coagulate together by sorption, due to the attractive electrical charge of ionic surfaces (Honeyman and Santschi, 1989). Colloidal phases form more quickly than larger, filterable material because coagulation between larger particles proceeds at a slower rate than surface sorption (Farley and Morel, 1986; Honeyman and Santschi, 1989, 1991). Iron also has a strong tendency to form amorphous colloidal phases with organic matter (Hunter and Liss, 1982; Moore and Braucher, 2008; Mosley et al., 2003), and this process would be particularly likely in the turbulent hydrothermal plume where physical and chemical gradients are steep. This theory is supported by our observations of enhanced concentrations of Fe colloids in the E9N plume that corresponded well with the average concentration of Fe binding phases (colloids = 47% and L = 39% of total DFe). We assume here that hydrothermal CFe is made up of a mixture of amorphous oxyhydroxide colloids (Sands et al., 2012), nano-pyrite clusters (Luther and Rickard, 2005; Yücel et al., 2011) and colloidal-sized FeL (Boye et al., 2010; Cullen et al., 2006). Although the 'onion' model as described by Mackey and Zirino considers adsorption of metals onto organic colloids in the euphotic zone of the oceans, we consider this theory useful for explaining our results. Future Fe speciation studies in hydrothermal settings should aim to separate truly soluble FeL species from all dissolved FeL species as previously reported (Boye et al., 2010; Chen and Wang, 2004; Cullen et al., 2006) in order to more closely assess the role of colloids in stabilising hydrothermal Fe inputs.

Our observation that a large portion of hydrothermal Fe rapidly forms colloids in the

plume is consistent with experimental studies where high concentrations of Fe were added to organic rich seawater (Boye et al., 2005; Nishioka et al., 2005). Observations of natural Fe inputs (rivers, dust deposition, coastal upwelling) to seawater also show that a large portion of new Fe forms colloids (Benoit et al., 1994; Bergquist et al., 2007; Sanudo-Wilhelmy et al., 1996; Ussher et al., 2010). Coastal upwelling of Fe rich water also leads to a large variation of partitioning between soluble and colloidal Fe due to redox and biological processes (Ussher et al., 2010).

The mechanism of stabilisation of Fe by 'onion' aggregation (Mackey and Zirino, 1994) we propose here is consistent with theory and observations made to date. This mechanism of Fe binding may be much more widespread than just in hydrothermal systems, and could be a crucial control on Fe distributions in many parts of the ocean.

4.4.4 The transport and fate of Fe from hydrothermal systems

Regardless of the nature of FeL, our data suggest that a large portion (30%) of DFe in hydrothermal plumes exists in a chemically labile form that is available for transportation by deep ocean currents. In the E2 and E9N plumes, this corresponds to 10.1% of total hydrothermal Fe (E2), 9.0% (E9N) or 9.72 ± 7.2% (combined), based on the following formula:

$$\text{mean \% Fe stabilised} = \sum_{x} \left(\frac{\text{FeL}_x}{\text{TFe}_{hydrothermal}} \times \frac{\text{TMn}_{hydrothermal}}{\text{Mn}_\text{x}} \times 100 \right) \quad (4.2)$$

This relies on conservative mixing of Mn, which may be considered a maximum estimate as some Mn is oxidised by bacteria and on the surfaces of particles in the plume (Cowen and Li, 1991; Davies and Morgan, 1989; Dick et al., 2009), and Mn may also react with dissolved sulfide to form sulfide particles (Breier et al., 2012). If only 60% of the vent emitted Mn remained in the NBP samples (and 100% in the buoyant plume samples (Klinkhammer et al., 1986), the amount of hydrothermal Fe stabilised for the two sites may be revised to 7.5 ± 7.5%. This result has a high level of uncertainty due to the complexity, irregularity and turbulent nature of

hydrothermal plumes (Lupton et al., 1985).

The figure may also be considered as a minimum estimate, as other (kinetically inert) phases are also available for transport, and may in fact be scavenged less quickly from solution onto particles due to their lower reactivity. We have little experimental information about the nature of Fe species in the dissolved phases that are not part of the Fe_{NNmax} fraction, and these species merit further investigation. We assume here that a large portion is purely inorganic (colloidal) Fe oxy-hydroxides (Field and Sherrell, 2000; Sands et al., 2012) and pyrite nano-particles (Yücel et al., 2011).

Regarding the behaviour of Mn, we noticed that in samples which were strongly diluted (>20,000 x) with seawater, the DFe concentrations appeared to tend toward a concentration of approximately 5-10 nM above background (Figure 4.8). The implications of this were that in the aged plume, DFe concentrations might be depleted at a lesser rate than DMn. Owing to the very changeable deep ocean currents in this study area, the NBP that we sampled was an effluent cloud that dispersed in all directions and may be several hours or even days old. Because Mn does not tend to form colloidal phases in hydrothermal plumes (Sands et al., 2012; collidal = 0.1 - 0.4 μm) and is not complexed by organic ligands, it will be oxidised and not remain in the effluent for as long as stabilised DFe (Fitzsimmons et al., 2013). The main consequence of this result is that the stated orders of dilution in Figures 4.3 and 4.7, which are determined from Mn concentrations, should be considered as a maximum estimates, particularly in more diluted samples.

Colloidal (or smaller) material is not expected to settle in seawater (according to Stokes' settling laws; Yücel et al., 2011), and is therefore likely to be transported over large distances away from hydrothermal plumes by deep ocean currents. The likelihood of further aggregation of colloidal and FeL type complexes is low (Honeyman and Santschi, 1989) due to the extremely low concentrations involved (<100 nM) as the plume disperses and particle/colloid concentrations decrease (Field and Sherrell, 2000). This stabilisation of DFe in the NBP is clearly important to the transport of Fe and the significance of hydrothermal plumes as a source of Fe to

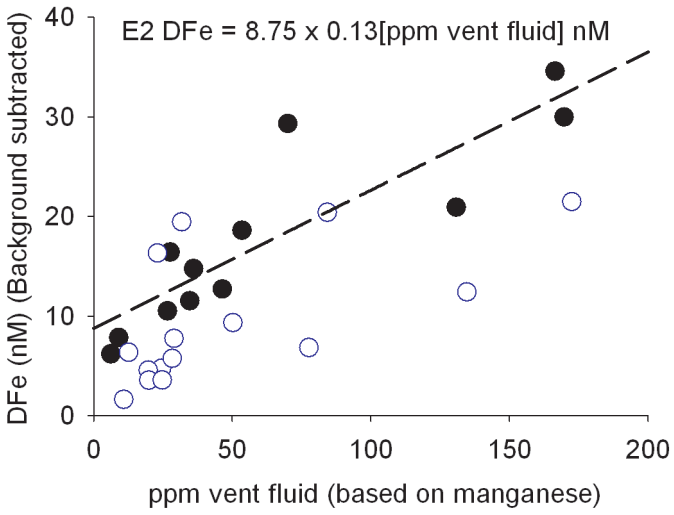

Figure 4.8: Dissolved Fe plotted against vent fluid concentration in seawater (ppm) in the neutrally buoyant plumes for E2 (filled black circles) and E9N (unfilled blue circles). The dilution is based on dissolved manganese, which is often used as a conservative tracer. The dashed line shows a regression for the E2 samples, which tend to 8.75 nM Fe above background rather than zero as predicted. The E9N samples showed a much higher degree of variation, which was also found in the RT-CLE-ACSV experiments, possibly indicating more complicated and diverse Fe speciation.

the deep ocean. It is likely that hydrothermal vents indeed produce the lenses of enhanced DFe concentrations that have been observed in the deep ocean (Klunder et al., 2011; Kondo et al., 2012; Nishioka et al., 2013; Wu et al., 2011), and may also supply large quantities of colloidal Fe to the deep ocean (Bergquist et al., 2007; Wu et al., 2001). Interestingly, our results differ from those of Nishioka et al. (2013) in that we see a large contribution of CFe to the DFe pool, whereas they found a large influx of SFe from hydrothermal sources. The different observations may be due to small differences in Fe(II) oxidation rates or vent fluid sulfide concentrations, which control partitioning between soluble Fe(II) and colloidal Fe(III) in early stages of plume development (Field and Sherrell, 2000). In our study area, the likely destination of stabilised vent Fe is towards the east on the Antarctic continental shelf after movement along the circumpolar current and upwelling to the surface ocean (Marshall and Speer, 2012). A volcanic eruption from the South Sandwich island arc has previously resulted in pumice being transported around the entire Southern Ocean (Coombs and Landis, 1966; Risso et al., 2002; Sutherland, 1965).

Our estimation that 7.5% of hydrothermal Fe is stabilised by Fe binding phases is slightly higher than the 4% reported by Bennett et al. (2008). These workers suggested that hydrothermal vents could provide 11-22% of deep ocean Fe. Since then, attempts have been made to incorporate the hydrothermal contribution of DFe to global oceans into numerical models (Sander and Koschinsky, 2011; Tagliabue et al., 2010). It is important to note that to date we have little understanding of what constrains the portion of hydrothermal Fe that is stabilised for transport from an individual vent site. Hydrothermal fluids vary in Fe composition over more than 5 orders of magnitude (see Figure 2.4), and other seawater constituents that may affect Fe speciation (e.g. $[H^+]$, $[HS^-]$, [DOC]) are also highly variable (and independent of Fe) in hydrothermal environments. Future studies should aim to scrutinise the speciation of Fe in a range of environments, with a key example being the Rainbow site, Mid Atlantic Ridge, where fluid Fe = 24 mM (Douville et al., 2002; c.f. this study Fe = 0.8 - 1.3 mM).

4.5 Conclusions

We have shown that two fairly typical hydrothermal plumes contained high concentrations of labile Fe that was bound by ligand phases averaging 30% of the DFe concentration or 7.5% of the total hydrothermal Fe (see Chapter 7). The two vent sites were not statistically different in terms of $K'_{Fe^{3+}L}$ or the ratio of L:DFe, possibly suggesting that certain features of Fe stabilisation in hydrothermal plumes are universal to typical hydrothermal systems. The complexes (along with observed colloidal phases) are likely to remain dissolved and be available for transport into the deep ocean.

Our results suggest that the Fe binding observed was the result of the flocculation of hydrothermal Fe with ambient dissolved organic matter upon entry into the cold deep ocean. In principle, this process may occur in other systems where Fe rich water meets organic rich seawater (such as rivers). It is possible that the resulting complexes are too weak to be detected by traditional CLE-ACSV methods, and that the complexes are lower in concentration than total DFe, preventing detection by the forward titration technique. Such phases may make up some of the previously observed weak ligands, and would be present in all seawater with riverine or hydrothermal inputs. These processes may therefore have an enormous global impact on Fe concentrations and biogeochemistry.

The two study sites were relatively similar in a global context, and ideally sites with high/low Fe, sulfide, acidity, temperature and level of sedimentation should be examined under the same experimental conditions to test our hypothesis that 7.5% of all hydrothermal Fe is stabilised. Given that the concentration of Fe in hydrothermal fluids does not seem to depend solely on geological features (spreading rate, temperature) or chemical features ($[HS^-]$, $[H^+]$), further measurements of Fe speciation in various vent sites in a variety of geographical locations are required before numerical models of hydrothermal Fe contribution to the oceans can be constrained.

Chapter 5

Iron speciation in the Kemp Caldera

Contents

5.1 Introduction

Submarine island arc seamounts and calderas occur along all oceanic subduction margins and many (∼29 - 54%) are hydrothermally active (Baker et al., 2008; de Ronde et al., 2001; Resing et al., 2009) accounting for ∼9% of global hydrothermal water flux (Baker et al., 2008). Differences in the chemical composition of island arc hosted hydrothermal venting may therefore be important when considering the global impacts of hydrothermal activity. For example, it was recently shown that the NW-Rota-1 volcano on the Mariana Arc (Western Pacific Ocean) vented hydrothermal fluids that contained 1000 times more aluminium than mid ocean ridge (MOR) hydrothermal fluids (Butterfield et al., 2011). The understanding of such differences may serve to better constrain the oceanic cycles of several elements (Frank et al., 2006). Unlike MOR or back-arc basin (BAB) spreading centre vent sites, island arc hydrothermal vents often occur at depths less than 1000 m (de Ronde et al., 2001; De Ronde et al., 2007; Embley et al., 2007). Hydrothermal island arcs are capable of large power and chemical mass fluxes, and material can escape from within calderas (Staudigel et al., 2004), and the buoyant hydrothermal effluent may therefore have an important effect on productivity in the surface mixed layer of the oceans, especially those depleted in the micronutrient iron (Fe; Boyd and Ellwood, 2010).

Island arcs can host hydrothermal activity in both volcano cones and collapsed calderas (Baker et al., 2008). The caldera walls can be sufficiently high to trap vented hydrothermal effluent, although this process has rarely been reported (Baker et al., 2012; Leybourne et al., 2012; Massoth et al., 2007). While the trapping may have an important localised effect on the chemistry of the seawater, it also serves to provide a natural laboratory to test hypotheses about the chemical fate of elements such as Fe, some of which may be kinetically stable in the dissolved phase in hydrothermal plumes (Bennett et al., 2008; Hawkes et al., 2013a; Statham et al., 2005; Toner et al., 2009; Wang et al., 2012; Yücel et al., 2011).

In hydrothermal settings where Fe concentrations exceed hydrogen sulfide, the grad-

ual formation of oxidised Fe oxy-hydroxide particles dominates the Fe speciation in the plume (Edmonds and German, 2004; Feely et al., 1996; Field and Sherrell, 2000; Sands et al., 2012). However, in island arc calderas and some MOR settings, sulfide may be in similar or greater concentrations than Fe, and FeS_x species must be considered alongside Fe oxy-hydroxides when considering the development of the dispersive plume (Yücel et al., 2011). Fe can form covalent or coordination bonds with S, and is often found as $FeS_{(aq)}$, FeS_2 (pyrite) and $Fe(HS)^+$ in natural marine environments (Luther and Ferdelman, 1993; Rickard and Luther, 1997). FeS_2 has been observed in high temperature vent fluids prior to emission into seawater (Yücel et al., 2011) and this Fe-S bond is not kinetically labile, as the Fe electrons are in a d^6 low-spin configuration (Luther and Rickard, 2005; Luther and Tsamakis, 1989). Yücel et al. (2011) therefore suggested that a significant portion ($\sim$10%) of hydrothermal Fe may be transported in hydrothermal plumes as stable Fe(II). Iron(II) can also be stabilised in particle aggregations by organic matter (Toner et al., 2009), and anoxic hydrothermal sediments may host the gradual formation of amorphous and framboidal pyrite through reaction of FeS with excess sulfide (Butler and Rickard, 2000; Rickard and Luther, 1997). Hydrothermal sulfide species may gradually oxidise in seawater and oxic sediments (Zeng et al., 2008), leading to further production of oxy-hydroxide phases and co-precipitation of several other elements (Chapter 6).

The balance between sulfur-bound and oxidised Fe in hydrothermal plumes will play an important role in the eventual fate of Fe in terms of geochemistry and bioavailability: the latter because one of the main bacterial approaches to Fe acquisition is through enzymatic reductive uptake - a process that is common for $Fe(OH)_x$ (Shaked and Lis, 2012) but not for FeS_x. Iron oxides are observed to co-precipitate with other elements in seawater (phosphorus (P), vanadium (V), arsenic (As), uranium (U), rare earth elements (REEs)), and this leads to significant modifications of ocean budgets of these elements (Feely et al., 1998; German et al., 1991). This chapter details investigations to interpret the balance between Fe(II) and Fe(III) in the Kemp Caldera water column and close to the 'Winter Palace' and 'Great Wall' vent

sites using voltammetric techniques and concentration analyses of several elements in various size fractions. In doing so we investigate whether the observed features of the Fe cycle in the caldera can be attributed to the known hydrothermal venting, and we discuss the relevance of island arc hydrothermal venting in the global Fe biogeochemical cycle.

5.2 Methods

5.2.1 Study area, Seawater profiling and sampling in the Kemp Caldera

The Kemp Caldera is described in Chapter 2. The caldera walls are high enough to trap the hydrothermal effluent, and therefore the system provides an excellent opportunity to examine the chemical fate of hydrothermal Fe, which is normally dispersed far from vent systems along deep ocean currents (Bennett et al., 2008; German et al., 2010).

A Seabird +911 conductivity, temperature and depth (CTD) profiler equipped with a light scattering sensor (LSS), reductive potential (Eh) detector and oxygen sensor was used to conduct water column profiles of the Kemp Caldera over three research cruises from 2009-2011 (note that in 2009 the Eh detector was not available). In 2010 and 2011 the profiler was used to collect seawater samples in 10 L Ocean Test Equipment (OTE) bottles guided by the real-time sensor readings. The remotely operated vehicle (ROV) *Isis* was used in 2010 to collect samples of the end-member fluids and sulfur chimneys (as described in Connelly and others, in prep.) and early buoyant plumes (using 1.2 L OTE bottles; referred to herein as 'near vent' samples). Samples were taken at several depths in the caldera, mainly above the Great Wall site (59.695°S, 28.352°W), but also 2 km away at a site within the caldera which did not show any local hydrothermal activity at 59.7°S, 28.317°W. Seawater was also sampled from inside a different caldera with very little hydrothermal activity as a relative background sample for dissolved metals and labile Fe (see below).

5.2.2 Particulate, dissolved, soluble, colloidal and labile element measurements

Dissolved and soluble Fe and Mn from CTD samples were separated and analysed as described in Chapter 4. The near vent samples taken by the ROV *Isis* had very high concentrations of Fe and Mn and were directly analysed by ICP-MS (X-series, Thermo Fisher Scientific) after dilution (100x) in 3% HNO_3 containing an internal standard of Be and In (20 ppb and 10 ppb, respectively). Labile Fe was determined by complexation with 40 μM 1-nitroso-2-naphthol (NN), as described in Chapter 3. The labile Fe (herein Fe_{NN}) was quantified by comparison with standard additions of Fe in low Fe seawater and hydrothermal plume seawater, and the ionic matrix difference did not have a significant effect on electrode sensitivity. Methods for particulate phase digests and spectroscopic analysis are described in detail in Chapter 6.

The method of Luther and Tsamakis (1989) was used to determine non-purgeable dissolved (NPD) sulfide in filtered samples that had been frozen and defrosted to room temperature. The voltammetric method was adapted as in Al-Farawati and van den Berg (1999) for use with the voltammetric setup described in Chapter 3 (i.e. with an Ag/AgCl counter electrode in place of the SCE electrode used by Luther and Tsamakis). We used a deposition potential of -0.2 V and scanned from -0.2 to -0.9 V using a square-wave modulation with pulse height 25 mV, frequency 150 Hz, scan increment 2.5 mV. The deposition time was 120 s.

5.3 Results

5.3.1 Water column profiling and anomalies

The water column temperature and light attenuation profiles varied between 2009 and 2011 (Figure 5.1). The sub surface temperature (at 100 m) was up to 1°C cooler in 2010-2011. In 2010 and 2011 a large positive anomaly (∼0.1°C) occurred between 600-800 m in comparison to 2009. Deeper in the caldera (>1100 m), temperatures increased by ∼0.01°C yr^{-1}. During the two sampling cruises (2010-2011), light

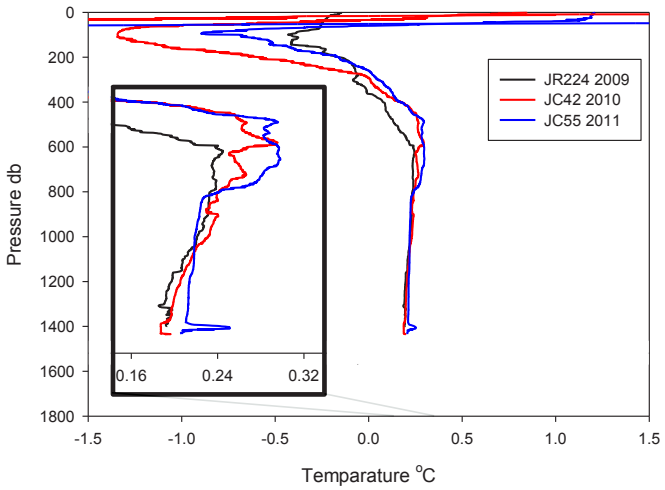

Figure 5.1: Water column temperature from surface to the depth of the Great Wall feature over the course of three years. The deeper parts of the caldera (>1000 m) may be gradually warming and overturning the caldera water. Sub-surface effects (∼100 m) are probably due to variations in sea ice and are not a hydrothermal effect.

attenuation anomalies were present at three depths in the caldera, at ∼0 m, ∼120 m and ∼500 m above the vent orifices. The two deeper particle plumes (as measured by LSS) were accompanied by temperature, Eh and Mn anomalies, and were the result of hydrothermal venting in the caldera (Figure 5.2). The upper particle plume coincided with increased Mn concentrations but not Eh, temperature or total Fe anomalies. This feature was not present in 2009 (Figure 5.3). The bottom water oxygen concentration was ∼210 μmol kg^{-1}, compared with ∼320 μmol kg^{-1} in surface waters.

5.3.2 Mn and Fe size fractions and speciation

Total (dissolved plus particulate) Mn and Fe concentrations were highly enriched (∼100 x typical Southern Ocean concentrations of 0.1-1 nM; Bucciarelli et al., 2001) in all parts of the caldera (Figure 5.2A) after trapping of the hydrothermal effluent. The majority of Mn was in the dissolved phase (97.0 ± 3.3%, mean ± 1 SD) due to its long oxidative half-life in seawater (up to 2 years; Lavelle et al., 1992). Total Fe (15 - 30 nM) concentrations were less variable than total Mn (40 - 120 nM)

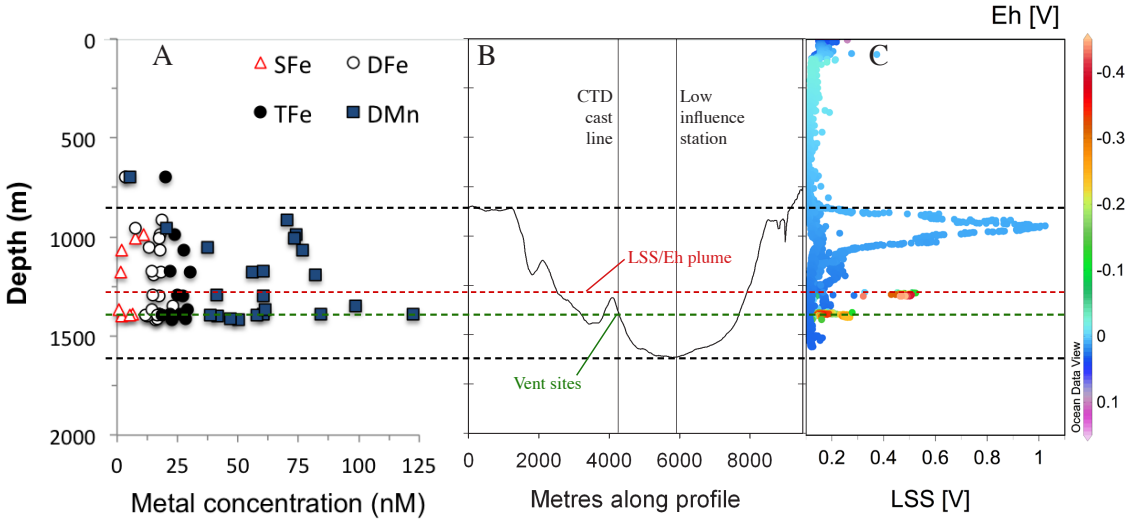

Figure 5.2: Depth profiles of several features in the caldera. A: Mn and Fe (total, dissolved and soluble) concentrations with depth. B: Bathymetry of the Caldera with the resurgent cone shown at ∼4 km along the profile. The hydrothermal vent sites are marked, as is the depth of the LSS/Eh plume (as a horizontal line). The positions of the typical cast location on and off the hydrothermal site are indicated by vertical lines. Note that the bathymetry is ∼6x vertically exaggerated. C: Light Scattering Sensor (LSS) reading with Eh detector anomaly indicated by colour. The Eh readings have been normalised to the reading at 500 m to correct for detector drift over the course of the CTD casts.

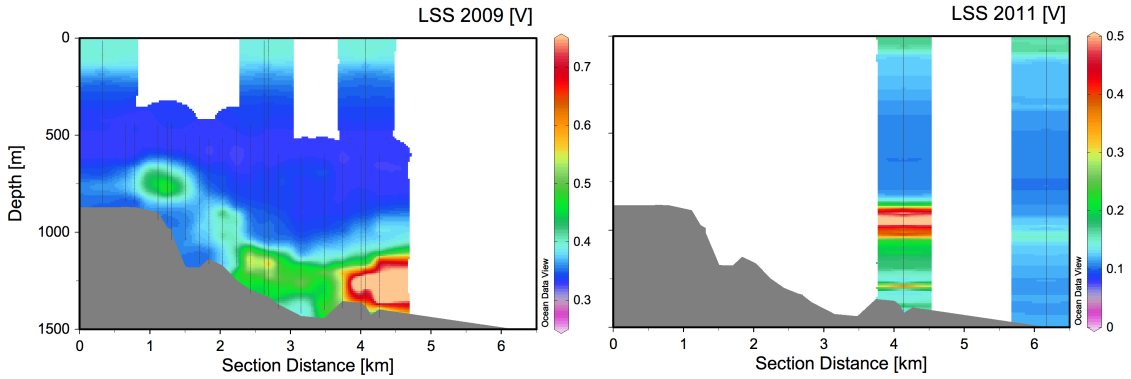

Figure 5.3: Section of light scattering sensor (LSS) readings in 2009 and 2011 plotted from the sill into the caldera over the resurgent cone to where the Winter Palace and Great Wall vent site is located. The absolute value in volts of LSS changes over time but the scale of an anomaly is consistent based on surface anomalies. The LSS ranges are the same for both plots. In 2009 a large LSS signal was seen ~100 m above the known vent sites. In 2011 this signal was much narrower and weaker, and was lower in magnitude than the anomaly centred around 950 m (also shown in Figure 5.2C).

above the Great Wall site, and dissolved Fe (DFe, <0.2 μm) was generally present at concentrations of 13 - 19 nM. The majority (6.6 - 16.1 nM) of dissolved Fe was in the colloidal (0.02 - 0.2 μm) size fraction (71.8 $\pm$ 21.3%, mean $\pm$ 1 SD) rather than the soluble size fraction (<0.02 μm; 0.7 - 11 nM; Figure 5.2A, Figure 5.4). The proportion of soluble Fe was higher in samples with greater influence from the known hydrothermal vent field and in the shallower particle plume (Figure 5.2A). Colloidal Fe made up 45 $\pm$ 11% (mean $\pm$ 1 SD) of total Fe. Particulate Fe concentrations did not vary much throughout the caldera or in the measured LSS plumes (Figures 5.2, 5.4), possibly suggesting that the partitioning between colloidal and particulate phases had reached a pseudo-steady state and that the hydrothermal vent plumes sampled were not the principle source of Fe. A highly variable portion (9.7 - 82.2% away from the immediate influence of the vent sites) of DFe was 'labile' Fe_{NN}. The concentration of Fe_{NN} was not necessarily enhanced in the near vent samples, whereas DFe typically showed highly elevated levels (Figures 5.4, 5.5). Of particular note is the large increase in Fe:Mn in these samples (Figure 5.5), suggesting that the samples incorporated more Fe-rich phases such as sediments. In the near vent

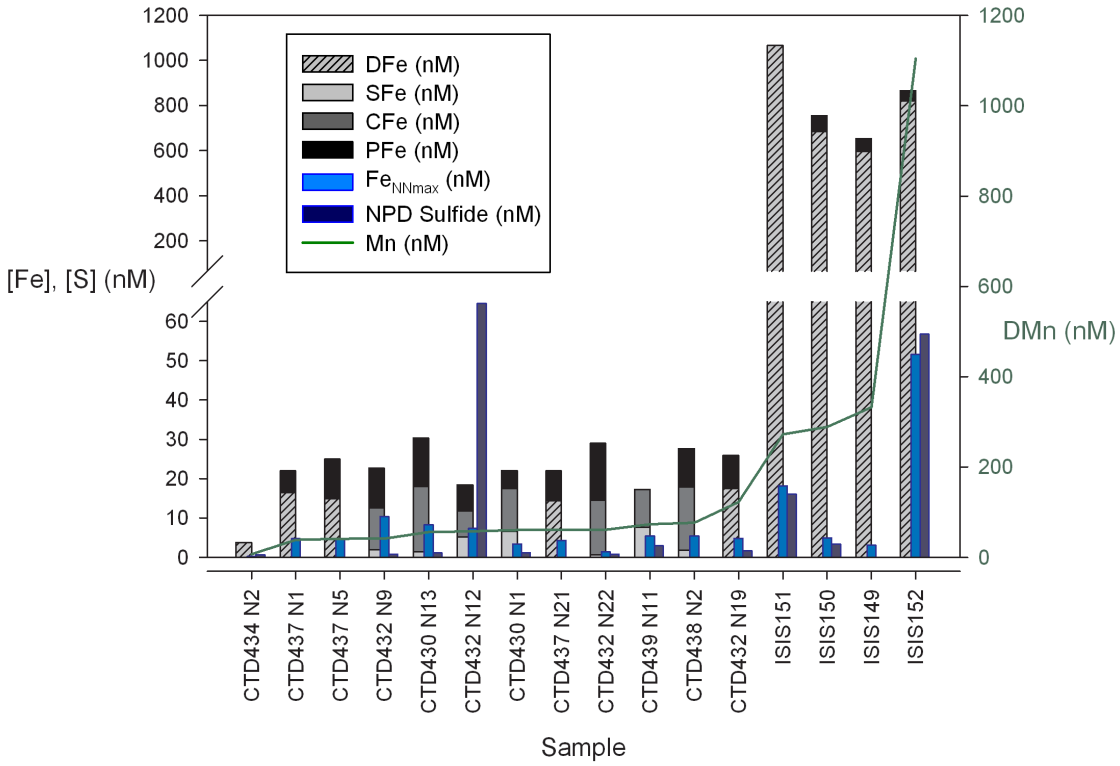

Figure 5.4: Fe size fractions, NBP sulfide and dissolved Mn for several CTD and near vent samples in the Kemp Caldera. A large change in concentrations was observed between the near vent and general caldera sets - largely due to loss of DFe; Fe_{NN} was less variable. Increased NBP sulfide was only found for three samples, and two of these corresponded well with increases in Fe_{NN}. The other (CTD432 N12) may be due to other metal sulfides or elemental sulfur. A sample outside the caldera along the island arc (CTD434 N2) is shown for comparison.

samples, the proportion of Fe_{NN} varied between 0.5 - 6.3% of DFe (four samples measured).

5.3.3 Non-purgeable dissolved sulfide

Increased NPD sulfide above typical seawater concentrations of ~2 nM (Luther and Tsamakis, 1989) was only detected in three samples taken very close to the vent sources (Figure 5.4). Quantification of the signal was challenging due to the rapid reaction of added (free) sulfide with dissolved iodide (i.e. when measuring standard additions; Luther and Tsamakis, 1989) and the reaction of sulfide on the surface of

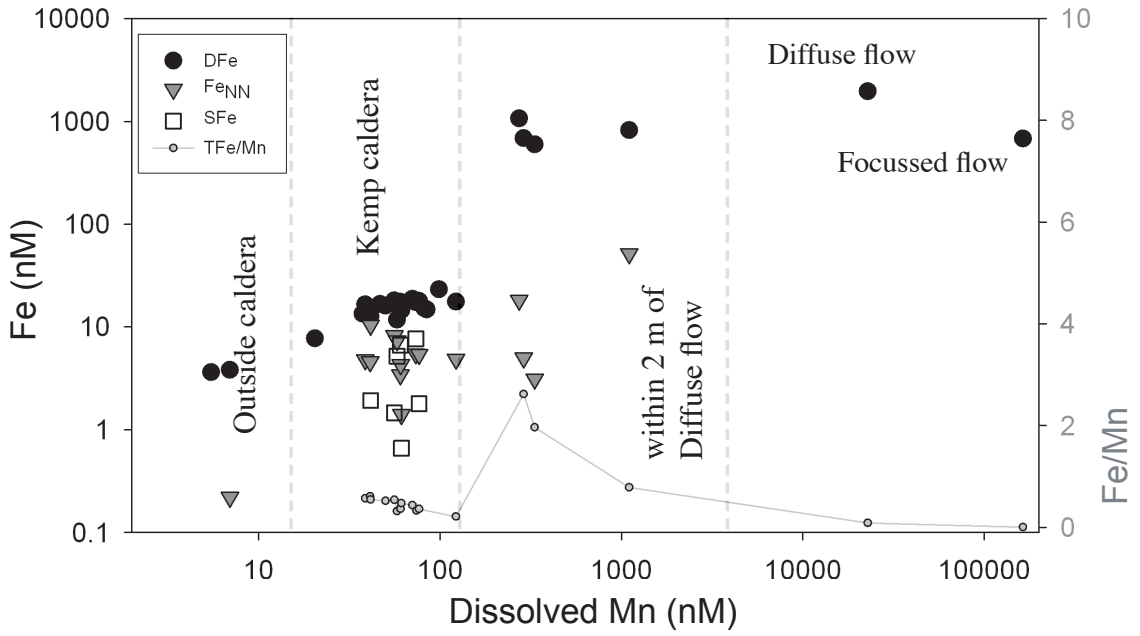

Figure 5.5: Various fractions of Fe plotted against dissolved Mn. The fluid and near vent samples taken by *Isis* are separated by vertical dashed lines, and two samples from a different part of the island arc are shown for comparison. The Fe/Mn ratio is shown as a grey line, showing the input of additional Fe in the near vent samples and higher in the water column.

discarded mercury drops and dissolved mercury in the cell (Al-Farawati and van den Berg, 1999; He et al., 2002). The NPD sulfide could therefore only be determined in a semi-quantitative manner, and is likely to be a lower estimate of the concentration. Using the concentration to current ratio presented in Al-Farawati and van den Berg (1999) (2 nA/nM for 120 s deposition), the estimated concentrations detected are plotted in Figure 5.4. Increases in NPD sulfide corresponded well with increases in Fe_{NN} in two near vent samples.

5.3.4 Particulate oxyanions

Elemental concentrations in the particulate phase (>0.2 μm) and elemental ratios with respect to Fe are reported and discussed in Chapter 6. In summary, P, V, As and Mn all correlated well with Fe in the particulate phase in the caldera samples, and the incorporation of the elements was lower in the near vent samples except for As, which was incorporated to a greater extent. From these observations I infer that the particles in the caldera were Fe oxy-hydroxides and not predominantly sulfides (Feely et al., 1998), whereas close to the vents a greater variety of particles existed.

5.3.5 Particle analysis by SEM, μXRF and μXAFS

Close to the vent sites, large abundances of Fe, Cu and Zn sulfides were identified by elemental ratios using SEM. Pyrite was identified (by Fe:S = 0.5) both in small particles and in large framboidal assemblages, which were usually about 10 μm in diameter (Figure 5.6). The elemental ratios of the (poly-) metallic sulfides were often slightly more sulfur rich than in the mineral stoichiometry, almost certainly due to the dispersal of very fine elemental sulfur over the entire filter membrane. This was confirmed by X-Ray Fluorescence (XRF) mapping, which showed high concentrations of sulfur in almost all parts of a 250 μm square analysed, while elements which are typically bound to sulfur in particles (Fe, Cu, Zn) were only present in distinct, larger fragments (see Figure 6.9, Chapter 6). Iron containing particles were identified as pyrite, chalcopyrite or other poly-metallic sulfides by comparison with spectra from Fe(II) and Fe(III) mineral standards using X-Ray

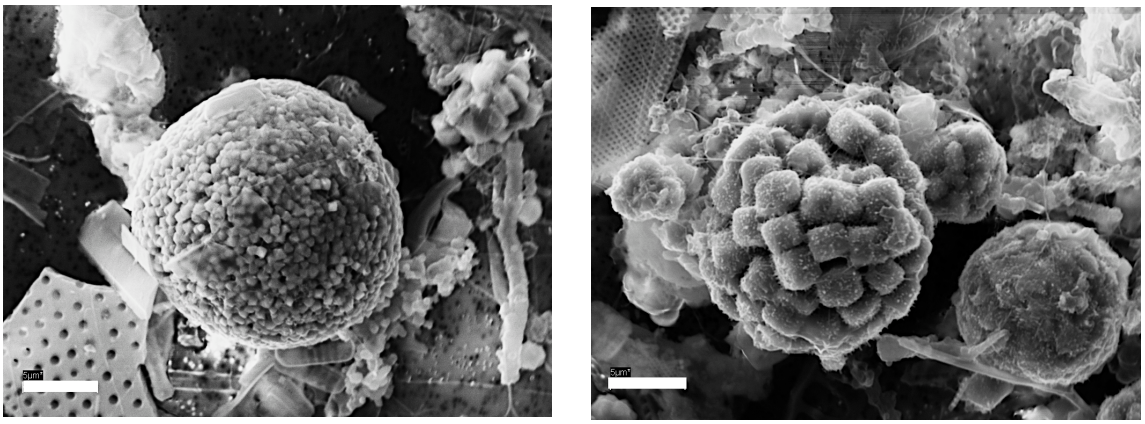

Figure 5.6: Framboidal pyrite on filters from ∼2 m above the Great Wall site imaged by SEM. Scale bar = 5 μm. These assemblages form at various temperatures when saturated solutions of $FeS_{(aq)}$ are reacted with H_2S (Butler and Rickard, 2000). Much of the other material present on the filter was siliceous biogenic material from the water column.

Adsorption Near Edge Spectroscopy (XANES). Barium (present in barite, $BaSO_4$) was detected in far fewer particles than the chalcophile elements, but were common on filters taken by stand alone pump system (SAPS) higher in the water column.

5.4 Discussion

Distinct differences were found between the near vent areas around the Winter Palace/ Great Wall vent field and in samples from higher above the site and elsewhere in the caldera, particularly in the Fe:Mn ratio. This suggests that the ambient material within the caldera was sourced from a different vent or that recent changes (before 2010) to the nature of venting resulted in an abrupt change in fluid chemistry. Here I discuss the results from the near vent samples and the rest of the caldera separately and then consider the caldera as a system in its entirety.

5.4.1 Near vent Fe chemistry

The Kemp Caldera vent fluids from Winter Palace/ Great Wall had low concentrations of Fe ($\leq$3.9 μM; Connelly and others, in prep.) and were unusually highly concentrated in hydrogen sulfide compared with typical vent fluids (measured at

>10,000x Fe; Figure 2.4, Chapter 2). Hydrogen sulfide is usually present in hydrothermal fluids at more similar concentration to Fe (within 1-2 orders of magnitude of each other, Figure 2.4), which allows an excess of free Fe^{2+} to rise in the buoyant plume and not be bound to sulfur (e.g. Field and Sherrell, 2000; Marbler et al., 2010; Mottl and McConachy, 1990). This is facilitated by competition for sulfide from more chalcophilic elements such as copper and zinc (Klevenz et al., 2011) and the oxidation of sulfide by dissolved oxygen (Gartman et al., 2011).

The excess sulfide at the Winter Palace/ Great Wall site resulted in the supersaturation of hydrothermal FeS by hydrogen sulfide: a process that leads to the formation of pyrite framboids (Figure 5.6; Butler and Rickard, 2000). The intriguing increase of Fe:Mn from the vent fluids (∼0.01) to the near vent samples (1-3; Figure 5.5) suggests that hydrothermal Fe was sequestered from the vent fluids subsurface as sulfides, which were then re-incorporated into the system after interaction between bottom water and hydrothermal sediments. Mn apparently remained in the high temperature fluid, probably due to its higher solubility compared with Fe as hydrothermal fluids cool sub-surface (Seyfried and Ding, 1993) and more conservative behaviour in the presence of dissolved sulfide (Mottl and McConachy, 1990). Much of the Fe in the near vent samples was in the dissolved phase (average 91%, see Appendix D; Figure 5.4), suggesting that nano-particulate sedimentary sulfide phases as well as pyrite particles and framboids were important (Yücel et al., 2011). The larger reduced Fe compounds are likely to settle quickly and not be transported into the shallower parts of the caldera (Feely et al., 1990; Trocine and Trefry, 1988), whereas 'colloidal' sized phases could be transported more easily (Homoky et al., 2011; Yücel et al., 2011). It is unclear to what extent the ROV operations led to the re-suspension of this material, and in any case the low temperature (and resulting lack of buoyancy) of the diffuse bottom water in question precludes the transport of this material far from the seafloor. The question of whether this material may be distributed around the caldera then becomes a question of time (and the longevity of this style of venting). Fe sulfide material may be gradually oxidised in oxic seawater (Zeng et al., 2008) but this process appears to be retarded in some hydrothermal

systems (Yücel et al., 2011).

The concentration of Fe_{NN} did not increase to the same extent as DFe close to the vent sites, suggesting that the sampled 'dissolved' nano-particulate pyrite phases are likely 'inert' to exchange with NN. However, increases in NBP sulfide corresponded well with increases in Fe_{NN} (Figure 5.4). The samples gave a peak at $\sim$ -0.75 V (Figure 5.7): more negative than usually observed (-0.6 V) for seawater sulfide (Ciglenečki and Ćosović, 1996; He et al., 2002; Laglera and Tovar-Sánchez, 2012; Luther and Tsamakis, 1989). Increased pH can result in a more negative peak potential (Ciglenečki and Ćosović, 1996), but these samples are more acidic than typical seawater (pH measured as 7.3 near the seafloor in a diffuse vent sample; D. Green, pers. comm.). No evidence for this unknown species was found elsewhere, suggesting that it was not dispersed throughout the caldera. The lack of large amounts of NPD sulfide in these samples suggests that Fe sulfide 'ligand' complexes (e.g. $Fe(SH)^+$) either oxidised rapidly or were not present in this environment. Oxidants (either O_2 or S^0) were present in the sediment and bottom water, as evidenced by the presence of pyrite framboids (Wilkin et al., 1996). The range of particles found in the near vent environments in the caldera is discussed in Chapter 6.

5.4.2 Caldera Fe chemistry

Manganese and iron were both highly enriched inside the caldera, and concentrations decreased outside (above the sill) of this feature (Figure 5.2A, Figure 5.5). Assuming that hydrothermal inputs were the most significant source of metals to the caldera, it follows that the species found in the caldera are similar to those which naturally disperse from island arc environments - albeit with a greater chance of long term intra-plume interactions. The total Fe:Mn ratio in the caldera was much higher than the sampled vent fluids from the Winter Palace/ Great Wall vent site (Figure 5.5), and Fe is normally preferentially lost from hydrothermal plumes due to the formation of sulfides and the faster oxidation (and precipitation) rate of Fe (Leybourne et al., 2012; Mottl and McConachy, 1990). This result, along with the fact that DFe did

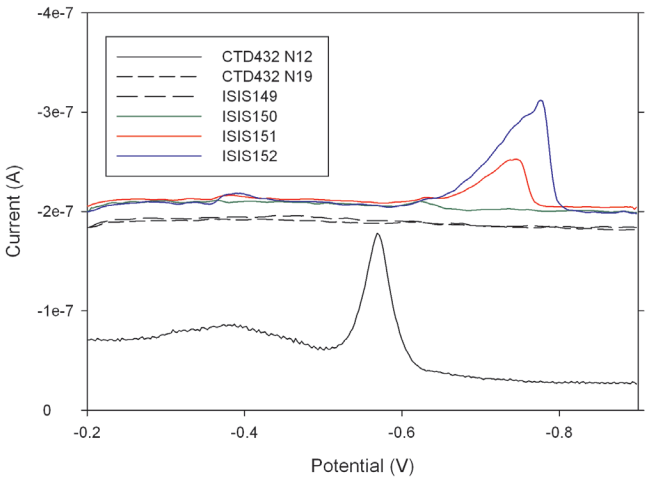

Figure 5.7: Several voltammograms of NPD sulfide deposited on a HMDE at -0.2 V for 120 s. Most filtered samples from the caldera did not give an easily measurable peak (e.g. CTD432 N19, dashed black line), but three samples gave peaks either at the typical potential found for sulfide (between -0.55 V and -0.6 V) or at a more negative potential (-0.75 V).

not increase in the hydrothermal plumes sampled above the Great Wall site (Figure 5.2), suggests that a different (high Fe:Mn) source of hydrothermal venting exists within the caldera. At the stations where the CTD profiles were conducted, the caldera water was therefore apparently well mixed hydrothermal effluent from an unknown source with additional inputs of dissolved Mn (Figure 5.2) and non-Fe bearing hydrothermal particles such as barite (Hitch, 2012) from the known Fe-poor vent sites.

Given the geological setting and the strong magmatic influence, it seems likely that the unknown vent source was an acid sulfite vent site (Butterfield et al., 2011; de Ronde et al., 2011; Gamo et al., 1997; Leybourne et al., 2012; Resing et al., 2007) with a high vent fluid Fe:Mn ratio (e.g. up to ∼18, de Ronde et al., 2001, 2005; Leybourne et al., 2012; Massoth et al., 2003). It is possible that this vent source exists elsewhere in the caldera, or that the vent fluid chemistry abruptly changed between 2009 and 2010 (see discussion below), and that the previous hydrothermal effluent remained in the water column. In either case, it seems reasonable to discuss the Fe chemistry of the caldera in terms of Fe rich acid sulfite venting and not in

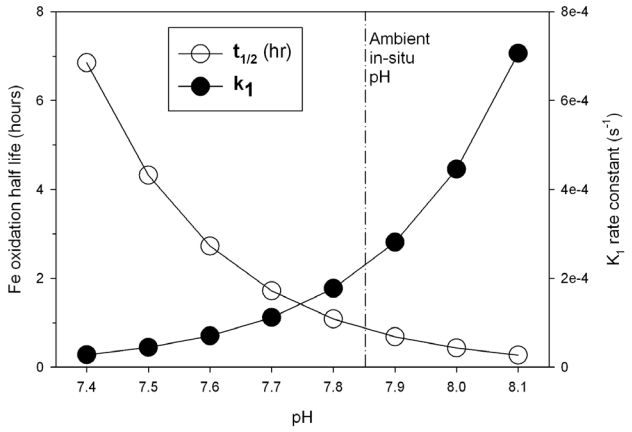

Figure 5.8: Change in oxidation half life ($t_{1/2}$; unfilled circles) and rate (k_1; filled circles) of Fe(II) with pH under the typical conditions of temperature, ionic strength and $[O_2]$ in the Kemp Caldera using Equation 1.1, Chapter 1. Island arc hydrothermal plumes can be 1 pH unit lower than ambient seawater, allowing a great increase in Fe(II) oxidation half life.

terms of the Fe poor, sulfide and Mn rich venting observed.

The particulate Fe correlated well with particulate oxyanions and manganese (Chapter 6), suggesting that Fe oxy-hydroxides and not sulfides dominated the particulate phase in the caldera. Considering that hydrogen sulfide is often not present in island arc caldera fumaroles (Butterfield et al., 2011) due to the fractionation of magmatic sulfite to sulfuric acid and elemental sulfur, it is possible that almost all hydrothermal Fe in these environments is left to oxidise as oxy-hydroxide colloids and particles (Field and Sherrell, 2000) or to form complexes with dissolved ligands (Bennett et al., 2008; Chapter 4). The oxidation of Fe(II) in such environments is likely to be slow (up to several hours; Figure 5.8) due to the mineral acidity associated with the dissolution of magmatic gases which persist in the plume (Resing et al., 2007), with pH often measured a whole pH unit below ambient in acid-sulfite vent plumes (Leybourne et al., 2012; Resing et al., 2007). The dispersal (and dilution) of plume effluent may therefore proceed as fast as Fe oxidation (both timescales in hours), limiting the amount of precipitation possible as Fe concentrations decrease and leading to a larger portion of colloidal sized particles (Field and Sherrell, 2000).

A variable but important portion (9.7 - 82.2%) of DFe was present as Fe_{NN}, i.e.

in kinetically labile complexes (able to bind with NN after overnight equilibration; Figure 5.4 and 5.5). This may include flocculated colloidal material that results from the oxidation and mixing of hydrothermal Fe with marine dissolved organic matter (Chapter 4), but not kinetically inert compounds such as pyrite or highly crystalline oxy-hydroxide phases. Amorphous oxy-hydroxides may be included in this fraction, and a varying degree of crystallinity or kinetic lability could explain the observed variability in concentration of Fe_{NN}.

5.4.3 Other vent site or change in venting?

Hydrothermal island arcs can host wide ranges of hydrothermal activity (Baker et al., 2008; Resing et al., 2009), often within the same caldera (Baker et al., 2012; de Ronde et al., 2011; Leybourne et al., 2012). It can take thorough surveying by underwater autonomous vehicle (AUV) to fully characterise the hydrothermal emissions from hydrothermal calderas (Baker et al., 2012), and so it is certainly possible that another vent site exists within the Kemp Caldera that has not been discovered.

Considering the difference we observed in the water column from 2009-2011 (particularly in light attenuation, Figure 5.3), it is also worth considering that hydrothermal effluent found in the caldera was left over from previous Fe-rich hydrothermal venting at the Winter Palace/ Great Wall site. In 2009 only the lower two of the three hydrothermal plumes were observed (Figure 5.3), and the intensity of the LSS anomaly suggested the presence of a high abundance of vent-derived particles. From 2010 the LSS anomaly was much smaller (0.025 V vs. 0.6 V) at neutrally buoyant plume depth (∼1300 m), consistent with a lower abundance of particulate oxy-hydroxide phases, Fe sulfides and native sulfur particles (Baker and Massoth, 1987; Baker et al., 2012). The obtained LSS increase in surface waters was comparable over the three cruises, confirming that variability in the sensor was not the cause of the differences. Given the volcanic setting of this hydrothermal activity, it is possible that in 2009 the venting was more similar to the high particulate, metallic acid-sulfate style venting often observed in magmatically influenced island

arc sites (de Ronde et al., 2011; Leybourne et al., 2012; Resing et al., 2007), and that since this time the fluid reaction pathway has increased, leading to a higher water/rock reaction ratio and higher dissolved sulfide and lower metal content in the fluids (de Ronde et al., 2005, 2011; Leybourne et al., 2012).

The large LSS plume at ∼900 m depth was first observed in 2010, possibly providing further evidence for a massive volcanic event or the emergence of an unusual Fe poor but particle rich hydrothermal vent site at a shallower depth around the caldera (Figure 5.2). The plume may also be due to sediment re-suspension from the sill of the caldera (Baker et al., 2005; Leybourne et al., 2012) and have little to do with hydrothermalism in the caldera. The regularity with which we observed this plume during 2010-2011 suggests that the material is small enough to avoid settling into the caldera, or that supply of material is continuous. Investigation of the size partitioning and elemental composition of this material may lead to important results about its origin, but the hydrothermal particle digest method (German et al., 1991) used in this work is not sufficiently strong to dissolve many (non hydrothermal) mineral phases (see Chapter 6). No increase in particulate Fe was measured in samples from this plume, so it is unlikely that this plume is composed of fresh hydrothermal particles.

It is not possible at this time to fully assess whether the increased Fe and Mn found in the caldera was sourced from a different vent site or the known site with different venting, and future visits to the site should aim to further explore the caldera and to assess changes in hydrothermal activity in the sedimentary record.

5.5 General Discussion

5.5.1 Fe speciation in island arc caldera and cone plumes

Colloidal sized species dominated the chemistry of Fe after dispersal into this hydrothermal caldera, and these phases probably included a mixture of pyrite nanoparticles (Yücel et al., 2011), oxy-hydroxide colloids (Field and Sherrell, 2000; Sands et al., 2012) and amorphous FeL aggregates (Hawkes et al., 2013a). Oxy-hydroxides

were probably most pervasive considering the high concentrations of oxyanions found in the particulate phase after further aggregation of this material. In island arc systems, where acidity and Fe concentrations are typically high (de Ronde et al., 2011; Leybourne et al., 2012; Resing et al., 2007), and hydrogen sulfide concentrations can be low (Butterfield et al., 2011), oxy-hydroxide colloids should dominate (Resing et al., 2007). Aggregation of nano-particles and colloids becomes less likely as the plume disperses, and in cases where the effluent is not trapped by caldera walls, 'soluble' sized Fe phases may also be important in the long term distribution of Fe (Nishioka et al., 2013).

5.5.2 Biogeochemical fate of Fe colloids

Iron associated with oxy-hydroxide and organic colloids can be utilised by photosynthesising organisms as a source of Fe (Chen et al., 2003; Chen and Wang, 2001; Dehner et al., 2011; Nodwell and Price, 2001; Sugie et al., 2013), possibly because they have mechanisms for reducing and dissolving Fe from colloidal species via extracellular processes, allowing incorporation of un-chelated, free Fe^{2+} (Hudson and Morel, 1990; Morel et al., 2008; Rich and Morel, 1990; Shaked et al., 2005; Shaked and Lis, 2012). The age, speciation and size of the colloids may lead to important controls on the bioavailability of the Fe (Chen et al., 2003; Chen and Wang, 2001; Dehner et al., 2011; Wang and Dei, 2003), and in fresh, amorphous hydrothermal colloids and nano-particles the Fe is more likely to be reactive and bioavailable than in highly crystalline phases (Anschutz and Penn, 2005; Sugie et al., 2013).

Shallow island arc vent plumes may therefore provide direct Fe nutrient supply to photosynthetic organisms. These supplies could include more labile, fresher material than the hydrothermal input reaching surface waters from deep ocean systems (Tagliabue et al., 2010), and may be more consistent and less periodic or climate dependent than other sources of Fe such as dust deposition or sea-ice (Tagliabue et al., 2010). The Kemp Caldera may be too deep to have direct influence on surface waters in the Southern Ocean (Figure 5.9), but other island arc hydrothermal plumes along the South Sandwich island arc and other island arcs can be shallower than

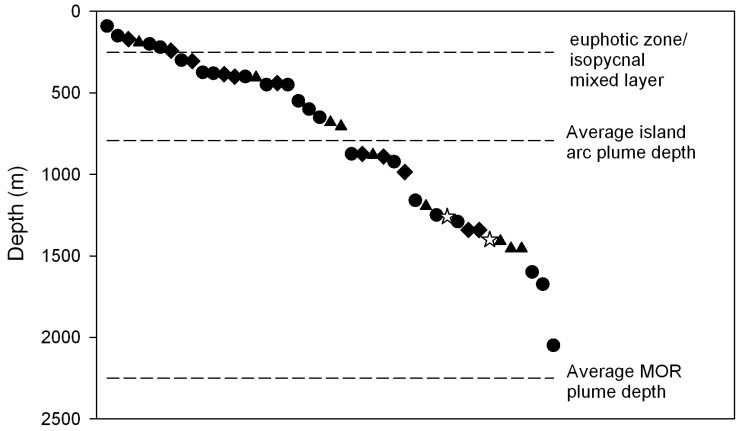

Figure 5.9: Depths of several reported island arc hydrothermal plumes in depth order. Black circles are from the Mariana Arc (Resing et al., 2009), black triangles from the Kermadec Arc (de Ronde et al., 2001), black diamonds from the Tonga arc (Massoth et al., 2007) and the Kemp Caldera hydrothermal plumes from this chapter are shown as unfilled stars. Representative depths of the euphotic zone/winter mixed layer (200 m) and average MOR plumes (2250 m) are shown along with the average depth of island arc plumes in this dataset (792 m) for comparison, showing that some island arc plumes may provide nutrients to surface waters during spring blooms. Wind driven eddies may also contribute to nutrient mixing (see text).

the typical winter convection cell mixed layer depth (∼200 m, de Boyer Montégut et al., 2004) and wind driven eddies may also increase vertical mixing (McGillicuddy et al., 2007). Ventilation of the Kemp Caldera (sill depth ∼850 m) from above could lead to some influence on the shallower water column during the winter, but this is unlikely to be investigated due to the regional coverage of sea ice during the Austral winter and spring. Displacement of caldera water laterally will lead to export of Fe colloids and Mn into the deeper ocean (700-900 m; Staudigel et al., 2004). Decoupling hydrothermal inputs from sub-aerial volcanic and dust depositional inputs along island arcs will be a challenge in assessing the importance of Fe fertilisation effects, and island arc surveys (Baker et al., 2008; de Ronde et al., 2001; Resing et al., 2009) in the future should aim to address the influence of hydrothermal plumes on marine productivity.

5.6 Conclusions

Hydrothermal effluent from an island arc caldera was trapped by the caldera walls, leading to an accumulation of the products of the hydrothermal fluid mixing with seawater. An important constituent of this material was Fe colloids, which were inferred to be oxy-hydroxide (nano) particles due to the co-precipitation of Fe with oxyanions and the scavenging of dissolved Mn in the particulate phase.

Two hydrothermal systems were inferred to be present in the caldera. One was limited to near-seafloor cycling of reduced Fe-sulfide products including pyrite framboids, which were the result of the large excess of hydrogen sulfide over Fe in the vent fluids at the Winter Palace and Great Wall vent sites. This system also injected high concentrations of dissolved Mn into the caldera. The second system led to the abundance of Fe colloids found in the caldera, and was the result of more traditional or acid sulfite style venting elsewhere or previously in the caldera. This system led to scavenging of several elements from seawater onto hydrothermal colloids and particles, and may lead to increased primary production in the southern ocean, depending on the spatial distribution of the caldera water after ventilation into the Scotia Sea.

Chapter 6

Particulate phase geochemistry from the E2, E9N and Kemp Caldera vent field plumes

Contents

6.1 Introduction

The extreme gradients in temperature, pH and oxidative potential between fresh hydrothermal fluids and the surrounding seawater lead to a rapid precipitation of several particulate (mineral) phases. These include anhydrite ($CaSO_4$), barite ($BaSO_4$) and mono- or poly- metallic sulfides (Klevenz et al., 2011; Mottl and McConachy, 1990), resulting in large deposits of poly-metallic sulfides around vent sites (Fouquet, 1997; German et al., 1999). Iron (Fe) and manganese (Mn) are the only metals easily detected above background concentrations in the dissolved phase in hydrothermal plumes, and these elements gradually oxidise and form oxy-hydroxide particles (Feely et al., 1996; Field and Sherrell, 2000; Klinkhammer et al., 1986). Further dissolved/particulate phase interactions occur as the plume develops, and these include scavenging and dissolution processes (Breier et al., 2012; Field and Sherrell, 2000), leading to a complex mixture of hydrothermal products and a modification of several elemental concentrations in the local deep ocean water (German et al., 1991; Trocine and Trefry, 1988).

Iron oxy-hydroxide phases can scavenge oxy-anionic elements, rare earth elements (REEs) and dissolved organic carbon (DOC) from vent fluid water, entrained seawater and after deposition in sediments (Bennett et al., 2011; Breier et al., 2012; Edmonds and German, 2004; Feely et al., 1990; German et al., 1991, 1990; Koschinsky and Hein, 2003; Olivarez and Owen, 1989; Sherrell et al., 1999). The co-precipitation and scavenging of elements by hydrothermal oxy-hydroxides have been investigated in hydrothermal plumes over a number of particle size ranges (>0.1 μm; Sands et al., 2012, >0.4 μm; Feely et al., 1991; Sands et al., 2012, >1 μm; Breier et al., 2012; Edmonds and German, 2004) and in hydrothermal sediments (German et al., 2002, 1999; Koschinsky and Hein, 2003; Olivarez and Owen, 1989). The species scavenged by Fe oxy-hydroxides tend to be neutrally or negatively charged in seawater (Koschinsky and Hein, 2003) and include aqueous forms of phosphorus (P), vanadium (V), arsenic (As), cobalt (Co), chromium (Cr), copper (Cu), lead (Pb), uranium (U), dissolved organic carbon (DOC) and the rare-earth elements (REEs) (Breier et al., 2012; Edmonds and German, 2004; Roth and Dymond, 1989; Trocine

and Trefry, 1988), which settle, leading to a removal of the scavenged elements and a control on the composition of ocean water (German et al., 2002, 1991; Koschinsky and Hein, 2003; Trocine and Trefry, 1988; Wheat et al., 1996). Feely et al. (1996, 1994a, 1998, 1991) demonstrated that the P:Fe ratio in hydrothermal plume particles was related to ambient phosphate concentrations and may therefore serve as a proxy for historical oceanic phosphate concentration in the sediment record.

In this chapter, the particulate concentrations of several elements (Al, P, V, Mn, Fe, Co, Cu, Zn, As, Ba) are discussed. The samples were collected during various stages of hydrothermal venting and the collection provided particulate distributions at the E2 and E9N vent sites of the East Scotia Ridge and in various parts of the Kemp Caldera. Additionally, specific mineralogy is considered in plume particles using scanning electron microscopy (SEM) imaging and X-ray adsorption fluorescence spectroscopy (XAFS).

6.2 Methods

Plume detection and sampling were conducted as described in Chapter 4. Stand Alone Pump Systems (SAPS) were also used, generally filtering $>$ 100 L seawater in-situ, and the filters (1 μm pore size, Whatman, 293 mm) were stored frozen alongside the 0.2 μm pore size filter membranes (45 mm) from the Ocean Test Equipment (OTE) bottles. Quarter of each SAPS filter was digested for analysis, while half filters were digested for the 0.2 μm filter membranes.

6.2.1 Dissolved phosphate analysis

Samples were collected directly from the OTE bottles through a length of PTFE tubing into a glass bottle (250 ml) avoiding inclusion of air bubbles. 2.5 ml of sample was removed and 50 μl of mercuric chloride was added to poison the sample. The glass bottles were sealed with air-tight plastic (Parafilm M, Alcan Packaging), stored at room temperature and analysed using a QuAAtro nutrient analyser (Seal Analytical) on shore.

6.2.2 Particle digestion

In order to fully digest marine particles and sediments, samples are typically heated in mixtures of HNO_3, $HClO_4$ and HF (German et al., 2002; Marsh et al., 2007; Trocine and Trefry, 1988). This ensures complete digestion of recalcitrant materials such as aluminosilicates. In the study of hydrothermal plume particles however, some of these background materials are not of interest, and researchers have deliberately used less extreme digestion methods (e.g. conc. HNO_3 reflux; German et al., 1991) in order to dissolve only the fresh hydrothermal precipitates. Other methods of particle analysis include the use of microwave reactors to digest material in acid (Breier et al., 2012) or direct analysis of filter papers by X-Ray emission spectrometry (Feely et al., 1991) or X-Ray absorption fluorescence spectroscopy (Breier et al., 2012; Toner et al., 2009). For this study, three acid digestion techniques were compared using blank filters and sediment standards as described below.

6.2.2.1 Digest procedures

Hotplate reflux method (after German et al., 1991): Each sample was placed in a screw-capped PTFE bomb (30 ml) with concentrated sub-boiled HNO_3 (20 ml). The acid was brought to reflux on a PTFE coated hot plate set at 150℃ for three days. The vessels were then left to cool and the acid was gradually transferred to a 15 ml PTFE bomb to dry down with the hotplate set at 100℃. In the cases when the filter was not completely digested, an extra 10 ml concentrated sub-boiled HNO_3 was added to the remaining filter material and these were left to digest for one day, at 100℃. This additional acid was also transferred to the vessel with the evaporated sample material. Once dry (assessed by inspection), 1 ml of 3% sub-boiled HNO_3 in deionised water (MilliQ, Millipore) was added to the sample, which nearly always contained a yellow precipitate that was assumed to be an oxidised product of the reaction of the filter matrix with nitric acid. The solutions were diluted with a further 3% sub-boiled HNO_3 for analysis by ICP-MS (X-series, Thermo Scientific). All 3% sub-boiled HNO_3 used was spiked with Be, In and Re (20, 10, 10 ppb) for use as internal standards. All work was carried out in a class 100 clean room in a

combined laminar flowhood/fume cupboard.

Microwave methods (after Breier et al., 2012): digestion of samples was carried out in a microwave (Anton Paar Multiwave 3000) using PTFE lined microwave vessels. 10 ml of acid was added to each vessel (1: 50% sub-boiled HNO_3, 2: 100% sub-boiled HNO_3). The temperature was ramped to 175℃ (1400 W) over the course of 20 min, and this was sustained for 40 min. The vessels were then allowed to cool (for 25 min) to room temperature. The solutions were diluted directly for analysis by ICP-MS using deionised water (MilliQ, Millipore) to make solutions of 5% HNO_3 (i.e. 10x dilution for method 1, 20x for method 2). The internal standard elements (Be, In, Re as before) were then added to the analysis solutions to make concentrations of 20, 10 and 10 ppb, respectively. All work was carried out in a class 100 clean room in a combined laminar flowhood/fume cupboard.

6.2.2.2 Blanks and Standards

Unused filters (0.2 μm polycarbonate, Whatman) were soaked in 10% HNO_3 (analytical grade, Fisher Scientific) for 1 week and then soaked in deionised water (MilliQ, Millipore) for 1 week, as this is the cleaning method used when collecting marine samples. These blank filters were cut in half using ceramic scissors (pre-washed in deionised water) and transferred to the digestion vessels with acid cleaned PTFE tweezers. Certified reference material (HISS-1 marine sediment, NRC Canada) was weighed into clean, dry glass vials and transferred into other digestion vessels for simultaneous treatment.

Ten elements (Al, P, V, Mn, Fe, Co, Cu, Zn, As, Ba) were analysed due to their importance in understanding hydrothermal plume and deep ocean background particles (German et al., 1991). The mean (x) and standard deviation (SD) of the blank (acid washed) filter are presented in Table 6.1, normalised to the concentration in a 1 ml solution. This normalisation is to account for the varying dilutions used for analysis. The limit of detection (LoD) is shown as three times the standard deviation, and this is also stated in terms of the LoD value (in picomoles per litre) in a seawater sample where 10 litres of water is filtered (the most commonly filtered

Table 6.1: Filter digest blank concentrations. LoD = Limit of Detection for 10 litres filtered seawater. Typical dilution from digest solution = 20x.

Method		Al	P	V	Mn	Fe	Co	Cu	Zn	As	Ba
Hotplate	x (ppb)	23.7	20.7	0.08	0.00	13.5	0.00	0.49	52.7	0.58	0.00
reflux	SD	15.7	15.2	0.10	0.12	7.32	0.01	0.49	14.8	0.33	0.80
100% HNO_3	LoD (pM)	347	294	1.19	1.36	78.4	0.14	4.56	135	2.67	3.49
microwave	x (ppb)	10.7	55.9	0.07	1.09	15.8	0.04	0.18	4.72	0.00	0.58
100% HNO_3	SD	30.6	12.1	0.04	1.10	11.2	0.02	0.24	3.18	0.11	0.35
	LoD (pM)	679	234	0.49	12.1	120	0.18	2.19	28.9	0.90	1.52
microwave	x (ppb)	108	19.2	0.23	0.97	48.4	0.07	1.61	68.7	0.36	3.39
50% HNO_3	SD	134	N/A	0.09	0.69	10.3	0.05	2.21	68.9	0.66	1.24
	LoD (pM)	2970	N/A	1.12	7.49	111	0.49	20.4	626	5.28	5.41

volume).

The limits of detection obtained were generally below the obtained background seawater and hydrothermal plume concentrations (see below), except for Zn and As. HISS-1 reference material was also analysed by the three methods. The mean and standard deviation of analysis are presented in Table 6.2 and the % of certified value (where available) is shown in Table 6.2.

The hotplate method (German et al., 1991) only digested ∼52% of Fe from a marine sediment sample, and considerably less Al (∼12%). This is likely to be due to the necessity to use HF to dissolved aluminosilicate material. Apparent contaminations for Zn and As were much larger in scale than for the blank filters (note 1000x dilution for analysis of standards in comparison with 20x for blank filters), suggesting that some part of the handling process of these sediment standards was the source of this error. The large dilution of these digests for analysis and very low concentration of these elements may have led to the apparent high recoveries. Zinc was problematic in general, and the blank filter contribution to the background samples was very high (Table 6.3). The microwave methods performed better for Al, and

Table 6.2: Certified reference material (HISS-1) recoveries for the three digest methods. B.D. = below detection limit. Typical dilution from digest solution = 1000x.

Method		Al	V	Mn	Fe	Co	Cu	Zn	As
	Certified	7300	6.80	66.10	2500	0.65	2.29	4.94	0.80
Hotplate	x (ppb)	857	3.85	33.9	1290	0.39	0.96	8.75	1.19
reflux	SD	38.8	0.19	3.27	67.4	0.02	0.29	3.01	0.34
100% HNO_3	% certified	11.7%	56.7%	51.2%	51.6%	59.8%	41.9%	177.0%	149%
microwave	x (ppb)	1786	5.29	50.6	1915	B.D.	B.D.	B.D.	1.38
100% HNO_3	SD	584	0.54	11.5	286				
	% certified	24.5%	77.8%	76.5%	76.6%				173%
microwave	x (ppb)	1814	4.16	34.9	1380	B.D.	B.D.	B.D.	0.46
50% HNO_3	SD	433	0.37	8.63	222				
	% certified	24.9%	61.1%	52.8%	55.2%				57.6%

the 100% HNO_3 digest typically dissolved ~77% of sediment Fe. All three methods are likely to dissolve relatively labile, freshly formed hydrothermal phases (Edmonds and German, 2004; German et al., 1991), but a more appropriate reference material for hydrothermal products would be most useful. In this study, the hotplate method was used in order to conform to the most relevant literature (Edmonds and German, 2004; German et al., 1991; Sands et al., 2012) for the best comparison of results. All values obtained should be considered as minimum estimates of 'total particulate' concentrations, and best estimates of 'total hydrothermal particulate' concentrations, after subtraction of background concentrations (as measured off-site; Table 6.3).

6.2.2.3 Background samples from the East Scotia Sea

Samples were taken from two depths at the background station at 59°40.898 S, 33°06.181 W (see Chapter 4) and in the vicinity of the hydrothermal vents above the plumes (e.g. at 1000 m depth). In total, five background samples were digested and the results averaged (Table 6.3).

Table 6.3: Background seawater particulate concentrations. The total error is calculated as the square root of the sum of squares of the blank error and average background error. Only the blanks from this particular sample set (n = 4) are used for this calculation.

	Al	P	V	Mn	Fe	Co	Cu	Zn	As	Ba
	nM	nM	pM	nM	nM	pM	pM	pM	pM	pM
1 ml solution	3,941	1,566	9,196	374	2,933	1,500	76,700	19,523	1,793	352,824
SD	108	63.2	496	34.5	96.2	94.3	5,608	13,579	147	38,809
Total error	590	271	590	36.1	488	238	22,404	21,827	1295	39,524
Seawater	0.79	0.31	1.84	0.07	0.59	0.30	15.3	3.90	0.36	70.6
± total error	0.12	0.05	0.12	0.01	0.10	0.05	4.48	43.7	0.06	7.90

Large errors are associated with the Zn measurement, which was similar in concentration in the blank and background sample digests. Arsenic is present in low concentrations in seawater particulates (pM levels) and the limit of detection is shown alongside data later. Hydrothermal particulate Fe concentrations are easily distinguished from background concentrations of ∼0.6 nM.

6.2.2.4 Sample analysis and calculation of total errors

Particles were collected by filtration of 10 L of seawater through acid cleaned 0.2 μm pore size polycarbonate filter membranes (Whatman), which were folded in half and frozen at sea, and defrosted in a laminar flow hood on shore. The filters were cut in half using ceramic scissors and one half was digested in concentrated HNO_3 for three days at 150℃ on a PTFE coated hotplate, as described above (German et al., 1991). The other half of the filter was set aside for spectroscopic analysis (see below). Digested samples were dried down, solvated into 1 ml 2% HNO_3 solution and then diluted 30x for analysis. SAPS samples were diluted ∼200x.

Total errors for samples (which have the background particulate concentrations subtracted) are calculated as $E_T = \sqrt{(E_{Bl}^2 + E_{BG}^2 + E_R^2)}$, E_{Bl} is blank error, E_{BG} is the subtracted background error (Table 6.3) and E_R is the percent error in the result based on the variability of the background samples.

6.2.2.5 Practical considerations

The hotplate method is by far the most time consuming, taking roughly 1 week (∼20 samples) and involving the most steps (and presumably the most potential for contamination and human error), whereas the microwave methods take less than one day for 16 samples - making them very useful for large numbers of samples. The microwave digest using 100% HNO_3 appeared to be the most effective in terms of digesting the filters: no filter pieces were recovered after the digestion. The presence of filter pieces after digestion in the other methods is concerning as some ions may absorb onto the surfaces, leading to a lower and inconsistent recovery of material. Filter remains from several hydrothermal samples were left to soak for two days in 3% HNO_3, to test this effect, and the resulting solution contained $<$2% of the recovered material for all elements studied except Cu (2.7%), As (3.2%) and Ba (3.4%).

Enhanced levels of major ions in samples can have a large effect on the ICP-MS measurement due to signal reduction when major ions absorb plasma energy. For this reason, several internal standards are typically added and the signal intensities corrected based on an interpolation of the reduction of signal (corrected to mass of the ion). Figure 6.1 shows an example analytical run, where one hydrothermal filter sample reduced the magnitude of the ICP-MS response (compared with ICP-MS standards) by over 60%. The background filters, taken from clean (non-hydrothermal) seawater give much less signal suppression, this may be due to the different (lower) composition of some ions, or the suppression of signal may be a cumulative effect over the course of the run - however, we would expect to see a slower return to normal signal magnitude for the CRM samples if this were the case. The interpolation of signal reduction and resulting correction is uniform across the atomic masses of interest - Be (9 amu), In (115 amu) and Re (186 amu) have very different masses and show very similar profiles - but the accuracy of the results after signal correction may be reduced by this effect.

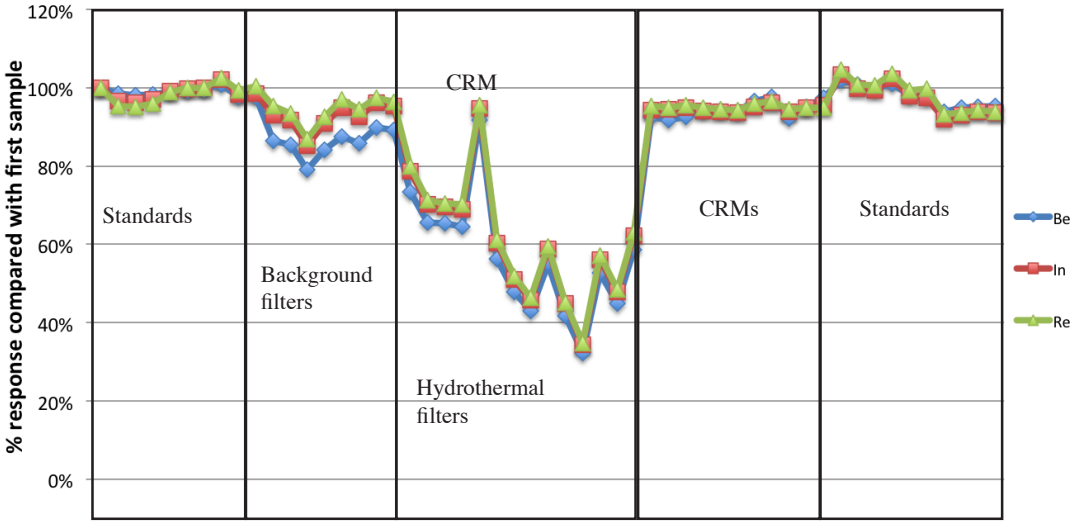

Figure 6.1: Internal standard drift on the ICP-MS during a typical run of samples. ICP-MS response can be significantly reduced by the sample matrix in filter digests. The return to signal response for a CRM during the run shows that the instrument did not suffer from drift in this run, and the consistency of signal reduction for the three internal standard elements shows that reduction is the same for all analytes of interest (e.g. Fe).

6.2.3 Individual particle analysis

Scanning Electron Microscopy (SEM; model LEO 1450VP), micro focussed X-Ray Fluorescence (μXRF) and micro focussed X-Ray Adsorption Fluorescence Spectroscopy (μXAFS) (Diamond Light source, Oxfordshire; Mosselmans et al., 2009) were used to examine several filters from each site (frozen at sea and defrosted in a laminar flow hood on shore) that were heavily loaded with particulate material from the buoyant plume (i.e. near vent samples taken by *Isis*. The SEM was also used to examine several SAPS filters from each site (some from the neutrally buoyant plume) for mineralogical description. The SEM was equipped with a Princeton Gamma Technology (PGT) light element Energy Dispersive X-Ray (EDX) microanalysis system for elemental analysis. Particles were identified using a backscatter display (also incorporated in the SEM), and spectra were collected over a period of 120 s. Three filters were successfully analysed by XAFS at the Diamond Synchrotron: two from the Kemp Caldera and one from E9S, a vent site located ~500

m south southeast of E9N with similar chemistry (James et al., in prep.). The filter samples were set into resin and mounted (sample side down) onto quartz slides, at which point the set resin and polycarbonate filter were ground down to expose a flat surface of sample mounted on quartz with no filter visibly remaining. Low-energy μXRF maps (for S, Si) were measured using a 2x3 μm beam (total map size 250 x 252 μm) by a silicon drift detector with a helium-filled bag surrounding the sample and detector to avoid X-ray signal adsorption by air. High-energy maps (for Fe, Cu and Zn) and μXAFS were measured using a 2x3 μm beam (total map size 300 x 300 μm) by a Ge detector in air.

6.3 Results

6.3.1 Elemental ratios

6.3.1.1 Phosphorus and vanadium

Phosphorus (P) and vanadium (V) both correlated well with Fe in all data sets. Differences were seen between vent sites (E2, E9N, Kemp Caldera; Figure 6.2), and from one year to the next in 2010 and 2011 (Figure 6.2 and 6.3). Some differences were also found between the SAPS samples (1 μm pore sized filters) and the samples filtered on board from the OTE bottles (0.2 μm pore sized filters), particularly for P. The obtained ratios of P:Fe and V:Fe are shown in Table 6.4 along with the ratios predicted by the trends discussed in Feely et al. (1998) and Edmonds and German (2004); see discussion. Some of the P:Fe ratios were highly variable (low R^2 values; Figure 6.2), but all correlations were accepted at the 0.01 significance level, except from the Kemp Caldera in 2010, with only three data points.

6.3.1.2 Other oxyanions: chromium and arsenic

Chromium (Cr) concentrations were only above the detection limit at E2 (Figure 6.4A-B), and Cr:Fe averaged 0.94 pM/nM in the plume and 0.37 pM/nM in all (plume + near vent) samples. It appeared that less Cr per Fe was incorporated in samples closer to the vents (Figure 6.4B). The obtained Cr:Fe ratio in the plume was intermediate to that found by at TAG (0.5 pM/nM; German et al., 1991) and

Table 6.4: Selected element to Fe ratios for the three sites over 2010-2011.

	E2	E9N 2010	E9N 2011	KC 2010	KC 2011
P:Fe (nM/nM)	0.19	0.29	0.55	0.36	0.41
Predicted ratio	0.15	0.16	0.16	0.17	0.17
V:Fe (pM/nM)	2.3	2.9	2.5	2.2	4.6
Predicted ratio	3.5	3.4	3.4	3.2	3.2
Mn:Fe (nM/nM)	0.043	0.15		0.09	0.16

the East Pacific Rise (1.3 pM/nM; Feely et al., 1994a). Arsenic to iron ratios varied greatly between sites and years (Figure 6.4C-D), and tended to be similar to or lower than previous measurements at the East Pacific Rise (Breier et al., 2012; Feely et al., 1994a). Several samples contained less As than the limit of detection (3σ of average blank), and this level is shown in Figure 6.4D.

6.3.1.3 Manganese

Manganese to iron ratios are presented in Figure 6.5 and Table 6.4. At E2, the Mn to Fe ratio was lower (0.043) than at E9N and the Kemp Caldera (0.15-0.16). The Mn:Fe ratio did not change in the plume samples between 2010 and 2011 at E9N, whereas at the Kemp Caldera the few samples taken in 2010 had slightly lower Mn:Fe ratios (0.09).

6.3.1.4 Cobalt, copper, zinc, barium and aluminium

Cobalt (Co) and barium (Ba) both correlated well with Fe in the plume samples (except Co in the Kemp Caldera; Ba was not measured for the E2 samples), whereas copper (Cu) and zinc (Zn) showed weak correlation (Figure 6.6). These elements are typically present in poly-metallic sulfide particles (Co, Cu, Zn) or barite (Ba) and may be co-diluted with Fe in the buoyant plume, subject to differential settling or dissolution (German et al., 1991; Trocine and Trefry, 1988). Particulate aluminium was rarely found above 5 nM (data not shown), but as explained previously, the digest method employed was not sufficiently strong to fully digest aluminosilicate material (German et al., 1991).

6.3.2 Particle mineralogy & composition by spectroscopy

6.3.2.1 SEM imaging

A large range of particles was present on filters taken from the three study sites, with sulfides and barite dominating the near-vent samples taken by *Isis* (filtered through 0.2 μm filters; Figure 6.7), and background siliceous material dominating the 1.0 μm SAPS filters taken higher in the water column (Figure 6.8). The hydrothermal particles found on the SAPS filters were barite, Fe oxides and silicates, in order of abundance. A higher abundance of sulfide particles was found on SAPS filters taken in the buoyant plumes. The barite particles showed a marked difference as the plume dispersed, becoming smaller, smoother and rounder with dispersion (Figure 6.7 and 6.8). It was noted that the barite particles showed up much brighter than other particle types (particularly sulfides) by optical backscatter, and therefore were more easily identified and perhaps preferentially selected for analysis. Most of the sulfide particles (Zn, Fe, some Cu) were small, often only slightly larger than the pore holes on the filter being examined. Fe oxides and silicates (identified by presence of Fe (and Si) and lack of S) were usually conglomerates of smaller particle units, as previously reported (Feely et al., 1990; Nelsen et al., 1987). Silicates and mixed phases (containing Si, Mg, Ca, Fe, Zn, Ti, S, organic matter) were present on all filters, particularly in the near vent samples. Globules of elemental sulfur were occasionally found at all three sites (Figure 6.7F), but at the Kemp Caldera fine particles of elemental sulfur were present on all parts of the filter, as evidenced by high S:Fe or S:Zn stoichiometry (e.g. >2) in particles identified as sulfides.

The E2 and E9N/E9S filters were fairly similar in the variation and nature of particulates - no differences could be established due to the small sample sets and differences in sample depths, sediment incorporation and filter volumes. The Kemp Caldera filters were remarkably different in that they contained pyrite framboids (Chapter 5) and were often dominated by elemental sulfur (Figure 6.9). Most particles present were less than 3 μm in diameter, i.e. smaller than the size of the micro focussed X-Ray beam at the I-18 beamline at the Diamond Light Source.

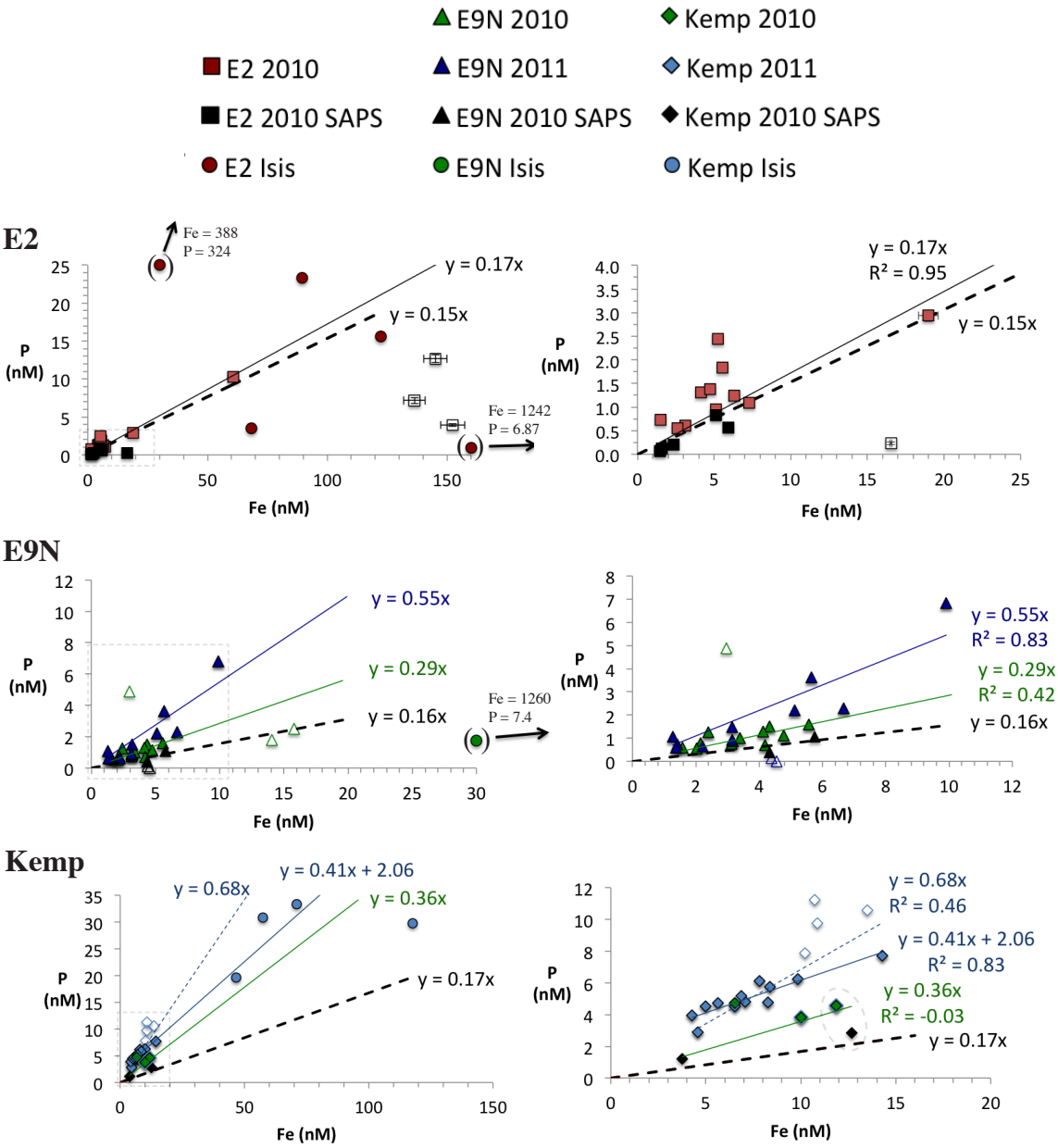

Figure 6.2: Background subtracted particulate P vs. Fe plots for the three sites. All data are shown in the left panels, and samples away from the immediate influence of the vents are shown in the right panels. In cases where anomalous samples are not used in a regression, the data points are shown as unfilled symbols. The dotted black lines show the predicted P:Fe ratios (see main text). In these figures, the error bars for the analysis are also shown (see main text). For clarity, these are not shown in the other figures in this chapter - errors are usually within the size of the data point. For E9N, regressions are shown for the 2010 and the 2011 data separately. For the Kemp Caldera in 2011, two regressions are shown (all data and filled data points only). The CTD bottle and SAPS data point shown within a dotted ellipse were taken from the same depth at roughly the same time (in 2010). The other SAPS sample was taken in the large particle plume at 930 m depth.

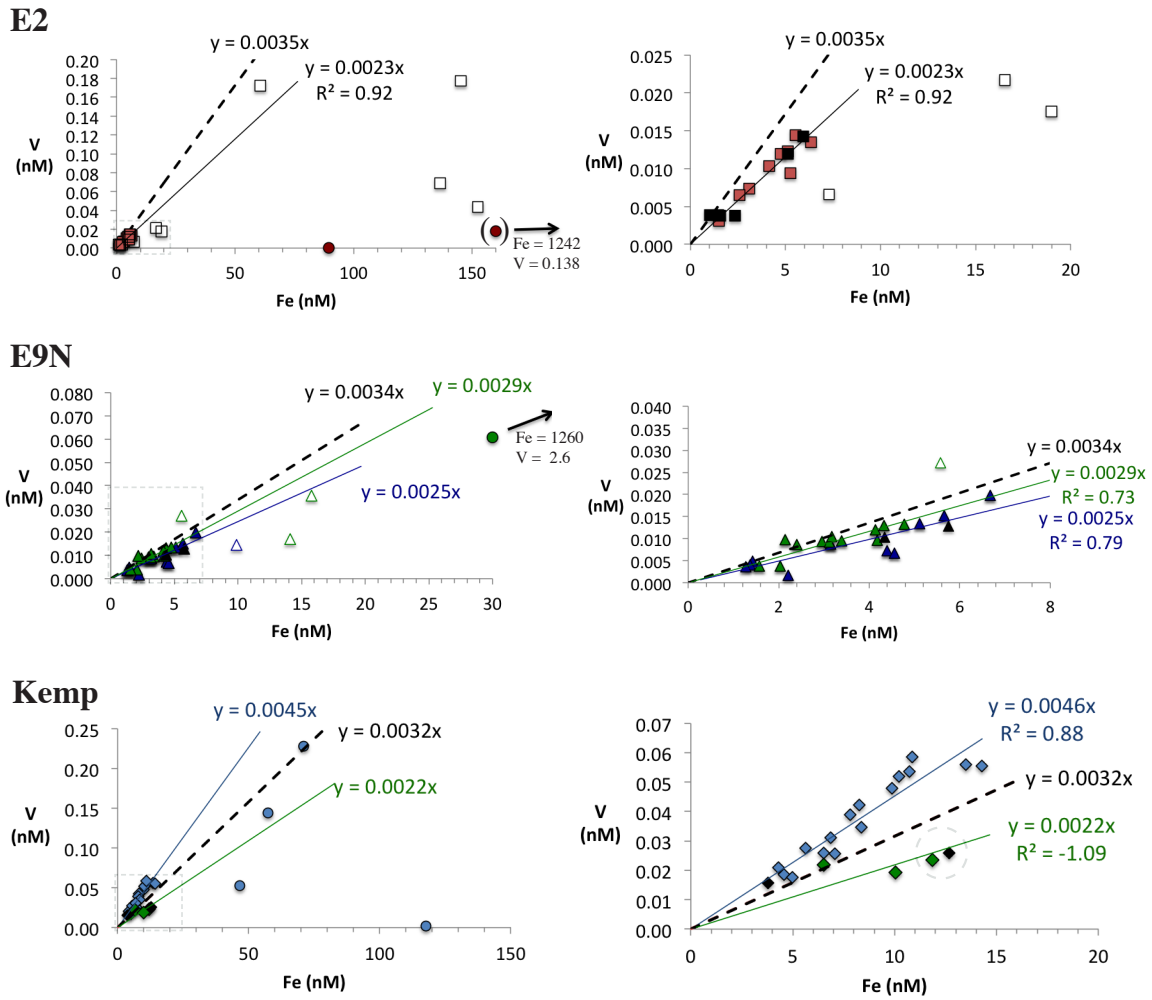

Figure 6.3: Background subtracted particulate V vs. Fe plots for the three sites. The predicted V:Fe ratios are shown as black dashed lines. The CTD bottle and SAPS data point shown within a dotted ellipse at Kemp were taken from the same depth at roughly the same time (in 2010). See Figure 6.2 for legend.

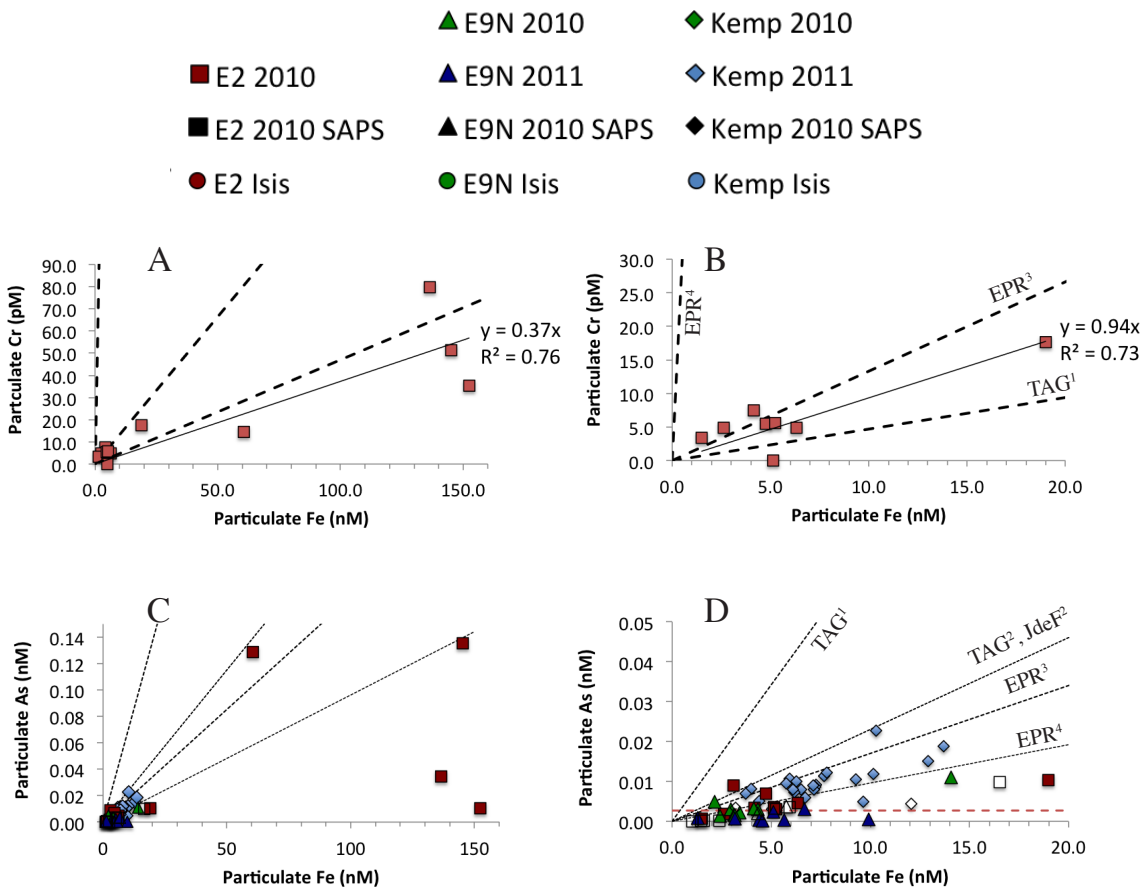

Figure 6.4: Background subtracted particulate Cr (A-B) and As (C-D) vs. Fe. Data from all three sites over both years are shown in the same plots. All data are shown in the left panels, and the samples away from the immediate influence of the vents are shown in the right panels. The dotted lines show the ratios presented in German et al. (1991) (TAG[1]), Feely et al. (1991) (TAG[2], Juan de Fuca[2]), Feely et al. (1994a) (EPR[3]) and Breier et al. (2012) (EPR[4]). The red dashed line in D shows the limit of detection for As.

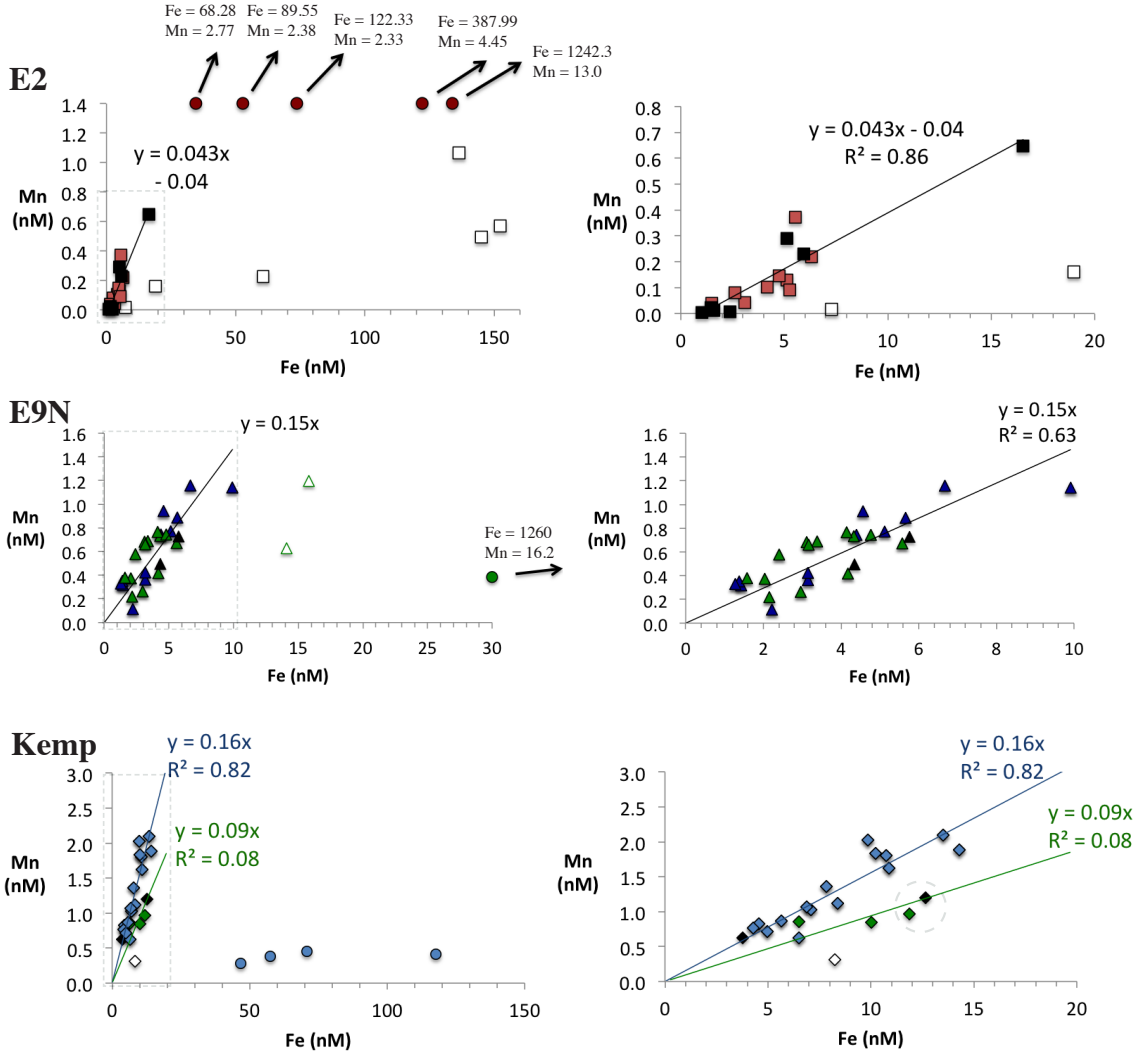

Figure 6.5: Background subtracted particulate Mn vs. Fe plots for the three sites. The CTD bottle and SAPS data point shown within a dotted ellipse at Kemp were taken from the same depth at roughly the same time (in 2010). See Figure 6.4 for legend.

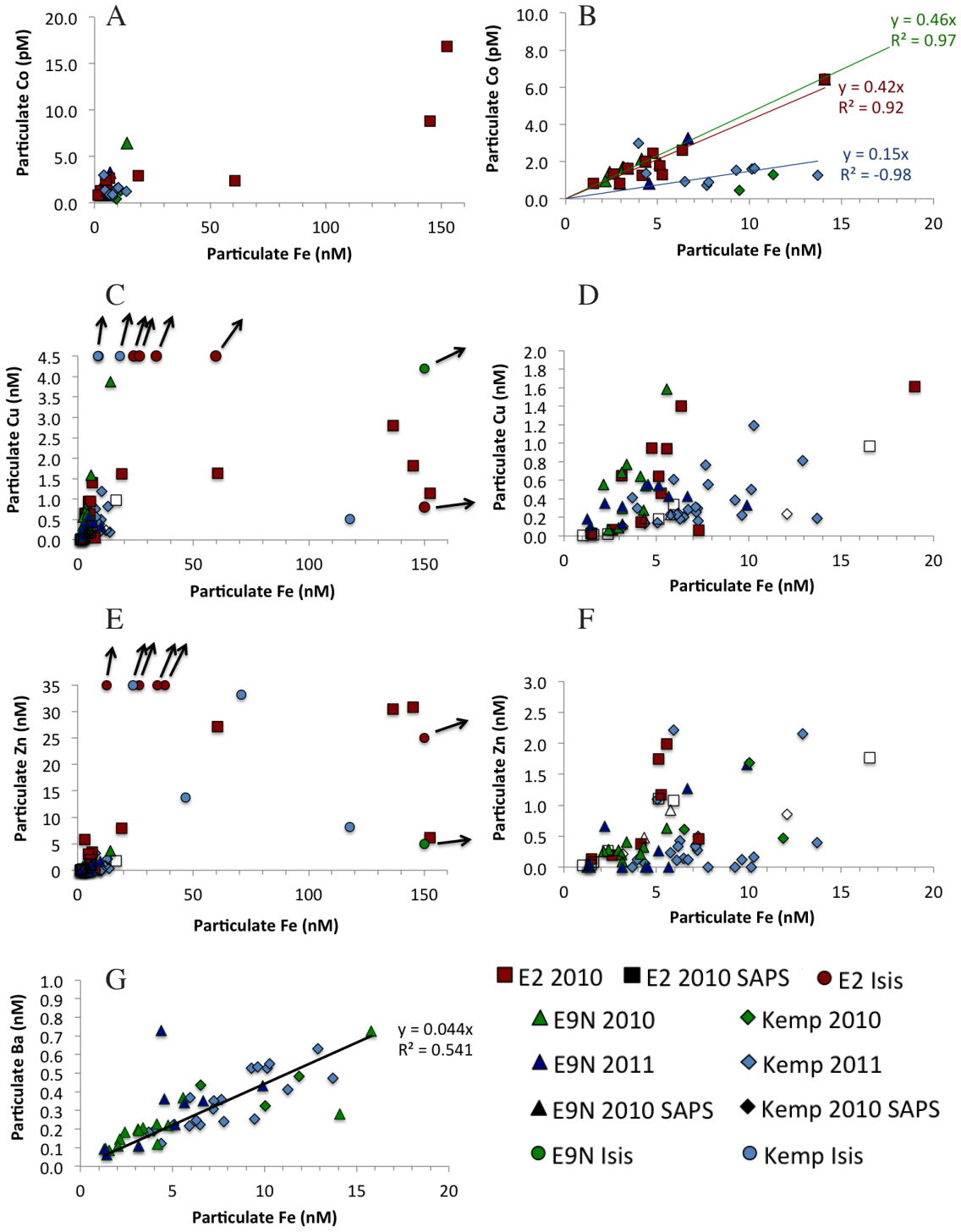

Figure 6.6: Background subtracted particulate Co (A-B), Cu (C-D), Zn (E-F) and Ba (G) vs. Fe. Data from all three sites over both years are shown in the same plots. All data are shown in the left panels, and the samples away from the immediate influence of the vents are shown in the right panels. For Co, a trend is shown for each site individually and for Ba a combined trend for E9N and the Kemp Caldera is shown. No trends are shown for Cu or Zn as these elements did not co-vary in consistent ratios with Fe.

6.3.2.2 XAFS analysis

Four filters (one from E2, one from E9S, two from the Kemp Caldera) were selected for area analysis by XRF and point analysis by XANES at the Diamond Light Source (Oxfordshire). They were chosen due to the abundance of hydrothermal particles based on the SEM work. At the light source, no areas with sufficiently high particle concentrations were found on the E2 filter, and the two filters from the Kemp Caldera were similar, so only one is described here. The differences found by XRF over a $\sim$0.3 mm^2 area confirmed the conclusions of the SEM work: sulfur was more abundant on the Kemp Caldera filters (Figure 6.9), and was not necessarily associated with metals (Fe, Cu, Zn) although these metals were found in several particles. Metals were much more enriched on the E9S filter (Figure 6.9A), consistent with the SEM observations and the more metal rich vent fluid compositions at the ESR sites compared with the caldera (Connelly and others, in prep.; James et al., in prep.). Particles $\leq$3 μm in size only represent one pixel on the XRF maps, and particles much greater in size were selected for XANES analysis and were compared with Fe standards, as indicated in Figure 6.9.

6.4 Discussion

A mixture of phases was observed in the near vent samples and plume samples both by spectroscopy and by examination of the elemental composition of bulk digests. The samples were predominantly taken in close vicinity of the vents ($<$1 km) in comparison to many other studies, which sampled much larger dispersive plumes, often averaging material from several vent sites (e.g. Edmonds and German, 2004; Feely et al., 1996, 1991). Other vent plumes (particularly along faster spreading ridges) also typically contain much higher concentrations of particulate Fe (Feely et al., 1996), facilitating bulk digest analysis and distinction from background particulate matter.

In this discussion, I consider the distribution of several elements in the three systems studied and reflect on what can be learned about their behaviour in hydrothermal vents in back-arc and island arc settings. The elemental ratios of the near vent

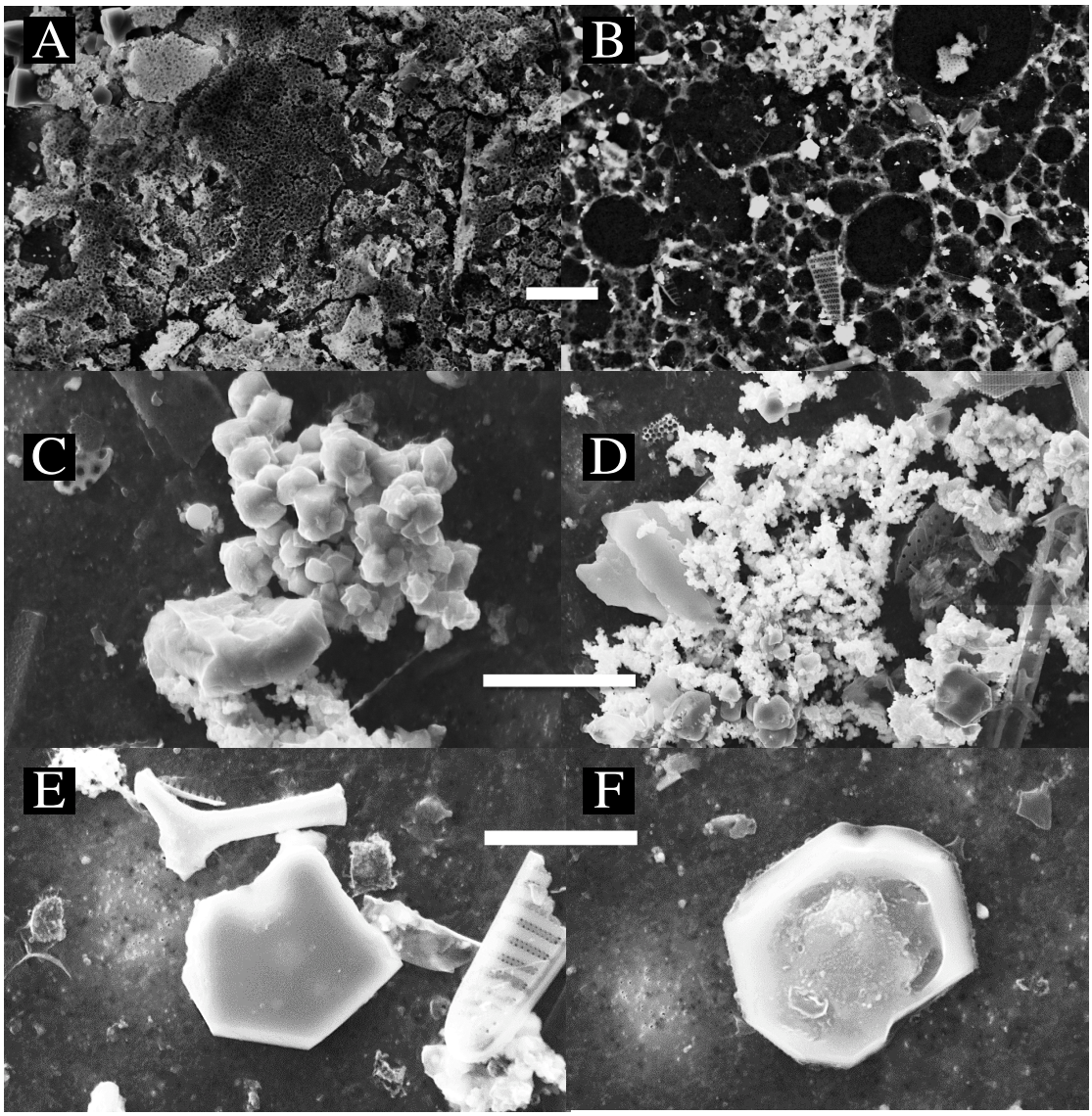

Figure 6.7: Typical particles filtered from Isis OTE bottles. A-B: Fe/Zn sulfide honeycombe structures (scale bar 20 μm). C: Fe sulfide cluster, D: Zn sulfide cluster, E: rough barite particle, F: elemental sulfur, (C-F taken from the same filter at E2, scale bars 10 μm).

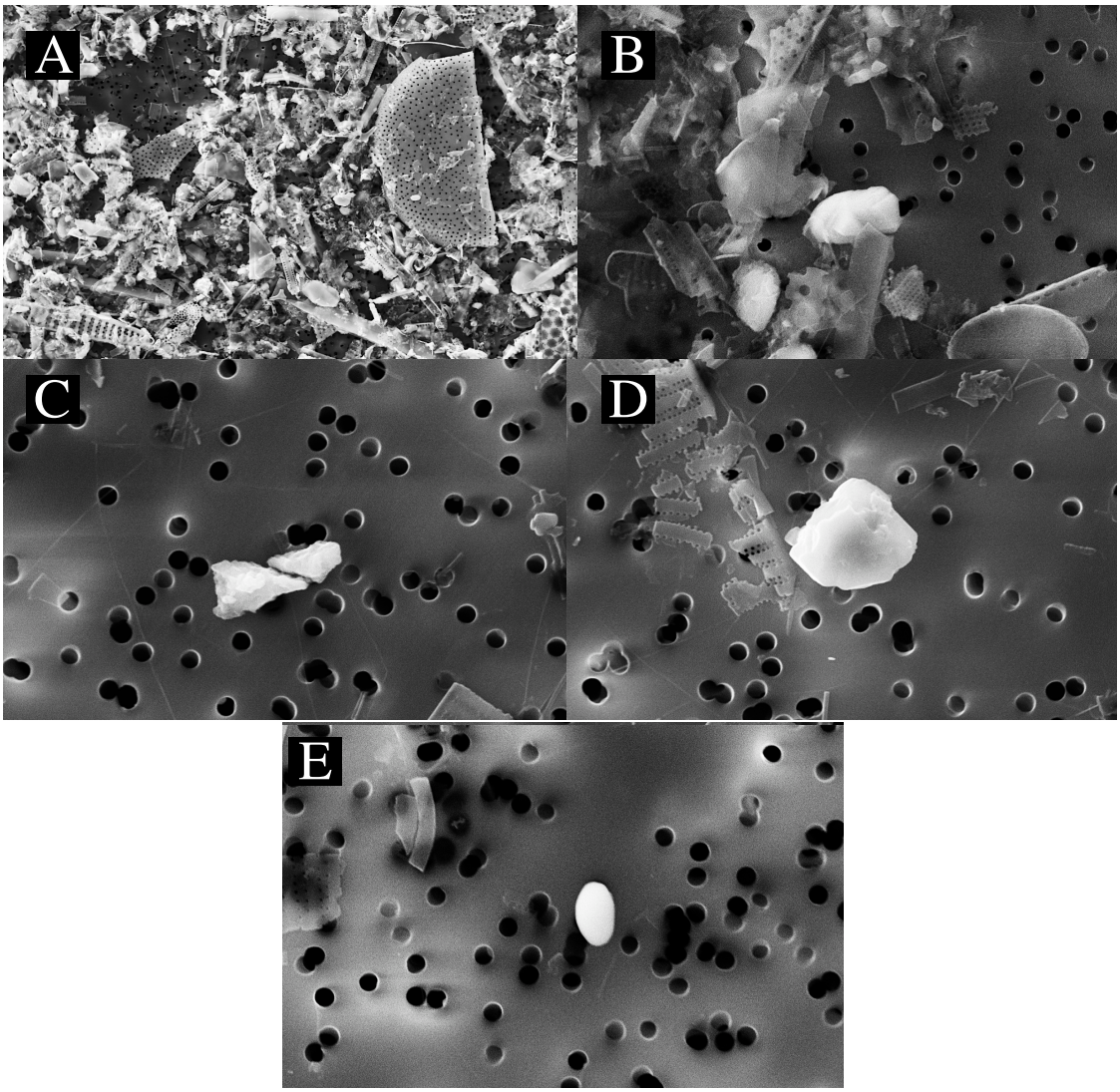

Figure 6.8: Typical particles found on SAPS filters. A: Siliceous (non-hydrothermal) material at 2375 m depth (∼225 m above vent orifice, E2 2010). B: Chalcopyrite particle (in centre) at 2385 m depth (∼15 m above vent orifice, E9N 2011). C, D and E: Fe oxy-hydroxide particle, silicate particle and smoothed barite particle (respectively) at 1413 m depth (10 m above vent orifice, Kemp Caldera, 2010). For scale, the pore holes are machined to 1 μm diameter - note larger scale in A. Siliceous material dominated the filters.

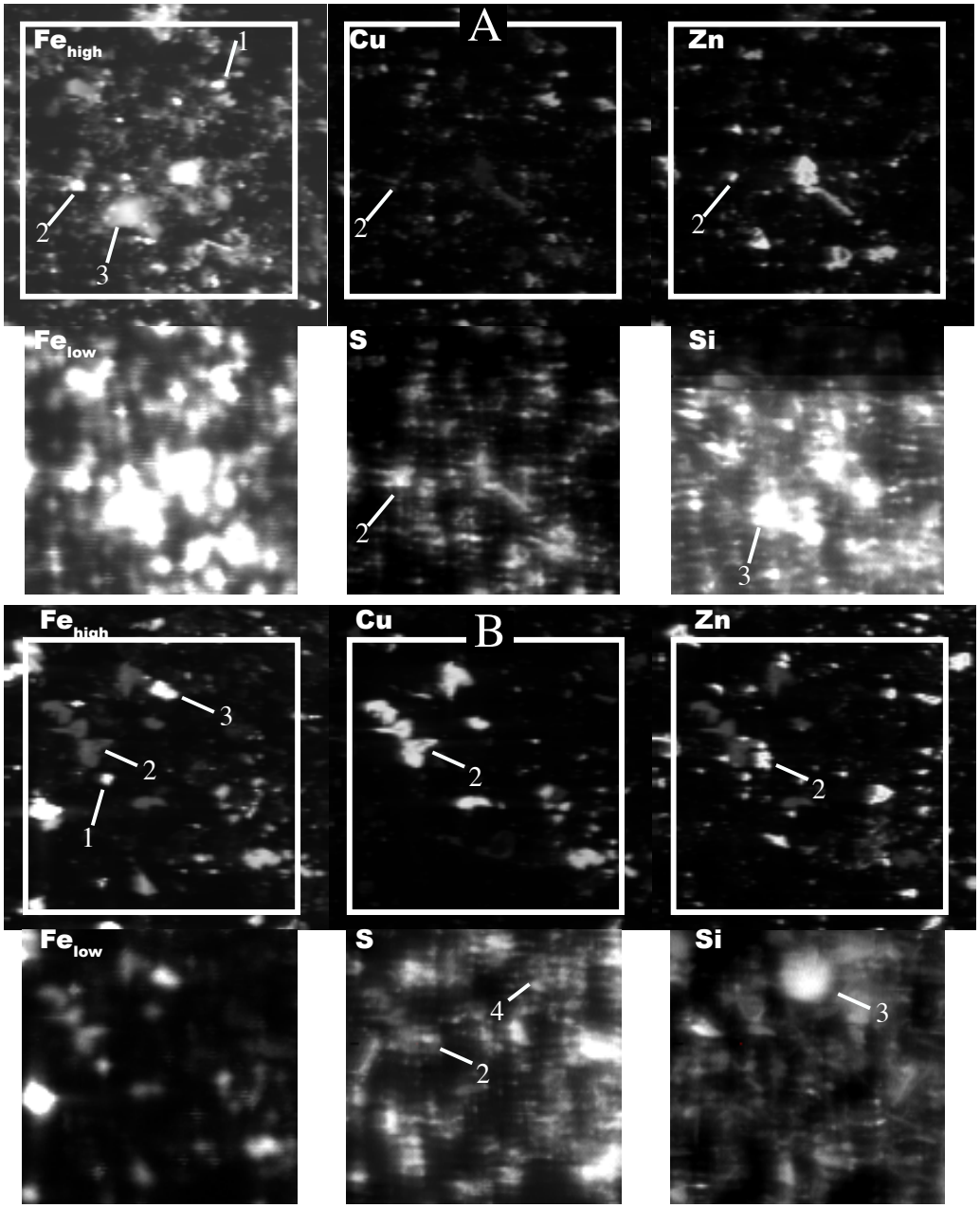

Figure 6.9: XRF maps for A: Isis 142 (E9S) and B: Isis 152 (Kemp Caldera). Maps obtained with a high energy beam are shown along the top rows (300 μm square) and with low energy along the bottom rows (250 μm square, position indicated on the top row with a white square). The signal intensity ranges are the same for both sets of maps, but due to repositioning of the filters and adjustments to the beam the intensities are not quantitatively equal. However, zinc (high energy) and sulfur (low energy) give reasonably similar intensities between the two filters, allowing good comparison of the intensities of the other elements. For example, the Fe signal is clearly more intense on the filter from E9S (A), whereas sulfur is equally or less intense. 1: Fe oxide, 2: Poly-metallic sulfide, 3: Fe silicate, 4: Elemental sulfur; as determined by XANES analysis.

samples taken by *Isis* are not generally discussed further as the ROV operations clearly led to the inclusion of sedimentary phases into the bottles (as evidenced by the presence of sedimentary pyrite framboids in some samples in the Kemp Caldera) - so elemental ratios in these samples do not necessarily reflect natural plume processes.

6.4.1 Phosphorus and vanadium

6.4.1.1 Predicted ratios based on dissolved phosphate

Dissolved phosphate (PO_4^{3-}) is depleted in surface waters as it is consumed as a nutrient, and is re-mineralised in deep waters after sinking and dissolution of organic matter. The deep ocean concentration of dissolved phosphate is related to how recently the water was ventilated at the surface, meaning that concentrations are lower in the north Atlantic Ocean ($\sim$1 μM; Edmonds and German, 2004) and higher in the north Pacific Ocean (3 μM, Feely et al., 1991). The analysis of hydrothermal plume precipitates led researchers to suggest that the P:Fe ratio in hydrothermal oxy-hydroxides was directly related to the concentration of ambient phosphate (Feely et al., 1991), therefore suggesting that the concentration of phosphate was the limiting factor in the amount of scavenging during rapid precipitation of hydrothermal oxy-hydroxides (Rudnicki and Elderfield, 1993). Vanadate is comparatively uniformly concentrated in seawater (Feely et al., 1998), and vanadium incorporation in hydrothermal oxy-hydroxide particles was inversely dependent on phosphate concentration, suggesting that the vanadate ion was out-competed by phosphate during precipitation (Edmonds and German, 2004; Feely et al., 1998). This research led to two equations (most recently updated in Edmonds and German, 2004; Equations 6.1 and 6.2) relating phosphate concentration with V:Fe and P:Fe in hydrothermal oxy-hydroxide particles.

$$\mathrm{P/Fe} = 0.0492[\mathrm{PO_4^{3-}}] + 0.0476 \tag{6.1}$$

$$\mathrm{V/Fe} = -0.0010[\mathrm{PO_4^{3-}}] + 0.0056 \tag{6.2}$$

6.4.1.2 Observed P:Fe and V:Fe ratios at E2 and E9N

The obtained P:Fe and V:Fe ratios for the three sites over the two sampling cruises are shown in Table 6.4. While at E2 the P:Fe ratio was similar to that predicted by Equation 6.1 for many samples, several samples contained additional P (Figure 6.2) - possibly indicating a natural or contamination source of P. At E9N over both years the trend in P:Fe was higher than predicted by Equation 6.1, increasing greatly from 2010 to 2011 from 0.29 to 0.55 (predicted 0.16 - see phosphate concentrations in Table 2.1). This increase was accompanied by a decrease in V:Fe (from 2.9 to 2.5, predicted 3.4 pM/nM), supporting the theory that P:Fe is preferentially incorporated into Fe oxy-hydroxides, or suggesting that additional (non V-containing) sulfide phases were sampled in 2011 and that the additional P was the result of a different P-containing mineral (Resing et al., 2007). Sulfides are in many instances not found above the first few metres of plume rise (German et al., 2010) as they tend to be larger and settle more quickly (Trocine and Trefry, 1988), but some workers have reported the distribution of sulfur or sulfide phases throughout the dispersing plume (Breier et al., 2012; Feely et al., 1996; Resing et al., 2007; Yücel et al., 2011). This may be particularly important in cases where vent H_2S is in large excess over Fe (Feely et al., 1996), such as in the vent sites in this study (see Chapter 2). Some differential settling of sulfide and oxy-hydroxide phases is still expected, so it is unusual to find such good linear (rather than curved) correlations.

Poor analytical reproducibility is unlikely to fully explain the variability in P:Fe - the total error (E_T; Section 6.2.2.4) is usually within the size of the data points (Figure 6.2). However, the Fe (and P) concentrations found here are considerably lower (and closer to background concentrations and the limits of detection) than at many other vent sites (Edmonds and German, 2004; Feely et al., 1998; Sands et al., 2012; Trocine and Trefry, 1988), making assessment of hydrothermal (and not background) effects more challenging.

Interestingly, the SAPS filters taken in 2010 conformed better to the predicted ratios than the 0.2 μm filters taken from the OTE bottles in the same year and in 2011 (Figures 6.2 and 6.3). Differences in oxyanion:Fe ratios are not expected in different

size fractions (Sands et al., 2012) and increased scavenging over the time of sample recovery and filtration is not expected (Metz and Trefry, 1993). Also, a sample filtered from an OTE bottle taken from the same position as a SAPS filter gave fairly similar concentrations for P, V, Mn and Fe (Figures 6.2, 6.3 and 6.5; shown by dotted ellipse for Kemp Caldera site), suggesting that an operational effect was not responsible for these differences. Phosphorus concentration was the most different of the four elements, and it is possible that whatever P-containing particulate species increased the apparent P:Fe ratio in several samples was typically in the 0.2 - 1.0 μm size range, and that for this reason it did not settle easily (Yücel et al., 2011) and was co-distributed with the oxy-hydroxide phases.

Low V:Fe ratios were found at the East Pacific Rise by Breier et al. (2012), accompanied by low P:Fe ratios, and in contrast with previous results of Feely et al. (1994a) for the same region. The different analytical approach used (microwave digestion followed by ICP-MS vs. spectroscopic analysis by X-Ray adsorption spectroscopy) may cause some differences, but good reproducibility between the studies of Feely et al. (1998, 1991) and Edmonds and German (2004), who used a hotplate digestion method, suggest that the differences are more likely due to sampling strategy. The work at mid-ocean ridges that tend to conform well to the phosphate concentration predictions tends to be conducted over large dispersive plume areas - possibly averaging material from several vent sites (Edmonds and German, 2004; Feely et al., 1996, 1994a, 1991) and not in the close vicinity of the vents (Breier et al., 2012; Figure 6.10).

6.4.1.3 Observed P:Fe and V:Fe ratios in the Kemp Caldera

The Kemp Caldera site provided further insight into the conundrum of the increased oxyanion:Fe ratio in hydrothermal plumes, as it is a high sulfidation vent site with distinctly different chemistry (see Chapter 2 and 5). The particulate matter in the caldera was highly enriched in P, with a P:Fe ratio of 0.42 (predicted 0.17). The V:Fe ratio in the caldera was also much higher than expected at 4.6 pM/nM (3.2 pM/nM predicted). Island arc vent sites are typically rich in magmatic gases and the resulting hydrothermal plumes can be highly enriched in Fe and acidity

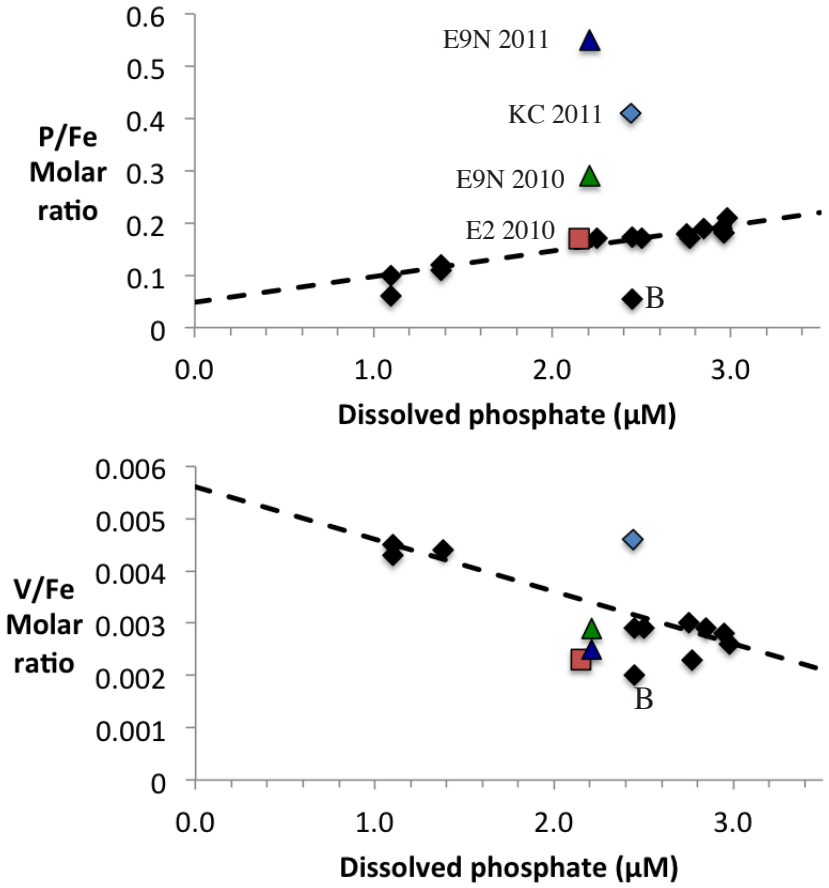

Figure 6.10: P:Fe and V:Fe ratios plotted against dissolved phosphate and compared with data presented in Edmonds and German (2004); Feely et al. (1998); Sands et al. (2012) and Breier et al. (2012) ('B' on plots). The Breier et al. study (2012) found lower P:Fe and V:Fe ratios than usual, possibly due to the inclusion of several Fe containing phases (not only Fe oxy-hydroxides).

(Leybourne et al., 2012; Resing et al., 2007). The Fe oxidation rate is lower in these settings, leading to slower precipitation and aggregation and a large pool of colloidal Fe (Chapter 5). The more gradual formation of Fe oxy-hydroxides via a long-lived colloidal intermediate likely leads to a higher adsorptive surface area per amount of Fe and the greater incorporation of surface active oxyanions, which apparently co-precipitate with available surfaces more rapidly than typical precipitation rates (Feely et al., 1990, 1994b; Rudnicki and Elderfield, 1993).

The balance between the rate of oxidation/coagulation and the dilution of vent species plays a crucial role in how much of Fe oxy-hydroxide material is in the colloidal and particulate phases at the point of sampling (Field and Sherrell, 2000). It is likely that the samples taken in the Kemp Caldera were far from venting, as signals (LSS, Eh) of plumes rich in Fe particles were not found at the sample stations (Chapter 5). The particulate oxy-hydroxides present are very likely to be aggregations of the pervasive colloids (Honeyman and Santschi, 1989) and the incorporated oxyanions probably co-precipitated with the oxy-hydroxides during their initial formation at venting some time previously (Metz and Trefry, 1993; Rudnicki and Elderfield, 1993).

High P:Fe (up to 0.56) and V:Fe (up to 7.1 pM/nM) ratios have been found previously in island arc (acidic) environments (Leybourne et al., 2012; Resing et al., 2007), and higher acidity coincided with greater P:Fe ratios (Resing et al., 2007), although other P containing phases were suggested to exist at this site. The results presented here suggest that a different mechanism of scavenging in these environments should be considered. It may be the case that phosphate incorporation into oxy-hydroxides is at least partly controlled by Fe(II) oxidation rate, which is indeed slower in the north Pacific Ocean than the Atlantic Ocean (Field and Sherrell, 2000), and is probably the dominant control on P:Fe concentrations in island arc environments (Figure 6.11). One implication of this suggestion is that the fluid chemistry (e.g. acidity) may have changed at E9N between 2010 and 2011, when we were not able to observe and sample the vents by ROV. Other differences in Fe speciation from 2010 to 2011 were not apparent at E9N (Chapter 4).

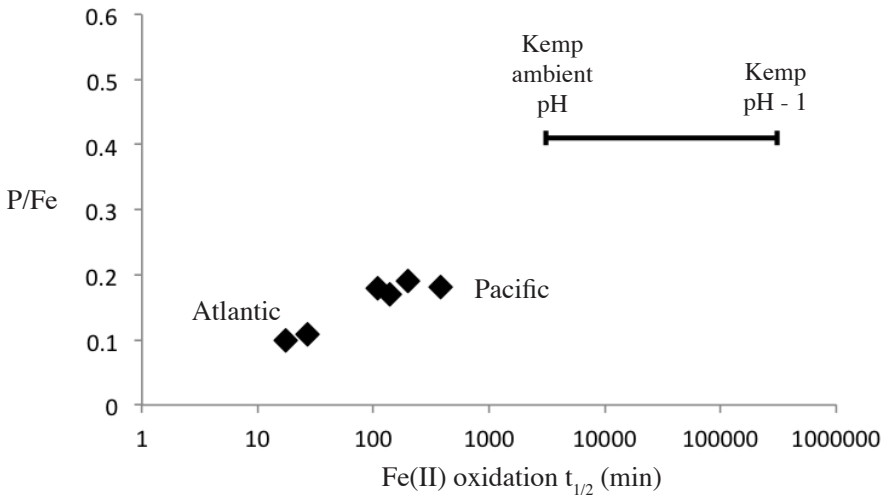

Figure 6.11: P:Fe ratio model considering Fe(II) oxidation rate as the limiting factor rather than dissolved phosphate. Values of P:Fe from Feely et al. (1998) and Edmonds and German (2004) are combined with oxidation rates from Field and Sherrell (2000). Fe(II) oxidation rates for Kemp are calculated as described in Chapter 1 (Equation 1.1) and the range of oxidation rates is shown for likely pH deviations from ambient conditions in the Kemp plume. It is likely that Fe-oxyhdroxides formed close to ambient pH.

6.4.2 Arsenic and chromium

Arsenic to iron ratios in hydrothermal plumes have not been shown to vary predictably like P or V, despite a slight difference in arsenate concentrations in the Atlantic (∼20 nM) and Pacific (∼25 nM) (Andreae, 1979; Cutter et al., 2001) - in fact, the highest As:Fe ratios reported were in the Atlantic at the TAG vent site (German et al., 1991; Figure 6.4D). The lack of dependence of As:Fe on dissolved ambient As(V) is probably due to variable arsenic concentrations in vent fluids (Von Damm, 1990), and due to the additional incorporation of As into sulfides (Breier et al., 2012) which would tend to interrupt any predictable Fe:As relationship as the plume develops and the oxides and sulfides fractionate through differential settling (Trocine and Trefry, 1988). Arsenic incorporation into oxy-hydroxides was higher at E2 and in the Kemp Caldera (Figure 6.4D), and in the case of the Kemp Caldera this may be attributed to greater scavenging by colloids as discussed for P and V. Chromium (Figure 6.4B) has similar concentrations to As, with very low concentrations in

seawater (< 5 nM; Connelly et al., 2006; Jeandel and Minster, 1987) and some (variable) enrichment in vent fluids (e.g. Jeandel and Minster, 1984; Sander and Koschinsky, 2000), leading to unpredictable Cr:Fe ratios in plume particles. It is therefore uncertain whether hydrothermal plumes act as a source or sink of Cr in seawater, but the relationship found at the TAG vent site suggested hydrothermal plumes should act as a sink for Cr (German et al., 1991). Only E2 had sufficient concentrations of Cr for analysis, possibly indicating that the vent fluids at E2 were more concentrated in As and Cr than at E9N.

6.4.3 Manganese

Manganese is an example of an element that can be scavenged by Fe oxy-hydroxides through surface activated oxidation (Davies and Morgan, 1989). Scavenging of elements onto particles is quite different from co-precipitation in the context of a developing hydrothermal plume, and tends to lead to a curved scatter plot of the element plotted against Fe (unlike the linear plot of oxyanions), as a greater proportion of the element is incorporated into particles over time (German et al., 1991; Rudnicki and Elderfield, 1993).

For Mn, an unusually linear relationship was obtained for the dispersing plume particles at all three sites (Figure 6.5), and very little Mn was found in the near-vent samples, which presumably contained a much greater proportion of sulfide phases. The ratio Mn:Fe was 0.04 at E2, compared with 0.15 and 0.16 at E9N and the Kemp Caldera, respectively. It is likely that the higher gas concentrations and more reducing nature of the E9N and Kemp vent sites (Connelly and others, in prep.; James et al., in prep.) led to increased bacterial activity at these sites (Urabe et al., 1995), more manganese oxidation (Cowen and Li, 1991; Cowen et al., 1990), and therefore more precipitation of Mn (Feely et al., 1996).

6.4.4 Copper, zinc, cobalt, barium and aluminium

Copper, zinc and cobalt are chalcophilic elements (have affinity for sulfur) and as such are rapidly removed from solution in the early stages of mixing with seawater (German et al., 1991; Klevenz et al., 2011; Trocine and Trefry, 1988). Copper, zinc

and barium were all present in many particles identified by SEM and XRF on filters taken in the near vent regions at all three sites. Limited conclusions can be taken from the abundance of particles from E2 and E9N or E9S due to the small sample sets and differences in exact sample environment (altitude from vents, etc.). The filters from the Kemp Caldera were more dominated by Zn sulfides than at the ESR sites, and the morphology of the Fe sulfides was distinct, given the presence of pyrite framboids. Most sulfides identified by XRF were poly-metallic, containing Fe, Cu and Zn (Figure 6.9), though Fe easily outweighed the other metals on the E9S filter.

The chalcophile elements are not usually found in high concentrations in particles in the dispersing plume, and are proportionally more important closer to the vent source (Feely et al., 1994b; German et al., 1991; Trocine and Trefry, 1988). In the three plumes studied here particulate Cu and Zn were not present at concentrations higher than 5 and 30 nM, respectively (Figure 6.6), except in the near-vent samples taken by *Isis*, which probably included sedimentary material (Chapter 5), and are not discussed here. Generally, particulate Cu and Zn concentrations were less than 2 nM (close to background levels and, for Zn, near to the limit of detection), with little dependence on Fe concentration (Figure 6.6C-F). Cobalt varied quite linearly with Fe in the plumes, possibly reflecting additional adsorptive sink of seawater cobalt (present at 10-50 pM; Martin et al., 1993, 1989) into particles. Co was lower in the Kemp Caldera particles, suggesting either that Co concentrations were lower (relative to Fe) in the vent fluids or that Co had been depleted in the caldera due to the persistence of venting, lack of ventilation, and the low ambient concentrations.

Barium is present in hydrothermal plumes as barite ($BaSO_4$), usually at low concentrations (Feely et al., 1990; Mottl and McConachy, 1990). It is the result of the reaction of vent-enriched barium with seawater sulfate. Barium showed good correlation with Fe in the particulate phase at E9N and the Kemp Caldera (not analysed at E2), suggesting that barite is dispersed and diluted with Fe oxy-hydroxides without much fractionation by settling. These particles were all found to be common

close to the vent sites under examination by SEM (Figure 6.7) and XRF (data not shown), and barite was common on SAPS filters taken in the dispersing plume (Figure 6.8), where it was generally more smoothed and rounded than close to the vents.

If particulate aluminium was increased in the Kemp Caldera as reported for other island arc sites (Butterfield et al., 2011; Leybourne et al., 2012; Resing et al., 2007), then it was not readily digestible by the technique employed here (German et al., 1991). These phases (possibly alunite, also P-containing woodhouseite) may have settled closer to the unknown vent site (Chapter 5), while Fe and Mn oxy-hydroxides continued to precipitate and settle more gradually.

6.5 General discussion and conclusions

A greater proportion of sulfide phases was present closer to the hydrothermal vents, as these phases have lower solubility products than Fe/Mn oxides (Feely et al., 1996) and precipitate first (Klevenz et al., 2011), settle faster (Trocine and Trefry, 1988) and do not continue to aggregate like oxy-hydroxides (Field and Sherrell, 2000). Cu, Zn and Fe sulfides and mixed silicate phases were common on near-vent filters and SAPS filters taken close to vent orifices. In the Kemp Caldera, sedimentary framboids and elemental sulfur were also sampled (Chapter 5).

After further dispersal at the ESR sites (i.e. further from the seafloor), the plumes sampled were still a mixture of phases as evidenced by the significant inputs of different elements (oxyanions, manganese, barium and chalcophiles) into the particulate phase. Oxy-hydroxides were readily identified by relationship of oxyanions and Mn with Fe, and variations in these relationships for individual samples suggests that other phases were contributing to the concentrations of some elements. When Mn is plotted against V, other facets of the mixture of phases sampled become more clear (Figure 6.12) - the samples which fall on the predicted line by relationships with Fe are presumably dominated by Fe oxy-hydroxides, whereas V rich samples are probably early stage oxy-hydroxides which haven't scavenged as much Mn, and Mn rich samples taken by *Isis* may include Mn sulfides or sediments. On larger datasets it is

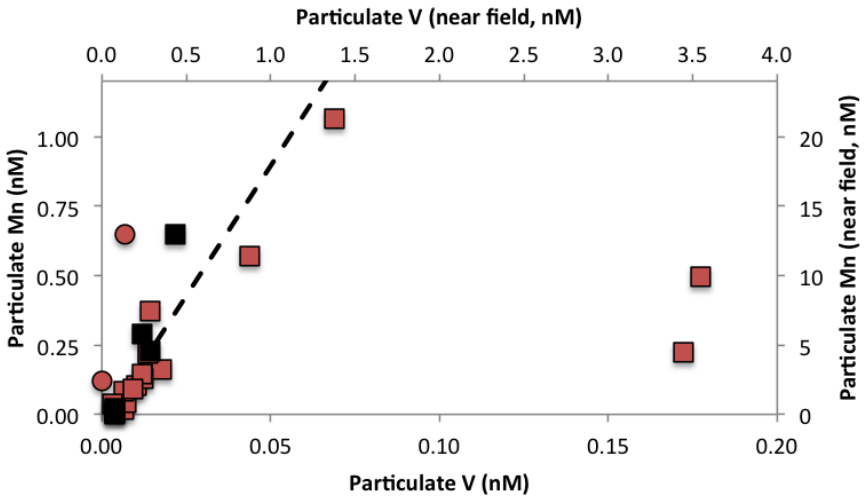

Figure 6.12: Particulate Mn plotted against particulate V at the E2 site. The symbols are the same as in Figures 2-5, i.e. red squares are OTE samples, black squares are SAPS samples and the red circles (plotted on secondary axes with the same x:y ratio) are near vent samples taken by *Isis*. The relationship Mn/Fe:V/Fe (Figures 6.3 and 6.5) is shown as a dotted black line.

possible to perform Principle Component Analysis (PCA) to elucidate the different phases in a system (Feely et al., 1996), but not enough data was gathered here to conduct such analyses.

Unlike plumes from fast spreading Pacific sites (Feely et al., 1996, 1994a, 1991) or ultramafic (Fe dominated) vent sites (Edmonds and German, 2004; German et al., 2010; Marbler et al., 2010), the vents sampled had smaller outputs of hydrothermal particulate material and the plumes were accordingly smaller in volume with lower Fe concentrations. The total Fe concentrations in the rising and dispersive plume were lowered by high sulfide concentrations at these vents sites - particularly at E9N. Slow and intermediate spreading ridges can host geographically isolated vent sites with plumes that are small compared with those on fast spreading ridges, which host a greater density of vents (Baker, 2007). The ESR hosts an unusually low abundance of venting, possibly due to the distance of most of the spreading axis from the subduction arc (Baker et al., 2005), and so the E2, E9N and E9S sites are particularly isolated. Due to the greater length of slow (< 40 mm yr^{-1}) spreading ridges, the impact that different spreading types have on global heat fluxes

is similar, with slow, intermediate and fast spreading ridges (<40, 40-80, >80 mm yr^{-1}) representing roughly equal proportions of global heat flux (Baker, 2007; Baker and German, 2004). Assuming that the generation of hydrothermal Fe particles is related to heat flux (at least approximately), small, isolated plumes from slow and intermediate ridge vent sites should have a similar global impact of Fe budgets to large plumes from fast spreading centres, although the faster ridges will have a more noticeable localised effect on oceanic and sedimentary Fe budgets (Boström et al., 1969; Feely et al., 1996; Tagliabue et al., 2010). If isolated vent fields like those on the ESR are rich in H_2S or otherwise have unusual chemistry pertaining to Fe speciation, the hydrothermally derived particulate Fe from that portion of ridge crest (and the resulting hydrothermal sediments for that part of the ridge crest) is less likely to conform to generalised behaviour of plume particulates. This is particularly the case if the models are constructed based on data from plumes which average the material of several vent sites, on faster spreading ridges.

It has been considered that the dependence of P:Fe in hydrothermal oxy-hydroxides on dissolved phosphate concentrations could be used as a palaeo proxy for past phosphate concentrations after analysis of hydrothermal sediments (Feely et al., 1998; Sands et al., 2012). Our results from E2 and E9N suggest that prior knowledge of the type of venting (e.g. Fe:H_2S ratio) may be necessary for such a proxy to be used in hydrothermal sediments. Island arc sites such as the Kemp Caldera (this study) and NW-Rota-1 (Resing et al., 2007) also have different (higher) P:Fe ratios, so the proxy could only apply to certain (mid-ocean ridge spreading centre) regions. A large portion of global Fe sediments do come from fast spreading mid-ocean ridge axes (Boström et al., 1969; German and Von Damm, 2004), so with due care, this proxy may be applied - but only where anoxic diagenesis has not led to dissolution of sedimentary P (Poulton and Canfield, 2006; Schaller et al., 2000).

The inclusion of Fe sulfide phases into the hydrothermal plumes may explain the low V:Fe ratios obtained in this study, but P:Fe should be decreased for the same reason. Very acidic environments may allow the dissolution of aluminium from host rocks and lead to the precipitation of P containing woodhouseite minerals (Resing

et al., 2007), but this process is not expected for the (less acidic) East Scotia Ridge plumes, where P:Fe was also found to vary from one year to the next (Figure 6.2). It is possible that in highly sulfidic environments, such as the E9N site and the Kemp Caldera (Chapter 2, 5), a different, more gradual mechanism for the precipitation of Fe oxy-hydroxides via a lower concentration of oxidised colloidal particles may lead to a greater inclusion of P (and V, As) due to the increased surface area and adsorption time available during slow oxidation. The fluxes of other dissolved elements (REEs, dissolved organic carbon) into particles should also be considered in hydrothermal plumes and sediments, and greater surface areas may also lead to greater incorporation of these species.

Chapter 7

Conclusions and future work

7.1 General discussion of the thesis

This thesis has considered the speciation of iron (Fe) in three hydrothermal vent environments, and I have combined several analytical approaches in order to make a wide-ranging examination of the possible fate and biogeochemical importance of hydrothermal Fe to the marine environment. I have further catagorised the hydrothermal Fe pool based on speciation, size and reactivity, allowing some assessment of how much Fe may escape precipitation and settling on the ridge axis and at island arcs, and in what form this Fe may be. Other vent sites may be investigated using the same experimental approaches, and this would allow a much better assessment of the global importance and variation in hydrothermal Fe stabilisation. A summary/schematic of the Fe pools investigated is shown in Figure 7.1. The different pools of Fe present in a given vent site reflect the fluid chemistry and the chemistry of the ambient seawater. In fluids where the molar ratio of H_2S to Fe is low (Figure 2.4), less than 65% of Fe will be present as sulfides (see German et al., 2010, Mottl and McConachy, 1990 and Field and Sherrell, 2000), allowing more Fe to be oxidised and aggregate as inorganic and organic colloids. In this thesis I found measureable amounts of both Fe colloids and labile Fe complexes (which I infered to be colloidal or aggregate in nature) but the relationship between these pools remains to be clarified (Figure 7.1, blue arrow).

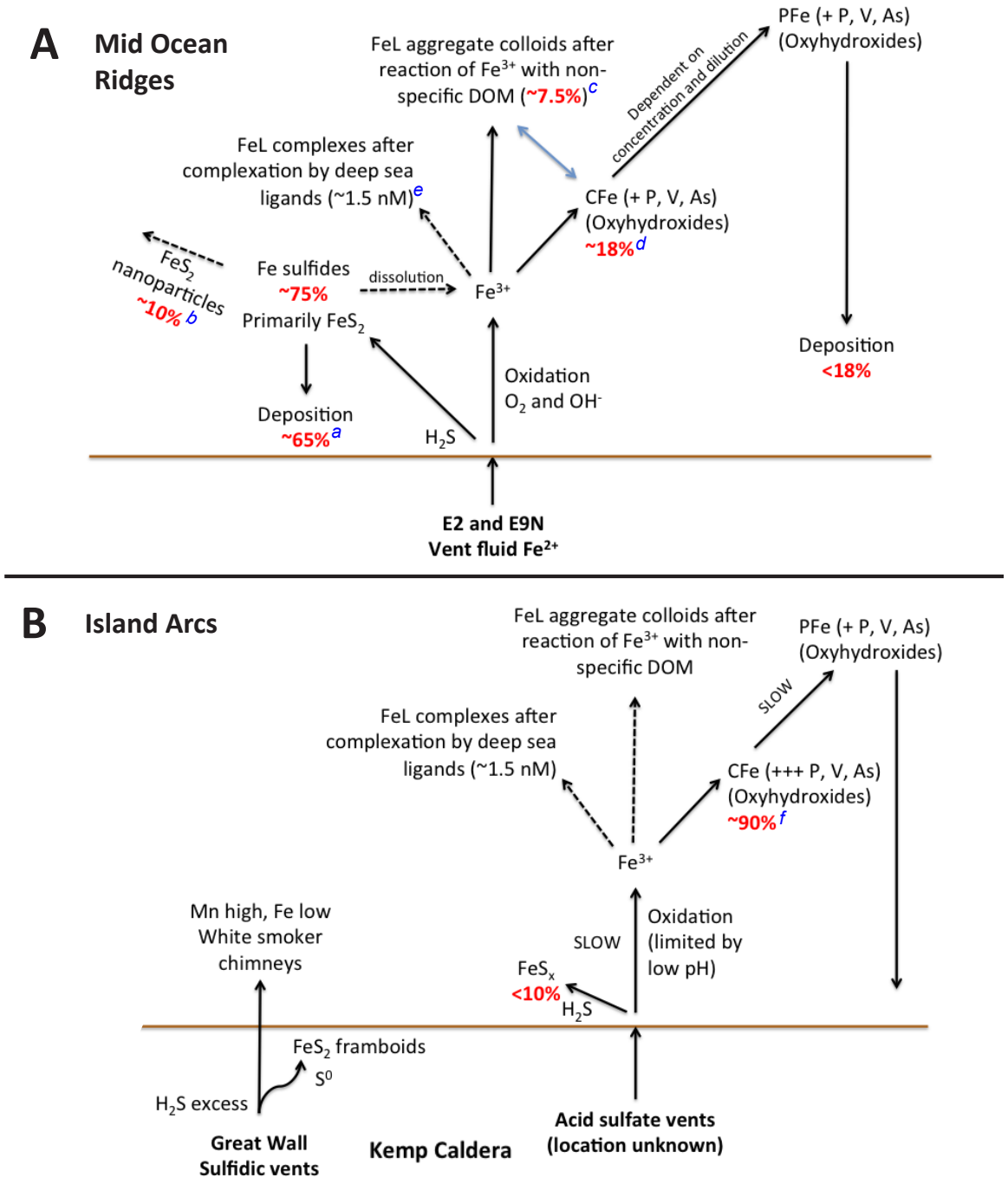

Figure 7.1: Schematic showing the fate of hydrothermal Fe in the environments studied. Percentages in red are based on previous reports or results obtained in this work (see references below). Processes with dotted lines are inferred from previous results but were not measured/investigated in this work. The blue arrow indicates an unknown relationship between two pools of Fe. A: E2 and E9N, B: Kemp Caldera. See next page for reference explanations (blue letters).

The references in Figure 7.1 are as follows: a: Mottl and McConachy (1990). The (highly variable) ratio of H_2S to Fe controls the amount of Fe precipitation as sulfides (Klevenz et al., 2011), and exerts the principle control on the other forms of Fe. b: Yücel et al. (2011). A value of 10% hydrothermal Fe in nano-pyrite was found in two varying vent environments, and this value may be globally consistent, but needs further constraint. c-d: Hawkes et al. (2013a) (Chapter 4). At E2 and E9N, a value of 7.5% was obtained. The remaining Fe (after sulfide precipitation) is presumed to form oxyhydroxide colloids and particles. The relationship between the labile and colloidal Fe is unknown. I assume here that sulfide precipitation is faster than these aggregation processes and limits colloid and labile-Fe complex formation. e: Kondo et al. (2012). Chemically available Fe will also bind with deep ocean ligands, given time. These ligands are apparently widely distributed at similar concentrations in different ocean basins (Gledhill and Buck, 2012). f: Butterfield et al. (2011). H_2S is low in island arc vent sites, limiting pyrite formation and allowing the oxidation of Fe to colloidal phases. This value is a rough guess as we did not sample the near vent environment for these inferred vents in the Kemp Caldera. The colloidal budget in island arc environments should be universally higher than at mid-ocean ridges.

Along with differences in vent fluid composition, the biggest factor in determining the products of hydrothermal venting in seawater is the rate of Fe(II) oxidation. This controls the capacity for absorption of surface reactive seawater constituents and plays an important role in the balance between colloidal and particulate sized Fe(III) particles in the distal plume. In more acidic or more oxygen limited environments, Fe(II) oxidation is slower and surface absorption appears to be increased due to a higher colloidal budget. Magmatically influenced island arc hydrothermal vents like those in the Kemp Caldera are important ifor understanding this effect, because the acid rich fluids allow very long Fe(II) oxidation rates. This style of venting may contribute around 9% of worldwide venting, so differences in the chemistry - including the provision of more stable DFe to the oceans as colloids - are an important consideration in calculating global hydrothermal influence on seawater.

7.2 Outline of possible future work

During the development of this work several interesting ideas have been developed which merit further investigation. The analysis of Fe speciation in seawater by competitive ligand exchange and cathodic stripping voltammetry is not new, but as different environments are investigated, new and innovative approaches need to be developed to fully explore the speciation of such a variable and important element. In conversations with Fe speciation experts and correspondence with anonymous reviewers regarding the reverse titration approach outlined in Chapter 3 and used in Chapter 4, it has become clear that further investigation of the kinetic and thermodynamic constraints on Fe speciation in the laboratory and in-situ in natural environments would be most useful. The investigation of RT-CLE-ACSV with other competitive ligands such as 2,3-dihydroxynaphthalene (DHN; van den Berg, 2006) and salicylaldoxime (SA; Rue and Bruland, 1995) would be interesting, as would kinetic experiments at different competitive ligand concentrations (Gerringa et al., 2007; Witter et al., 2000; Wu and Luther, 1995). In-situ voltammetry and concentration analysis may also be very important tools for future research.

The speciation of Fe was investigated in two 'typical' hydrothermal plumes (Chapter 4) - but to fully understand and resolve hydrothermal Fe inputs into deep ocean environments, other more extreme hydrothermal settings must also be investigated. For example, ultramafic hosted vent sites such as Rainbow, Mid-Atlantic Ridge can have Fe:H_2S ratios as high as 24 (Douville et al., 2002) allowing a much greater flux of Fe away from the vent site. Conversely, some vent sites have such high H_2S that all Fe appears to be incorporated into fragments and assemblages of pyrite - such as the Kemp Caldera vent site discussed in Chapter 5. Therefore, simply multiplying the global hydrothermal water flux by a nominal % stabilised Fe is likely to cause systematic regional errors in any attempts to model hydrothermal inputs of Fe. The south-eastern Pacific has the highest incidence of venting in the world due to fast tectonic spreading rates, leading to enormous output of Fe rich fluids (Feely et al., 1996), and these regions should be investigated with high priority when considering the distribution of dissolved Fe from global hydrothermal sources (Tagliabue et al.,

2010). Generally speaking going forward, hydrothermal outputs from slow and fast spreading rates should be given equal attention for important flux measurements, due to their apparent equal importance in heat (and possibly mass) fluxes (Baker, 2007).

Island arc calderas are often more shallow than mid-ocean ridge or back-arc basin vent sites, and as such may have an important and direct influence on primary productivity (Chapter 5). It would be fascinating to investigate Fe speciation in shallow, acidic hydrothermal environments alongside measurements of primary productivity in order to directly assess whether hydrothermal venting can truly fertilise surface waters. Additionally, it appears that co-precipitation of dissolved seawater constituents such as phosphate may be increased in these environments, possibly due to the slower oxidation of Fe as a result of the increased acidity of the plume water (Chapter 6). This effect could be further investigated (for example in laboratory Fe oxy-hydroxide precipitation experiments) and quantified, and considerations of marine dissolved residence times of several elements may be re-considered (Elderfield and Schultz, 1996; Wheat et al., 1996).

Appendix A

Calculation of $\alpha_{\mathrm{Fe}'}$

$\alpha_{Fe'}$ is the ratio of all inorganic Fe(III) species to free Fe^{3+} (Equation (A.1).

$$\alpha_{Fe'} = \frac{[Fe^{3+}] + \sum [Fe(X)_n]^i}{[Fe^{3+}]} \tag{A.1}$$

Where $[Fe(X)_n]^i = [Fe(OH)]^{2+}$, $[Fe(OH)_2]^+$, $Fe(OH)_3$, $[Fe(OH)_4]^-$, $[FeF]^{2+}$, $[FeF_2]^+$, FeF_3, $[FeCl]^{2+}$, $[FeCl_2]^+$, $[Fe(SO_4)]^+$, $[Fe(SO_4)_2]^-$ and $[Fe(CO_3)]^+$.

Each species is in equilibrium with free iron (Fe^{3+}) as described by an expression of the following form (first hydrolysis product shown):

$$[Fe^{3+}] + H_2O \xrightarrow{K'_{Fe(OH)^{2+}}} Fe(OH)^{2+} + H^+ \tag{A.2}$$

Where

$$K'_{Fe(OH)^{2+}} = \frac{[Fe(OH)^{2+}][H^+]}{[Fe^{3+}][H_2O]} \tag{A.3}$$

Cancelling water (the solvent) and rearranging,

$$\alpha_{Fe(OH)^{2+}} = \frac{[Fe(OH)^{2+}]}{[Fe^{3+}]} = \frac{K'_{Fe(OH)^{2+}}}{[H^+]} \tag{A.4}$$

Equilibrium constants (K) are available from the literature for these iron species (Byrne and Kester, 1976; Byrne et al., 2005; Millero and Pierrot, 2007), and the hydrolysis values can be adjusted to account for the ionic strength of the solution (K'; Millero and Pierrot, 2007). At pH 7.90 (measured on the total scale), temperature 22.5℃, ionic strength 0.71 m and average seawater composition of ions (Cl^- etc.), I calculate values as in Table A.1.

The hydrolysis products alone make up >99.99% of species at laboratory temperature and experimental pH. From this data I use $\alpha_{Fe'} = 6.33 \times 10^9$ (or $10^{9.80}$) in this thesis.

Table A.1: Equilibrium constants and α coefficients for individual inorganic iron species in seawater at laboratory/experimental conditions for RT-CLE-ACSV

Complex	logK	logK′	$\alpha_{[Fe(X)_n]^i}$	% species (<0.01% if not stated)
Fe^{3+}	0.00		1.0	
$[Fe(OH)]^{2+}$	-2.18	-3.23	4.63 x 10^4	
$[Fe(OH)_2]^+$	-6.90	-6.09	5.18 x 10^9	67.2
$Fe(OH)_3$	-13.0	-15.1	3.70 x 10^8	8.10
$[Fe(OH)_4]^-$	-22.3	-22.7	7.85 x 10^8	24.7
$[FeF]^{2+}$	5.18		3.34	
$[FeF_2]^+$	9.11		0.61	
FeF_3	11.9		8.81 x 10^{-3}	
$[FeCl]^{2+}$	1.26		9.93	
$[FeCl_2]^+$	2.53		1.01 x 10^2	
$[Fe(SO_4)]^+$	2.21		4.55	
$[Fe(SO_4)_2]^-$	3.17		1.19	
$[Fe(CO_3)]^+$	9.72		2.36 x 10^5	
		$\alpha_{Fe'}$	6.33 x 10^9	
		$Log(\alpha_{Fe'})$	9.80	

Appendix B

The RT-CLE-ACSV data fitting model in R

Data generated with the RT-CLE-ACSV technique had to be fitted by non-linear regression, and for this a code was written for the statistical analysis software R. Firstly, all peak currents (i_p) were normalised to the maximum obtained value in the same titration (i_p/i_{pmax} = X) and these data were imported alongside the corresponding $\alpha_{Fe(NN)_3}$ (=$\beta_{Fe(NN)_3}$ x $[NN]^3$), the calculated concentration of Fe_{NNmax} and $\alpha_{Fe'}$

- *The Langmuir Isotherm* Here, the data is fitted to the Langmuir Isotherm (Equation 3.7)

- *Non-linear fit for one saturating ligand* Here, the data is fitted to Equation 3.8 where j = 1, i.e. the ligands are equal to or greater than Fe_{NNmax} in concentration. As $[Fe^{3+}]$ can be calculated from K'_{FeL}, [L], $[Fe_{NNmax}]$, $\alpha_{Fe(NN)_3}$ and $\alpha_{Fe'}$ (Equation 3.10), the model only has to fit K'_{FeL} and often a factor which scales the data in cases where i_{pmax} has not been reached.

- *Non-linear fit for one unsaturating ligand* Here j <1 (Equation 3.11). The parameter j is evaluated as $[L]/Fe_{NNmax}$.

- *Non-linear fit for two unsaturating ligands* This fit is the most demanding on the model, as a new unknown parameter is added (K'_{FeL_2}) and the polynomial function to solve $[Fe^{3+}]$ is a cubic formula. $[L_2]$ is made to be equal to $[Fe_{NNmax}]$, as this extra parameter can rarely be solved with only 12 data points. Generally speaking, two ligand classes are unlikely to be sufficiently different within the applied detection window to be successfully resolved with NN.

The non-linear fits are assessed with a given set of parameters for the data scaling (i.e. if i_{pmax} is not reached), [L] and K'_{FeL}. These are usually set to 1, Fe_{NNmax} and a low value such as $1x10^{19}$, respectively. The model modifies these parameters within a small range to the best solution it can using least squares analysis, and then increases the starting value of K'_{FeL}. This is necessary because the range of possible values of K'_{FeL} cover too big a range to be evaluated by the model. The model keeps trying to make a better fit than the last result as the starting K'_{FeL}

increases (i.e. smaller sum of squares of the difference between the data and the fit) and proceeds until the next result is worse than the current fit. This approach leaves the possibility that too low a value of K'_{FeL} will be used when the model finishes (i.e. if there are two solution 'wells' which give good fits) but in these cases the plausibility of the result in comparison to similar samples can be considered. Additionally, a higher value of K'_{FeL} can be set for the starting parameter to see if another reasonable result is obtained. An example output of the model is shown in Figure B.1.

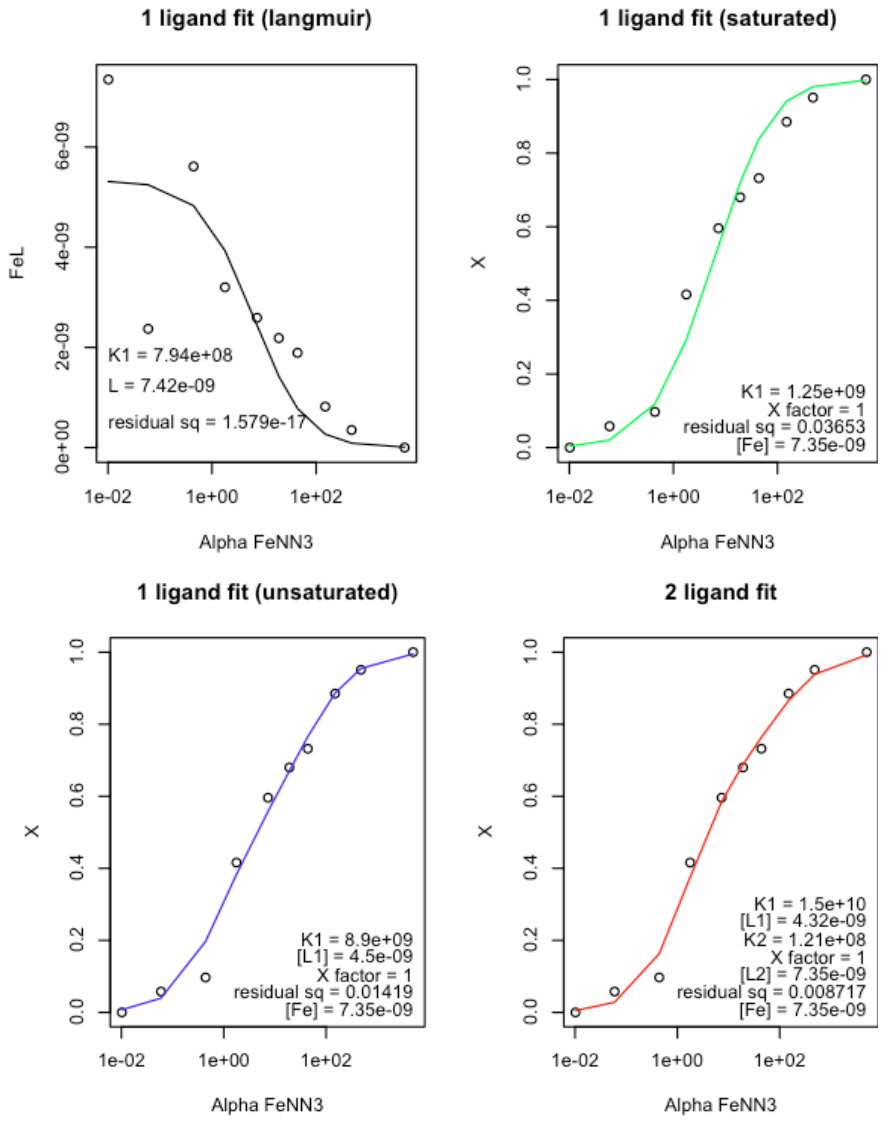

Figure B.1: Example output from the R model. Here, the Langmuir isotherm fit is badly affected by the outlying data point, the 1 ligand (saturated) fit is too steep, the unsaturated ligand fit describes the data well and the two ligand fit is probably unnecessarily complicated. Note that the values for K'_{FeL} reported on the output graphs are lowered by 10 orders of magnitude for easier mathematical manipulation - this applies to all values such as $\alpha_{Fe'}$ which is used as 0.633 instead of $10^{9.80}$.

Appendix C

RT-CLE-ACSV data

		UV treated	
[NN] µM	Log[α_{FeNN3}]	peak	X
0.32	7.22	3.22	0.00
0.98	8.69	5.46	0.09
1.64	9.35	12.28	0.38
2.55	9.93	15.95	0.53
3.59	10.37	20.64	0.73
5.24	10.87	23.45	0.85
8.20	11.45	26.58	0.98
19.64	12.59	27.05	1.00
32.80	13.26	28.36	1.05
48.47	13.77	27.06	1.00

		Saturated FoB	
[NN] µM	Log[α_{FeNN3}]	peak	X
1.00	8.77	3.72	0.00
1.59	9.35	4.05	0.02
2.50	9.93	4.80	0.06
3.32	10.37	4.82	0.06
4.98	10.87	5.47	0.09
6.95	11.28	6.18	0.13
9.57	11.69	7.45	0.19
13.29	12.18	9.77	0.31
18.58	12.59	13.50	0.50
25.17	12.97	17.15	0.68
39.60	13.54	23.36	1.00

		10 nM FoB	
[NN] µM	Log[α_{FeNN3}]	peak	X
0.58	8.00	1.11	0.00
1.00	8.70	6.89	0.14
1.05	8.77	2.56	0.08
1.59	9.31	7.19	0.15
2.03	9.63	5.99	0.27
2.50	9.90	11.14	0.31
3.26	10.25	7.50	0.34
3.32	10.27	13.69	0.41
4.91	10.78	10.85	0.50
4.98	10.80	15.75	0.49
6.89	11.22	11.30	0.55
6.95	11.24	17.07	0.54
9.51	11.64	11.10	0.51
9.57	11.65	17.90	0.57
13.02	12.05	12.40	0.56
13.29	12.08	19.41	0.63
18.32	12.50	14.15	0.65
18.58	12.52	21.86	0.72
24.91	12.90	14.90	0.76
25.17	12.91	23.88	0.80
35.42	13.36	14.10	0.73

		15 nM FoB	
[NN] µM	Log[α_{FeNN3}]	peak	X
0.58	8.00	0.95	0.00
1.05	8.77	1.93	0.11
2.03	9.63	4.41	0.30
3.26	10.25	4.37	0.28
4.91	10.78	5.58	0.38
6.89	11.22	5.49	0.37
9.51	11.64	6.44	0.44
13.02	12.05	7.65	0.55
18.32	12.50	8.55	0.61
24.91	12.90	10.05	0.74
35.42	13.36	14.80	1.05
52.39	13.87	14.15	1.00

		CTD3 N7		CTD3 N11		CTD3 N6		CTD3 N1		CTD424 N7		CTD10 N11		CTD13 N1		CTD424 N4		CTD15 N1	
[NN] µM	Log[α_{FeNN3}]	peak	X	peak	X	peak	X	peak	X	peak	X	peak	X	peak	X	peak	X	peak	X
0.58	8.01	0.00	0.00	2.69	0.03	0.83	0.00	0.90	0.01	1.62	0.00	3.27	0.00	1.32	0.00	3.15	0.11	1.21	0.00
1.05	8.77	1.33	0.04	1.31	0.00	1.03	0.05	0.53	0.00	2.14	0.02	1.32	0.00	2.70	0.06	2.10	0.06	0.68	-0.03
2.03	9.63	1.07	0.00	2.00	0.02	1.08	0.06	0.62	0.00	8.24	0.27	2.80	0.16	4.41	0.14	1.31	0.02	2.18	0.06
3.26	10.25	1.36	0.04	2.21	0.02	1.16	0.08	0.84	0.01	14.55	0.53	4.27	0.32	6.11	0.21	0.88	0.00	4.97	0.22
4.91	10.78	2.88	0.28	7.61	0.16	1.75	0.23	2.02	0.05	19.10	0.71	5.89	0.50	10.98	0.43	1.50	0.03	5.61	0.26
6.89	11.22	4.52	0.53	20.97	0.49	2.05	0.30	9.59	0.31	20.30	0.76	6.95	0.62	13.52	0.54	5.84	0.23	8.90	0.46
9.51	11.64	5.42	0.67	18.68	0.44	2.44	0.40	9.64	0.31	20.84	0.78	6.83	0.60	16.40	0.67	11.00	0.47	11.19	0.59
13.02	12.05	6.06	0.77	19.23	0.45	2.98	0.54	14.26	0.47	24.09	0.92	7.34	0.66	16.49	0.67	6.32	0.25	14.37	0.78
18.32	12.50	6.69	0.87	28.34	0.68	3.71	0.72	18.23	0.61	24.24	0.92	8.22	0.76	18.99	0.79	8.01	0.33	14.26	0.77
24.91	12.90	7.78	1.03	31.97	0.77	3.21	0.59	18.50	0.61	26.44	1.01	8.56	0.79	22.61	0.95	14.57	0.63	16.27	0.89
35.42	13.36	7.38	0.97	37.41	0.91	4.22	0.84	27.60	0.93	26.14	1.00	9.55	0.90	23.82	1.00	17.91	0.79	17.63	0.97
52.39	13.87	7.55	1.00	41.12	1.00	4.84	1.00	29.78	1.00	34.45	1.34	10.44	1.00	30.25	1.29	22.51	1.00	18.10	1.00

		CTD15 N7		CTD15 N10		CTD15 N14		CTD424 N14		CTD7 N11(2)	
[NN] µM	Log[α_{FeNN3}]	peak	X	peak	X	peak	X	peak	X	peak	X
0.58	8.01	2.38	0.00	1.22	0.00	1.46	0.00	3.13	0.07	0.75	0.00
1.05	8.77	2.34	0.00	1.95	0.07	2.03	0.04	2.40	0.00	1.71	0.04
2.03	9.63	2.73	0.03	3.04	0.18	3.86	0.17	3.83	0.14	3.84	0.13
3.26	10.25	3.00	0.05	2.81	0.16	3.02	0.11	4.14	0.17	3.09	0.10
4.91	10.78	4.25	0.16	6.29	0.50	3.71	0.16	5.78	0.32	5.16	0.18
6.89	11.22	6.66	0.36	8.56	0.73	7.24	0.42	8.19	0.55	8.82	0.34
9.51	11.64	9.54	0.61	8.42	0.72	9.19	0.56	11.79	0.90	10.42	0.40
13.02	12.05			8.77	0.75	5.61	0.30	7.82	0.52	13.86	0.55
18.32	12.50			8.65	0.74	6.73	0.38	12.86	1.00	13.95	0.55
24.91	12.90			10.20	0.90	9.43	0.58	12.86	1.00	16.99	0.68
35.42	13.36	12.99	0.90	11.47	1.02	12.98	0.83	12.63	0.98	19.26	0.77
52.39	13.87	14.13	1.00	11.25	1.00	15.26	1.00				
78.38	14.39									24.73	1.00

		CTD4N1	
[NN] µM	Log[α_{FeNN3}]	peak	X
0.58	8.01	1.19	0.00
1.05	8.77	3.85	0.06
2.03	9.63	1.19	0.10
3.26	10.25	2.27	0.42
5.24	10.87	2.99	0.60
7.21	11.28	8.93	0.68
9.51	11.64	12.27	0.73
14.35	12.18	13.83	0.89
20.96	12.67	14.79	0.95
45.87	13.69	18.86	1.00

		CTD4 N6		CTD4 N13		CTD7 N17		CTD7 N2		CTD7 N13		CTD7 N11	
[NN] µM	Log[α_{FeNN3}]	peak	X	peak	X	peak	X	peak	X	peak	X	peak	X
0.32	7.22	0.79	0.00					0.53	0.00				
0.58	8.01	0.79	0.00	1.13	0.00	0.59	0.00			0.75	0.00		
1.05	8.77	1.18	0.06	1.16	0.01	0.60	0.00	0.59	0.01	0.87	0.01	1.13	0.00
2.03	9.63	1.53	0.11	1.05	-0.02	0.77	0.03	1.21	0.05	1.06	0.04	0.73	0.01
3.26	10.25	3.49	0.39	1.36	0.06	1.52	0.14	2.23	0.13	0.86	0.01	0.97	0.04
4.91	10.78									1.98	0.15	1.54	0.17
5.24	10.87	5.07	0.62	1.85	0.18	3.47	0.43	4.60	0.31				
6.89	11.22									2.76	0.24	4.00	0.34
7.21	11.28	4.63	0.56	2.94	0.44	3.41	0.42	5.73	0.40				
9.51	11.64	5.35	0.66	2.82	0.41					3.21	0.30	7.21	0.59
11.70	11.91					3.98	0.51	8.29	0.59				
13.02	12.05									5.00	0.52	11.90	0.74
14.35	12.18	7.15	0.92	2.96	0.45								
16.99	12.40					4.79	0.63	10.75	0.78				
18.32	12.50									6.65	0.72	14.64	0.00
20.96	12.67	7.70	1.00	3.61	0.61								
24.91	12.90					5.49	0.73	12.10	0.88	7.28	0.79	10.66	0.65
26.23	12.97	6.90	0.88	4.09	0.72								
35.42	13.36					6.66	0.91	13.32	0.97	8.98	1.00	12.96	0.91
40.65	13.54	11.50	1.55	5.23	1.00								
52.39	13.87					7.29	1.00	13.65	1.00	11.83	1.35	17.91	1.00

		CTD6 N1	
[NN] µM	Log[α_{FeNN3}]	peak	X
0.40	7.51	0.42	0.00
0.58	8.00	0.45	0.01
1.07	8.80	0.45	0.01
2.06	9.65	1.46	0.22
3.39	10.30	2.34	0.40
5.37	10.90	2.93	0.52
7.35	11.31	3.71	0.69
9.80	11.68	4.56	0.86
13.55	12.11	4.55	0.86
19.50	12.58	5.06	0.97
27.41	13.02	5.14	0.98
41.17	13.55	5.22	1.00

Appendix D

Metals and Fe ligand data

E2		Depth	Maximum dilution (based on Mn)	Dissolved Mn nM	Dissolved Fe nM	Dissolved Cu nM	<0.02µm Mn nM	<0.02µm Fe nM	<0.02µm Cu nM	Particulate Mn nM	Particulate Fe nM	Particulate Cu nM	Fe ligand characteristics Fe NNmax nM	L nM	LogK	±
Samples	CTD3 N1	2586	6005	348	36.1	1.25				0.59	108	3.23	17.7	17.7	20.4	0.15
	CTD3 N6	2574	3971	525	83.5	1.14				0.57	146	1.80	3.91	3.91	20.6	0.06
	CTD3 N7	2372	18635	112	20.2	1.21				0.64	153	1.13	1.87	1.87	20.3	0.10
	CTD3 N11	2277	14257	147	30.9	1.77				0.24	19.5	1.61	11.5	11.5	20.2	0.10
	CTD3 N14	998		0.28	1.59	2.52				0.09	7.86	0.06				
	CTD4 N1	2612	7636	273	22.5	1.63				0.23	7.35	1.31	7.39	4.38	20.0	0.33
	CTD4 N6	2506	108899	19.7	9.42	2.43				0.18	4.74	0.16	2.02	2.02	19.8	0.23
	CTD4 N17	2341		0.81	1.43	2.66				0.11	2.08	0.04				
	CTD04 N13	2482	156933	13.8	7.76	2.76				0.16	3.18	0.08	2.03	2.03	21.5	0.11
	CTD04 N23	992		0.18	0.74	2.14										
	CTD5 N1	2567		354	31.6	1.09				1.14	137	2.47				
	CTD6 N17	2258	27604	76.1	16.3	2.05				0.30	6.90	1.41	1.89	1.27	20.4	0.20
	CTD7 N2	2272	37347	56.4	12.1	2.71				0.20	5.70	0.65	4.32	4.32	20.3	0.05
	CTD7 N11	2272	21475	97.6	14.3	3.21				0.22	5.31	0.95	6.60	6.60	20.6	0.16
	CTD7 N13	2272	36100	58.3	18.0	2.27				0.45	6.12	0.94	3.15	3.15	21.0	0.08
	CTD7 N17	2272	28705	73.2	13.1	3.29				0.25	6.59	0.57	2.10	2.10	20.9	0.24
Near field	ISIS133	5x diluted											27.2	27.2	20.5	0.11
		10x diluted											18.8	14.5	21.0	0.18
		20x diluted											13.6	9.27	21.8	0.26
		average	214	9733	637					21.83	1883	2.1	136	136	21.1	
	ISIS134	5x diluted											36.9	36.9	20.3	0.16
		10x diluted											19.1	17	20.4	0.15
		20x diluted											20.7	20.7	20.4	0.09
		average	641	3254	1392					13.13	483	11.9	184.5	184.5	20.3	
	ISIS135	5x diluted											28.3	28.3	20.4	0.13
		10x diluted											17.9	17.9	20.1	0.08
		20x diluted											15.1	15.1	19.8	0.45
		average	2762	755	288					13.49	692	20.6	141.5	141.5	20.1	
Background Station	CTD422 N1	2350		0.96	1.39	2.43	1.12	1.10	3.33	0.13	2.96	-0.03				
	CTD422 N2	2350		0.93	2.59	3.00										
	CTD422 N3	2350		0.30	1.74	2.77										
	CTD422 N13	2000		0.98	2.46	2.60	1.14	2.36	3.93	0.21	7.22	0.01				
	CTD422 N14	2000		0.20	0.94	2.45										
	CTD422 N15	2000		0.40	1.28	2.58										

	E9	Depth	Maximum dilution (based on Mn)	Dissolved Mn nM	Dissolved Fe nM	Dissolved Cu nM	<0.02µm Mn nM	<0.02µm Fe nM	<0.02µm Cu nM	Particulate Mn nM	Particulate Fe nM	Particulate Cu nM	Fe ligand characteristics Fe NNmax nM	L nM	LogK	±
Samples 2010	CTD08	1000		0.40	3.32	2.59										
	CTD10 N11	2115	30862	6.99	21.0	3.14				0.57	4.21	0.19	3.19	2.04	21.8	0.11
	CTD10 N18	1498		0.41	0.68	2.64				0.40	2.57	0.09				
	CTD12	2237	20304	10.3	134	4.59				0.59	25.7	0.26				
	CTD13 N23	2300	11776	17.4	22.0	1.42				4.22	19.9	3.63	8.11	5.68	21.4	0.16
	CTD14 N1	2229		2.98	5.02	2.10				0.76	3.82	0.72				
	CTD14 N4	2305		2.81	6.66	2.31				0.73	3.74	0.30				
	CTD14 N11	2102		1.85	1.55	2.84				0.65	2.97	0.06				
	CTD15 N1	2384	12768	16.1	8.40	1.91				0.52	4.43	1.07	7.13	7.13	19.8	0.08
	CTD15 N7	2344	75688	3.19	7.91	2.30				0.83	5.02	0.63	10.2	10.2	19.9	0.13
	CTD15 N10	2034	39760	5.55	6.32	2.08				0.49	4.75	0.30	5.36	3.03	21.2	0.72
	CTD15 N14	1984	86959	2.85	3.18	2.36				0.45	2.60	0.24				
	CTD15 N18	1934	139069	1.99	2.33	2.96				0.45	2.14	0.05				
	CTD15 N24	1873	290655	1.25	1.72	2.77				1.27	16.31	0.28				
Samples 2011	CTD424 N4	2382	7395	27.3	14.0	4.12	6.45	13.3	3.07	0.25	3.69	0.50	9.85	9.85	21.1	0.02
	CTD424 N7	2385	5777	34.8	23.0	2.80	21.5	8.25	1.81	0.44	3.86	0.36	6.75	3.25	20.7	0.55
	CTD424 N8	2218		0.69	2.61	0.34				0.51	3.92	0.19				
	CTD424 N10	2144	34504	6.31	7.31	2.41	8.77	17.9	6.57	0.40	2.13	0.14				
	CTD424 N14	2146	19670	10.6	10.9	2.47	10.8	4.86	2.42	0.86	5.90	0.60	4.26	4.26	20.7	0.15
	CTD424 N22	1750		0.87	1.73	2.89				0.43	2.08	0.04				
	CTD426 N1	2224	33794	6.43	9.33	2.83	6.47	0.68	1.88							
	CTD426 N2	+1.7 hours	41812	5.31	8.71	2.54	7.50	7.98	2.83							
	CTD426 N3	+3.7 hours	35110	6.21	10.8	2.71	7.57	0.69	5.86							
	CTD426 N13	+1.7 hours	36232	6.03	6.33	2.53	6.81	2.29	2.78	0.14	1.12	0.06				
	CTD426 N16	+11 hours					6.59	2.82	2.94							
	CTD428 N19	2073	42230	5.26	17.9	2.41	6.23	3.24	2.62	1.32	12.3	0.77				
	CTD428 N20	2044	49200	4.59	6.14	0.69	9.16	3.23	2.23	0.91	6.61	0.95				
	CTD428 N21	2016	48705	4.64	5.13	1.20	8.18	3.27	2.07	1.13	7.11	1.03				
	CTD428 N22	1995	39427	5.59	5.13	2.13	6.69	3.81	1.93	1.06	7.87	0.83				
Near Field	ISIS140	5x diluted											51.92	51.92	19.4	0.11
		10x diluted											27.90	18.70	21.5	0.31
		20x diluted											21.90	16.10	20.8	0.11
		average	219	905	1428					95	7389	35.3	260	260	20.6	

Kemp			Dissolved			<0.02µm			Particulate		
		Depth	Mn nM	Fe nM	Cu nM	Mn nM	Fe nM	Cu nM	Mn nM	Fe nM	Cu nM
Samples 2010	CTD101 N1	1418	50.1	16.0	2.47				0.86	6.50	0.34
	CTD101 N11	1414	46.7	16.7	2.67				0.97	11.8	0.28
	CTD101 N17	1297	60.6	17.3	3.09				0.84	10.0	0.34
	CTD102 N1	1349	98.5	23.3	2.15						
	CTD103 N1	1388	84.3	14.8	2.25						
	CTD103 N5	1193	82.0	15.1	2.73						
	CTD103 N13	1055	37.4	13.4	2.59						
	CTD103 N15	955	20.5	7.7	2.53						
	CTD103 N19	697	5.5	3.6	2.53				0.91	16.42	0.19
Samples 2011	CTD430 N1	1391	60.4	17.5	2.08	53.39	6.64	1.56	0.80	4.55	0.40
	CTD430 N13	1177	56.0	18.0	2.47	51.68	1.46	2.06	1.96	12.3	0.72
	CTD432 N9	1401	41.4	12.6	1.70	48.37	1.92	1.50	2.04	10.0	0.45
	CTD432 N12	1396	57.9	11.8	1.18	75.04	5.19	1.11	0.63	6.70	0.67
	CTD432 N19	1391	122.3	17.5	1.91				0.33	8.44	0.83
	CTD432 N22	1365	61.2	14.5	2.36	64.38	0.66	2.77	1.90	14.5	0.25
	CTD433 N1	986	74.2	17.9	2.47	70.27	11.03	1.95	0.87	6.01	0.17
	CTD437 N1	1395	38.7	16.5	2.41				0.87	5.49	0.02
	CTD437 N5	1291	41.2	14.9	3.10				1.84	10.1	0.10
	CTD437 N21	1172	60.6	14.3	2.70				1.36	7.68	0.04
	CTD438 N1	1066	76.6	17.9	2.27	67.46	1.79	0.74	1.39	9.81	0.94
	CTD438 N2	1066							1.64	11.1	1.25
	CTD438 N3	1066							1.13	8.57	0.62
	CTD439 N11	1005	73.4	17.3	3.90	54.56	7.68	1.63			
	CTD439 N14	912	70.4	18.7	2.56						
Near Field	ISIS 147	1422	124	847					0.42	118	0.52
	ISIS 149	1435	332	596					0.38	57.4	28.8
	ISIS 150	1430	289	685					0.45	70.9	36.9
	ISIS 151	1428	273	1066							
	ISIS 152	1425	1104	820					0.28	46.7	11.6
Background	CTD434 N2		6.13	2.79	2.34						
	CTD434 N8		6.94	3.81	2.09						

Appendix E

Particulate phase concentrations

E2	filter amount x seawater filtered	Sample	Al	P	V	Mn	Fe	Co	Cu	Zn	As	Ba
	ml		nM	nM	nM	nM	nM	nM	nM	nM	nM	nM
2010 Samples	1912.5	CTD3, n1		10.30	0.1721	0.23	60.6		1.64	27.1	0.1396	
	1612.5	CTD3, n6		12.66	0.1773	0.49	145		1.82	30.8	0.1266	
	2637.5	CTD3, n7		3.93	0.0436	0.57	152		1.14	6.16	0.0122	
	250	CTD5, n1	6.58	7.15	0.0687	1.06	136	0.0095	2.80	30.4	0.0265	0.40
	3737.5	CTD3, n11		2.94	0.0175	0.16	19.0		1.61	7.97	0.0083	
	3787.5	CTD3, n14		1.09	0.0066	0.02	7.29		0.06	0.46	0.0016	
	5000	CTD4, n2	3.15	0.61	0.0073	0.04	3.11		0.65	5.79	0.0096	
	10000	CTD4, n11	3.31	1.31	0.0104	0.10	4.16		0.15	0.38	0.0035	
	10000	CTD4, n16	2.97	0.55	0.0065	0.08	2.60		0.07	0.19	0.0018	
	10000	CTD4, n18	2.15	0.73	0.0031	0.04	1.50		0.03	0.13	0.0003	
	5000	CTD6, n24		1.24	0.0135	0.22	6.33		1.40	3.47	0.0042	
	5000	CTD7, n3	6.51	0.95	0.0123	0.13	5.13		0.64	1.75	0.0035	
	5000	CTD7, n12	4.96	1.39	0.0120	0.15	4.75		0.95	3.06	0.0043	
	5000	CTD7, n14	3.64	1.84	0.0144	0.37	5.55		0.94	2.00	0.0055	
	5000	CTD7, n19a	3.27	2.44	0.0094	0.09	5.25		0.46	1.17	0.0023	
SAPS	55500	E2 1	2.32	0.20	0.0038	0.01	2.37		0.02	0.26	0.0001	
	287750	E2 2	2.57	0.12	0.0038	0.01	1.58		0.01	0.08	0.0002	
	428250	E2 3	2.53	0.06	0.0039	0.02	1.46		0.03	0.04	0.0001	
	437000	E2 4	2.58		0.0039	0.00	1.02		0.01	0.03	0.0000	
	28250	CTD5	5.26	0.83	0.0120	0.29	5.13		0.18	1.10	0.0033	
	15500	CTD6	4.89	0.24	0.0217	0.65	16.54		0.97	1.77	0.0098	
	43500	CTD7	6.16	0.56	0.0142	0.23	5.93		0.34	1.07	0.0036	
Near vent	300	ISIS 132 R/G		3.53		2.77	68.3		5.14	190	0.0673	1.05
	187.5	ISIS 132 W		6.87	0.1382	13.0	1242		231.33	1150	1.7549	1.06
	112.5	ISIS 133		323.80		4.45	388		2.07	64.7	1.0276	20.3
	1450	ISIS 134		23.35	0.0005	2.38	89.5		11.89	91.1	0.4311	1.69
	950	ISIS 135		15.63		2.33	122		20.63	161	0.3915	1.61
		Background		0.31	0.0018	0.07	0.59	0.0003	0.02	0.00	0.0004	0.07

E9	filter amount x seawater filtered	Sample	Al	P	V	Mn	Fe	Co	Cu	Zn	As	Ba
	ml		nM	nM	nM	nM	nM	nM	nM	nM	nM	nM
2010 Samples	5000	CTD10, n12	6.48	1.52	0.0130	0.73	4.32		0.28	0.32	0.0017	
	10000	CTD10, n13	1.90	4.88	0.0093	0.26	2.95		0.09	0.28	0.0026	
	5000	CTD 13, n1	4.19	1.79	0.0171	0.63	14.1	0.0101	3.87	3.71	0.0107	0.28
	5000	CTD 14, n2	4.28	1.01	0.0095	0.69	3.39	0.0015	0.77	0.41	0.0015	0.21
	5000	CTD 14, n3	4.33	0.77	0.0092	0.69	3.12	0.0016	0.68	0.20	0.0003	0.20
	5000	CTD 14, n5	4.55	0.87	0.0105	0.66	3.17	0.0013	0.30	0.09	0.0015	0.19
	5000	CTD 14, n12	3.77	1.26	0.0086	0.58	2.40	0.0011	0.06	0.28	0.0001	0.18
	5000	CTD 15, n2	2.37	0.77	0.0098	0.22	2.15	0.0004	0.56	0.26	0.0064	0.14
	5000	CTD15, n2		1.60	0.0271	0.67	5.58	0.0016	1.59	0.63	0.0157	0.37
	5000	CTD 15, n8	4.61	1.28	0.0120	0.77	4.13	0.0021	0.64	0.21	0.0042	0.23
	5000	CTD15, n8		1.11	0.0133	0.74	4.77	0.0022	0.63	0.60	0.0055	0.22
	5000	CTD15, n12		0.70	0.0097	0.42	4.18	0.0014	0.30	0.65	0.0013	0.12
	5000	CTD15, n15		0.56	0.0038	0.37	2.03	0.0008	0.24	0.18		0.11
	5000	CTD15, n19		0.59	0.0038	0.38	1.58	0.0006	0.05	0.25		0.08
	1350	CTD15, n24		2.51	0.0356	1.20	15.8	0.0053	0.33	0.21	0.0005	0.73
SAPS	32000	CTD12	3.12	0.39	0.0103	0.49	4.34		0.19	0.48	0.0020	
	30750	CTD14	6.33	1.07	0.0128	0.73	5.76		0.23	0.93	0.0038	
Near vent	1050	ISIS 140		74.0	2.5503	16.2	1260	0.3095	35.3	41.7	0.8907	0.98
	825	ISIS 142		38.2	0.3706	6.91	527	0.0807	112	102	0.3257	1.57
	1075	ISIS 144		29.3	0.7582	14.0	414	0.0816	8.43	15.7	0.1816	2.76
2011 Samples	5000	CTD 424, n4		0.63	0.0017	0.12	2.22		0.35	0.66		0.00
	5000	CTD 424, n6	4.19	1.48	0.0088	0.36	3.15		0.32		0.0039	0.11
	5000	CTD 424, n9	1.83	0.94	0.0088	0.42	3.15		0.13		0.0010	0.11
	5000	CTD 424, n11		0.73	0.0048	0.32	1.43		0.10			0.06
	5000	CTD 424, n19	3.48	2.22	0.0134	0.77	5.12		0.54	0.27	0.0020	0.22
	5000	CTD 424, n23		0.60	0.0040	0.35	1.37			0.07		0.10
	550	CTD 428, n19	4.15	6.82	0.0145	1.14	9.91		0.33	1.65		0.43
	600	CTD 428, n20	1.49	0.14	0.0073	0.74	4.39		0.54			0.73
	500	CTD 428, n21	2.40		0.0068	0.94	4.56		0.55			0.36
	600	CTD 428, n22	2.66	3.62	0.0151	0.89	5.66		0.43			0.34
	5000	CTD 428, n23	1.03	1.07	0.0036	0.33	1.27		0.18	0.00	0.0005	0.09
		CTD 426										
	5000	+ 10 hours	5.24	2.30	0.0197	1.16	6.67		0.42	1.27	0.0060	0.35
	5000	+ 12.5 hours	207	1.87	0.0134	0.76	4.15		0.24		0.0020	0.18
	5000	+ 16 hours	2.48	2.27	0.0108	0.59	3.87		0.15		0.0002	0.09
	5000	+ 17.5 hours		3.33	0.0135	0.73	3.84		0.23	0.18	0.0051	0.20
	5000	+ 19 hours		3.09	0.0115	0.68	3.67		0.20		0.0012	0.16
	5000	+ 21 hours		2.37	0.0121	0.71	3.71		0.17		0.0019	0.10
	5000	+ 1.5 hours	59.3	2.10	0.0081	0.48	3.12		0.22	1.39	0.0024	0.10
	5000	+ 1.5 hours		0.73	0.0008	0.05	0.34			0.26	0.0004	
		Background		0.31	0.0018	0.07	0.59	0.0003	0.02	0.00	0.0004	0.07

E2	filter amount x seawater filtered	Sample	Al	P	V	Mn	Fe	Co	Cu	Zn	As	Ba
	ml		nM	nM	nM	nM	nM	nM	nM	nM	nM	nM
2010 Samples	1912.5	CTD3, n1		10.30	0.1721	0.23	60.6		1.64	27.1	0.1396	
	1612.5	CTD3, n6		12.66	0.1773	0.49	145		1.82	30.8	0.1266	
	2637.5	CTD3, n7		3.93	0.0436	0.57	152		1.14	6.16	0.0122	
	250	CTD5, n1	6.58	7.15	0.0687	1.06	136	0.0095	2.80	30.4	0.0265	0.40
	3737.5	CTD3, n11		2.94	0.0175	0.16	19.0		1.61	7.97	0.0083	
	3787.5	CTD3, n14		1.09	0.0066	0.02	7.29		0.06	0.46	0.0016	
	5000	CTD4, n2	3.15	0.61	0.0073	0.04	3.11		0.65	5.79	0.0096	
	10000	CTD4, n11	3.31	1.31	0.0104	0.10	4.16		0.15	0.38	0.0035	
	10000	CTD4, n16	2.97	0.55	0.0065	0.08	2.60		0.07	0.19	0.0018	
	10000	CTD4, n18	2.15	0.73	0.0031	0.04	1.50		0.03	0.13	0.0003	
	5000	CTD6, n24		1.24	0.0135	0.22	6.33		1.40	3.47	0.0042	
	5000	CTD7, n3	6.51	0.95	0.0123	0.13	5.13		0.64	1.75	0.0035	
	5000	CTD7, n12	4.96	1.39	0.0120	0.15	4.75		0.95	3.06	0.0043	
	5000	CTD7, n14	3.64	1.84	0.0144	0.37	5.55		0.94	2.00	0.0055	
	5000	CTD7, n19a	3.27	2.44	0.0094	0.09	5.25		0.46	1.17	0.0023	
SAPS	55500	E2 1	2.32	0.20	0.0038	0.01	2.37		0.02	0.26	0.0001	
	287750	E2 2	2.57	0.12	0.0038	0.01	1.58		0.01	0.08	0.0002	
	428250	E2 3	2.53	0.06	0.0039	0.02	1.46		0.03	0.04	0.0001	
	437000	E2 4	2.58		0.0039	0.00	1.02		0.01	0.03	0.0000	
	28250	CTD5	5.26	0.83	0.0120	0.29	5.13		0.18	1.10	0.0033	
	15500	CTD6	4.89	0.24	0.0217	0.65	16.54		0.97	1.77	0.0098	
	43500	CTD7	6.16	0.56	0.0142	0.23	5.93		0.34	1.07	0.0036	
Near vent	300	ISIS 132 R/G		3.53		2.77	68.3		5.14	190	0.0673	1.05
	187.5	ISIS 132 W		6.87	0.1382	13.0	1242		231.33	1150	1.7549	1.06
	112.5	ISIS 133		323.80		4.45	388		2.07	64.7	1.0276	20.3
	1450	ISIS 134		23.35	0.0005	2.38	89.5		11.89	91.1	0.4311	1.69
	950	ISIS 135		15.63		2.33	122		20.63	161	0.3915	1.61
		Background		0.31	0.0018	0.07	0.59	0.0003	0.02	0.00	0.0004	0.07

Bibliography

Achterberg, E. P., Braungardt, C. B., Sandford, R. C. and Worsfold, P. J. 'UV digestion of seawater samples prior to the determination of copper using flow injection with chemiluminescence detection'. *Analytica Chimica Acta* (2001). **440**(1) pp. 27–36.

Al-Farawati, R. and van den Berg, C. M. 'Metal–sulfide complexation in seawater'. *Marine Chemistry* (1999). **63**(3) pp. 331–352.

Aldrich, A. P. and van den Berg, C. M. G. 'Determination of iron and its redox speciation in seawater using catalytic cathodic stripping voltammetry'. *Electroanalysis* (1998). **10**(6) pp. 369–373.

Alt, J. C. 'Subseafloor processes in mid-ocean ridge hydrothennal systems'. *Geophysical Monograph Series* (1995). **91** pp. 85–114.

Aluwihare, L. and Repeta, D. 'A comparison of the chemical characteristics of oceanic DOM and extracellular DOM produced by marine algae'. *Marine Ecology-Progress Series* (1999). **186** pp. 105–117.

Andreae, M. O. 'Arsenic speciation in seawater and interstitial waters: the influence of biological-chemical interactions on the chemistry of a trace element'. *Limnology and Oceanography* (1979). **24**(3).

Anschutz, A. J. and Penn, R. L. 'Reduction of crystalline iron III oxyhydroxides using hydroquinone: Influence of phase and particle size'. *Geochemical Transactions* (2005). **6**(3) pp. 60–66.

Baker, E., Massoth, G., Walker, S. and Embley, R. 'A Method For Quantitatively Estimating Diffuse And Discrete Hydrothermal Discharge'. *Earth and Planetary Science Letters* (1993). **118**(1-4) pp. 235–249.

Baker, E. T. 'Hydrothermal cooling of midocean ridge axes: Do measured and modeled heat fluxes agree?' *Earth and Planetary Science Letters* (2007). **263**(1) pp. 140–150.

Baker, E. T., Embley, R. W., Walker, S. L., Resing, J. A., Lupton, J. E., Nakamura, K.-I., de Ronde, C. E. J. and Massoth, G. J. 'Hydrothermal activity and volcano distribution along the Mariana arc'. *Journal of Geophysical Research-Solid Earth* (2008). **113**(B8).

Baker, E. T. and German, C. R. 'On the global distribution of hydrothermal vent fields'. *Mid-Ocean Ridges: Hydrothermal Interactions Between the Lithosphere and Oceans, Geophysics Monograph Series* (2004). **148** pp. 245–266.

Baker, E. T. and Massoth, G. J. 'Characteristics of hydrothermal plumes from 2 vent fields on the Juan-de-Fuca Ridge, Northeast Pacific Ocean'. *Earth and Planetary Science Letters* (1987). **85**(1-3) pp. 59–73.

Baker, E. T., Massoth, G. J., Nakamura, K.-i., Embley, R. W., de Ronde, C. E. and Arculus, R. J. 'Hydrothermal activity on near-arc sections of back-arc ridges: Results from the Mariana Trough and Lau Basin'. *Geochemistry Geophysics Geosystems* (2005). **6**(9) p. Q09,001.

Baker, E. T., Walker, S. L., Embley, R. W. and de Ronde, C. E. J. 'High-Resolution Hydrothermal Mapping of Brothers Caldera, Kermadec Arc'. *Economic Geology* (2012). **107**(8, SI) pp. 1583–1593.

Bennett, S. A., Achterberg, E. P., Connelly, D. P., Statham, P. J., Fones, G. R. and German, C. R. 'The distribution and stabilisation of dissolved Fe in deep-sea hydrothermal plumes'. *Earth and Planetary Science Letters* (2008). **270** p. 157.

Bennett, S. A., Coleman, M., Huber, J. A., Reddington, E., Kinsey, J. C., McIntyre, C., Seewald, J. S. and German, C. R. 'Trophic regions of a hydrothermal plume dispersing away from an ultramafic-hosted vent-system: Von Damm vent-site, Mid-Cayman Rise'. *Geochemistry, Geophysics, Geosystems* (2013). **14**(2) pp. 317–327.

Bennett, S. A., Statham, P. J., Green, D. R. H., Le Bris, N., McDermott, J. M., Prado, F., Rouxel, O. J., Von Damm, K. and German, C. R. 'Dissolved and particulate organic carbon in hydrothermal plumes from the East Pacific Rise, 9 degrees 50'N'. *Deep-Sea Research Part I-Oceanographic Research Papers* (2011). **58**(9) pp. 922–931.

Benoit, G., Oktaymarshall, S. D., Cantu, A., Hood, E. M., Coleman, C. H., Corapcioglu, M. O. and Santschi, P. H. 'Partitioning of Cu, Pb, Ag, Zn, Fe, Al, and Mn between filter-retained particles, colloids, and solution in 6 Texas estuaries'. *Marine Chemistry* (1994). **45**(4) pp. 307–336.

Bergquist, B. A. and Boyle, E. A. 'Dissolved iron in the tropical and subtropical Atlantic Ocean'. *Global Biogeochemical Cycles* (2006). **20**(1).

Bergquist, B. A., Wu, J. and Boyle, E. A. 'Variability in oceanic dissolved iron is dominated by the colloidal fraction'. *Geochimica et Cosmochimica Acta* (2007). **71**(12) pp. 2960–2974.

Bischoff, J. L. and Rosenbauer, R. J. 'An empirical equation of state for hydrothermal seawater (3.2 percent NaCl)'. *American Journal of Science* (1985). **285**(8) pp. 725–763.

Boström, K., Peterson, M., Joensuu, O. and Fisher, D. E. 'Aluminum-poor ferromanganoan sediments on active oceanic ridges'. *Journal of Geophysical Research* (1969). **74**(12) pp. 3261–3270.

Boyd, P. and Ellwood, M. 'The biogeochemical cycle of iron in the ocean'. *Nature Geoscience* (2010). **3**(10) pp. 675–682.

Boyd, P. W., Jickells, T., Law, C. S., Blain, S., Boyle, E. A., Buesseler, K. O., Coale, K. H., Cullen, J. J., de Baar, H. J. W., Follows, M., Harvey, M., Lancelot, C., Levasseur, M., Owens, N. P. J., Pollard, R., Rivkin, R. B., Sarmiento, J.,

Schoemann, V., Smetacek, V., Takeda, S., Tsuda, A., Turner, S. and Watson, A. J. 'Mesoscale iron enrichment experiments 1993-2005: Synthesis and future directions'. *Science* (2007). **315**(5812) pp. 612–617.

Boye, M., Nishioka, J., Croot, P., Laan, P., Timmermans, K. R., Strass, V. H., Takeda, S. and de Baar, H. J. W. 'Significant portion of dissolved organic Fe complexes in fact is Fe colloids'. *Marine Chemistry* (2010). **122**(1-4) pp. 20–27.

Boye, M., Nishioka, J., Croot, P. L., Laan, P., Timmermans, K. R. and de Baar, H. J. W. 'Major deviations of iron complexation during 22 days of a mesoscale iron enrichment in the open Southern Ocean'. *Marine Chemistry* (2005). **96**(3-4) pp. 257–271.

Boye, M., van den Berg, C. M. G., de Jong, J. T. M., Leach, H., Croot, P. and de Baar, H. J. W. 'Organic complexation of iron in the Southern Ocean'. *Deep-Sea Research Part I-Oceanographic Research Papers* (2001). **48**(6) pp. 1477–1497.

Breier, J. A., Toner, B. M., Fakra, S. C., Marcus, M. A., White, S. N., Thurnherr, A. M. and German, C. R. 'Sulfur, sulfides, oxides and organic matter aggregated in submarine hydrothermal plumes at 9 degrees 50'N East Pacific Rise'. *Geochimica et Cosmochimica Acta* (2012). **88** pp. 216–236.

Bruguier, N. J. and Livermore, R. A. 'Enhanced magma supply at the southern East Scotia Ridge: evidence for mantle flow around the subducting slab?' *Earth and Planetary Science Letters* (2001). **191**(1-2) pp. 129–144.

Bruland, K. W., Franks, R. P., Knauer, G. A. and Martin, J. H. 'Sampling and analytical methods for the determination of copper, cadmium, zinc, and nickel at the nanogram per liter level in sea-water'. *Analytica Chimica Acta* (1979). **105**(1) pp. 233–245.

Bucciarelli, E., Blain, S. and Tréguer, P. 'Iron and manganese in the wake of the Kerguelen Islands (Southern Ocean)'. *Marine Chemistry* (2001). **73**(1) pp. 21–36.

Buck, K. N. and Bruland, K. W. 'The physicochemical speciation of dissolved iron in the Bering Sea, Alaska'. *Limnology and Oceanography* (2007). **52**(5) pp. 1800–1808.

Buck, K. N., Lohan, M. C., Berger, C. J. M. and Bruland, K. W. 'Dissolved iron speciation in two distinct river plumes and an estuary: Implications for riverine iron supply'. *Limnology and Oceanography* (2007). **52**(2) pp. 843–855.

Buck, K. N., Moffett, J. W., Barbeau, K. A., Bundy, R. M., Kondo, Y. and Wu, J. 'The organic complexation of iron and copper: an intercomparison of competitive ligand exchange–adsorptive cathodic stripping voltammetry (CLE-ACSV) techniques'. *Limnology and Oceanography: Methods* (2012). **10** pp. 496–515.

Butler, I. B. and Rickard, D. 'Framboidal pyrite formation via the oxidation of iron (II) monosulfide by hydrogen sulphide'. *Geochimica et Cosmochimica Acta* (2000). **64**(15) pp. 2665–2672.

Butterfield, D. and Massoth, G. 'Geochemistry Of North Cleft Segment Vent Fluids - Temporal Changes In Chlorinity And Their Possible Relation To Recent Volcanism'. *Journal of Geophysical Research-Solid Earth* (1994). **99**(B3) pp. 4951–4968.

Butterfield, D., Massoth, G., Mcduff, R., Lupton, J. and Lilley, M. 'Geochemistry Of Hydrothermal Fluids From Axial Seamount Hydrothermal Emissions Study Vent Field, Juan-De-Fuca Ridge - Subseafloor Boiling And Subsequent Fluid-Rock Interaction'. *Journal of Geophysical Research-Solid Earth And Planets* (1990). **95**(B8) pp. 12,895–12,921.

Butterfield, D. A., Nakamura, K.-i., Takano, B., Lilley, M. D., Lupton, J. E., Resing, J. A. and Roe, K. K. 'High SO2 flux, sulfur accumulation, and gas fractionation at an erupting submarine volcano'. *Geology* (2011). **39**(9) pp. 803–806.

Butterfield, D. D., McDuff, R. E. and Mottl, M. J. 'Gradients in the composition of hydrothermal fluids from the Endeavour segment vent field: Phase separation and brine loss'. *Journal of Geophysical Research* (1994). **99**(B5) p. 9561.

Byrne, R. H. and Kester, D. R. 'Solubility of hydrous ferric oxide and iron speciation in seawater'. *Marine Chemistry* (1976). **4**(3) pp. 255 – 274.

Byrne, R. H., Yao, W. S., Luo, Y. R. and Wang, B. 'The dependence of Fe-III hydrolysis on ionic strength in NaCl solutions'. *Marine Chemistry* (2005). **97**(1-2) pp. 34–48.

Campbell, A., Bowers, T., Measures, C., Falkner, K., Khadem, M. and Edmond, J. 'A Time-Series Of Vent Fluid Compositions From 21-Degrees-N, East Pacific Rise (1979, 1981, 1985), And The Guaymas Basin, Gulf Of California (1982, 1985)'. *Journal of Geophysical Research-Solid Earth And Planets* (1988). **93**(B5) pp. 4537–4549.

Campbell, A. C., Palmer, M. R., Klinkhammer, G. P., Bowers, T. S., Edmond, J. M., Lawrence, J. R., Casey, J. F., Thompson, G., Humphris, S., Rona, P. and Karson, J. A. 'Chemistry of hot springs on the Mid-Atlantic Ridge'. *Nature* (1988). **335** pp. 514–519.

Chen, M., Dei, R. C., Wang, W.-X. and Guo, L. 'Marine diatom uptake of iron bound with natural colloids of different origins'. *Marine Chemistry* (2003). **81**(3) pp. 177–189.

Chen, M. and Wang, W. X. 'Bioavailability of natural colloid-bound iron to marine plankton: Influences of colloidal size and aging'. *Limnology and Oceanography* (2001). **46**(8) pp. 1956–1967.

Chen, M. and Wang, W. X. 'Phase partitioning and solubility of iron in natural seawater controlled by dissolved organic matter'. *Global Biogeochemical Cycles* (2004). **18** p. GB4013.

Ciglenečki, I. and Ćosović, B. 'Electrochemical study of sulfur species in seawater and marine phytoplankton cultures'. *Marine Chemistry* (1996). **52**(1) pp. 87–97.

Connelly, D. P. and others. 'The Kemp Caldera: A sulfur rich hydrothermal vent system in a back arc basin.' (in prep.).

Connelly, D. P., Statham, P. J. and Knap, A. H. 'Seasonal changes in speciation of dissolved chromium in the surface Sargasso Sea'. *Deep Sea Research Part I: Oceanographic Research Papers* (2006). **53**(12) pp. 1975–1988.

Coombs, D. S. and Landis, C. A. 'Pumice from the South Sandwich Eruption of March 1962 reaches New Zealand'. *Nature* (1966). **209** pp. 289–290.

Cowen, J. P. and Li, Y. H. 'The Influence of a Changing Bacterial Community on Trace-Metal Scavenging in a Deep-Sea Particle Plume'. *Journal of Marine Research* (1991). **49**(3) pp. 517–542.

Cowen, J. P., Massoth, G. J. and Feely, R. A. 'Scavenging rates of dissolved manganese in a hydrothermal vent plume'. *Deep Sea Research Part A. Oceanographic Research Papers* (1990). **37**(10) pp. 1619–1637.

Croot, P. L., Andersson, K., Ozturk, M. and Turner, D. R. 'The distribution and specification of iron along 6 degrees E in the Southern Ocean'. *Deep-Sea Research Part II-Topical Studies in Oceanography* (2004). **51**(22-24) pp. 2857–2879.

Croot, P. L. and Heller, M. I. 'The importance of kinetics and redox in the biogeochemical cycling of iron in the surface ocean.' *Frontiers in Microbiology* (2012). **3**(219).

Croot, P. L. and Johansson, M. 'Determination of iron speciation by cathodic stripping voltammetry in seawater using the competing ligand 2-(2-thiazolylazo)-p-cresol (TAC)'. *Electroanalysis* (2000). **12**(8) pp. 565–576.

Cullen, J. T., Bergquist, B. A. and Moffett, J. W. 'Thermodynamic characterization of the partitioning of iron between soluble and colloidal species in the Atlantic Ocean'. *Marine Chemistry* (2006). **98** pp. 295–303.

Cutter, G. A., Cutter, L. S., Featherstone, A. M. and Lohrenz, S. E. 'Antimony and arsenic biogeochemistry in the western Atlantic Ocean'. *Deep Sea Research Part II: Topical Studies in Oceanography* (2001). **48**(13) pp. 2895–2915.

Davies, S. and Morgan, J. 'Manganese(II) Oxidation Kinetics On Metal Oxide Surfaces'. *Journal of Colloid And Interface Science* (1989). **129**(1) pp. 63–77.

De Angelis, M. A., Lilley, M. D., Olson, E. J. and Baross, J. A. 'Methane Oxidation in Deep-Sea Hydrothermal Plumes of the Endeavor Segment of the Juan-De-Fuca Ridge'. *Deep-Sea Research Part I-Oceanographic Research Papers* (1993). **40**(6) pp. 1169–1186.

De Baar, H. J. W. and De Jong, J. T. M. 'Distributions, sources and sinks of iron in seawater'. In D. R. Turner and K. A. Hunter (editors), 'The biogeochemistry of iron in seawater', IUPAC Series on Analytical and Physical Chemistry of Environmental Systems, pp. 123–253. John Wiley & Sons Ltd., Chichester (2001).

de Boyer Montégut, C., Madec, G., Fischer, A. S., Lazar, A. and Iudicone, D. 'Mixed layer depth over the global ocean: An examination of profile data and a profile-based climatology'. *Journal of Geophysical Research: Oceans (1978–2012)* (2004). **109**(C12).

de Ronde, C., Baker, E., Massoth, G., Lupton, J., Wright, I., Feely, R. and Greene, R. 'Intra-oceanic subduction-related hydrothermal venting, Kermadec volcanic arc, New Zealand'. *Earth and Planetary Science Letters* (2001). **193**(3-4) pp. 359–369.

De Ronde, C., Baker, E., Massoth, G., Lupton, J., Wright, I., Sparks, R., Bannister, S., Reyners, M., Walker, S., Greene, R. et al. 'Submarine hydrothermal activity along the mid-Kermadec Arc, New Zealand: Large-scale effects on venting'. *Geochemistry Geophysics Geosystems* (2007). **8**(7) p. Q07,007.

de Ronde, C. E., Hannington, M., Stoffers, P., Wright, I., Ditchburn, R., Reyes, A., Baker, E., Massoth, G., Lupton, J., Walker, S. et al. 'Evolution of a submarine magmatic-hydrothermal system: Brothers volcano, southern Kermadec arc, New Zealand'. *Economic Geology* (2005). **100**(6) pp. 1097–1133.

de Ronde, C. E., Massoth, G. J., Butterfield, D. A., Christenson, B. W., Ishibashi, J., Ditchburn, R. G., Hannington, M. D., Brathwaite, R. L., Lupton, J. E., Kamenetsky, V. S. et al. 'Submarine hydrothermal activity and gold-rich mineralization at Brothers Volcano, Kermadec Arc, New Zealand'. *Mineralium Deposita* (2011). **46**(5) pp. 541–584.

Dehner, C. A., Barton, L., Maurice, P. A. and Dubois, J. L. 'Size-Dependent Bioavailability of Hematite (alpha-Fe2O3) Nanoparticles to a Common Aerobic Bacterium'. *Environmental Science & Technology* (2011). **45**(3) pp. 977–983.

Dick, G. J., Clement, B. G., Webb, S. M., Fodrie, F. J., Bargar, J. R. and Tebo, B. M. 'Enzymatic microbial Mn(II) oxidation and Mn biooxide production in the Guaymas Basin deep-sea hydrothermal plume'. *Geochimica et Cosmochimica Acta* (2009). **73**(21) pp. 6517–6530.

Douville, E., Charlou, J. L., Oelkers, E. H., Bienvenu, P., Colon, C. F. J., Donval, J. P., Fouquet, Y., Prieur, D. and Appriou, P. 'The rainbow vent fluids (36 degrees 14 N, MAR): the influence of ultramafic rocks and phase separation on trace metal content in Mid-Atlantic Ridge hydrothermal fluids'. *Chemical Geology* (2002). **184**(1-2) pp. 37–48.

Edmonds, H. and German, C. 'Particle geochemistry in the Rainbow hydrothermal plume, Mid-Atlantic Ridge'. *Geochimica et Cosmochimica Acta* (2004). **68**(4) pp. 759–772.

Elderfield, H. and Schultz, A. 'Mid-ocean ridge hydrothermal fluxes and the chemical composition of the ocean'. *Annual Review of Earth and Planetary Sciences* (1996). **24** pp. 191–224.

Embley, R., Baker, E., Butterfield, D., Chadwick, W., Lupton, J., Resing, J., De Ronde, C., Nakamura, K., Tunnicliffe, V., Dower, J. et al. 'Exploring the sub-

marine ring of fire: Mariana Arc-Western Pacific'. *Oceanography* (2007). **20**(4) p. 68.

Farley, K. J. and Morel, F. M. M. 'Role of Coagulation in the Kinetics of Sedimentation'. *Environmental Science & Technology* (1986). **20**(2) pp. 187–195.

Feely, R., Baker, E., Marumo, K., Urabe, T., Ishibashi, J., Gendron, J., Lebon, G. and Okamura, K. 'Hydrothermal plume particles and dissolved phosphate over the superfast-spreading southern East Pacific Rise'. *Geochimica et Cosmochimica Acta* (1996). **60**(13) pp. 2297–2323.

Feely, R., Gendron, J., Baker, E. and Lebon, G. 'Hydrothermal plumes along the East Pacific Rise, 8 40' to 11 50' N: Particle distribution and composition'. *Earth and Planetary Science Letters* (1994a). **128**(1) pp. 19–36.

Feely, R., Lewison, M., Massoth, G., Robertbaldo, G., Lavelle, J., Byrne, R., Vondamm, K. and Curl, H. 'Composition And Dissolution Of Black Smoker Particulates From Active Vents On The Juan-De-Fuca Ridge'. *Journal of Geophysical Research-Solid Earth And Planets* (1987). **92**(B11) pp. 11,347–11,363.

Feely, R., Trefry, J., Lebon, G. and German, C. 'The relationship between P/Fe and V/Fe ratios in hydrothermal precipitates and dissolved phosphate in seawater'. *Geophysical Research Letters* (1998). **25**(13) pp. 2253–2256.

Feely, R. A., Geiselman, T. L., Baker, E. T., Massoth, G. J. and Hammond, S. R. 'Distribution And Composition Of Hydrothermal Plume Particles From The Ashes Vent Field At Axial Volcano, Juan-de-Fuca Ridge'. *Journal of Geophysical Research-Solid Earth and Planets* (1990). **95**(B8) pp. 12,855–12,873.

Feely, R. A., Massoth, G. J., Trefry, J. H., Baker, E. T., Paulson, A. J. and Lebon, G. T. 'Composition and sedimentation of hydrothermal plume particles from North Cleft segment, Juan de Fuca Ridge'. *Journal of Geophysical Research: Solid Earth (1978–2012)* (1994b). **99**(B3) pp. 4985–5006.

Feely, R. A., Trefry, J. H., Massoth, G. J. and Metz, S. 'A comparison of the scavenging of phosphorus and arsenic from seawater by hydrothermal iron oxyhydroxides in the Atlantic and Pacific Oceans'. *Deep Sea Research Part A. Oceanographic Research Papers* (1991). **38**(6) pp. 617–623.

Field, M. P. and Sherrell, R. M. 'Dissolved and particulate Fe in a hydrothermal plume at 9 degrees 45' N, East Pacific Rise: Slow Fe (II) oxidation kinetics in Pacific plumes'. *Geochimica et Cosmochimica Acta* (2000). **64**(4) pp. 619–628.

Fitzsimmons, J. N., Zhang, R. and Boyle, E. A. 'Dissolved iron in the tropical North Atlantic Ocean'. *Marine Chemistry* (2013).

Fouquet, Y. 'Where are the large hydrothermal sulphide deposits in the oceans?' *Philosophical Transactions of the Royal Society of London. Series A: Mathematical, Physical and Engineering Sciences* (1997). **355**(1723) pp. 427–441.

Fouquet, Y., von Stackelberg, U., Charlou, J. L., Donval, J. P., Foucher, J. P., Erzinger, J., Herzig, P., Mühe, R., Wiedicke, M., Soakai, S. et al. 'Hydrothermal

activity in the Lau back-arc basin: Sulfides and water chemistry'. *Geology* (1991). **19**(4) pp. 303–306.

Frank, M., Marbler, H., Koschinsky, A., van de Flierdt, T., Klemm, V., Gutjahr, M., Halliday, A., Kubik, P. and Halbach, P. 'Submarine hydrothermal venting related to volcanism in the Lesser Antilles: Evidence from ferromanganese precipitates'. *Geochemistry, Geophysics, Geosystems* (2006). **7**(4).

Froelich, P., Klinkhammer, G., Bender, M., Luedtke, N., Heath, G., Cullen, D., Dauphin, P., Hammond, D., Hartman, B. and Maynard, V. 'Early Oxidation Of Organic-Matter In Pelagic Sediments Of The Eastern Equatorial Atlantic - Suboxic Diagenesis'. *Geochimica et Cosmochimica Acta* (1979). **43**(7) pp. 1075–1090.

Gallant, R. M. and Von Damm, K. L. 'Geochemical controls on hydrothermal fluids from the Kairei and Edmond Vent Fields, 23 degrees-25 degrees S, Central Indian Ridge'. *Geochemistry Geophysics Geosystems* (2006). **7** p. 24.

Gamo, T., Ishibashi, J., Tsunogai, U., Okamura, K. and Chiba, H. 'Unique geochemistry of submarine hydrothermal fluids from arc-back-arc settings of the western Pacific'. *Geophysical Monograph Series* (2006). **166** pp. 147–161.

Gamo, T., Okamura, K., Charlou, J.-L., Urabe, T., Auzende, J.-M., Ishibashi, J., Shitashima, K., Chiba, H. et al. 'Acidic and sulfate-rich hydrothermal fluids from the Manus back-arc basin, Papua New Guinea'. *Geology* (1997). **25**(2) pp. 139–142.

Gartman, A. and Luther, G. W. 'Comparison of pyrite (FeS< sub> 2</sub>) synthesis mechanisms to reproduce natural FeS< sub> 2</sub> nanoparticles found at hydrothermal vents'. *Geochimica et Cosmochimica Acta* (2013).

Gartman, A., Yücel, M., Madison, A. S., Chu, D. W., Ma, S., Janzen, C. P., Becker, E. L., Beinart, R. A., Girguis, P. R. and Luther III, G. W. 'Sulfide oxidation across diffuse flow zones of hydrothermal vents'. *Aquatic Geochemistry* (2011). **17**(4-5) pp. 583–601.

German, C., Colley, S., Palmer, M., Khripounoff, A. and Klinkhammer, G. 'Hydrothermal plume-particle fluxes at 13 N on the East Pacific Rise'. *Deep Sea Research Part I: Oceanographic Research Papers* (2002). **49**(11) pp. 1921–1940.

German, C., Hergt, J., Palmer, M. and Edmond, J. 'Geochemistry of a hydrothermal sediment core from the {OBS} vent-field, 21 °N East Pacific Rise'. *Chemical Geology* (1999). **155**(1–2) pp. 65 – 75.

German, C. R., Campbell, A. C. and Edmond, J. M. 'Hydrothermal scavenging at the Mid-Atlantic Ridge - modification of trace-element dissolved fluxes'. *Earth and Planetary Science Letters* (1991). **107**(1) pp. 101–114.

German, C. R., Klinkhammer, G. P., Edmond, J. M., Mitra, A. and Elderfield, H. 'Hydrothermal scavenging of Rare-Earth Elements in the ocean'. *Nature* (1990). **345**(6275) pp. 516–518.

German, C. R., Livermore, R. A., Baker, E. T., Bruguier, N. I., Connelly, D. P., Cunningham, A. P., Morris, P., Rouse, I. P., Statham, P. J. and Tyler, P. A. 'Hydrothermal plumes above the East Scotia Ridge: an isolated high-latitude back-arc spreading centre'. *Earth and Planetary Science Letters* (2000). **184**(1) pp. 241–250.

German, C. R., Thurnherr, A. M., Knoery, J., Charlou, J.-L., Jean-Baptiste, P. and Edmonds, H. N. 'Heat, Volume and chemical fluxes from submarine venting: A synthesis of results from the Rainbow hydrothermal field, 36 °N MAR'. *Deep Sea Res. I* (2010). **57** pp. 518–527.

German, C. R. and Von Damm, K. L. 'Hydrothermal Processes'. In H. Holland and K. Turekian (editors), 'The Oceans and marine Geochemistry', volume 6, pp. 181–222. Elsevier-Pergamon, Oxford (2004).

Gerringa, L. J. A., Rijkenberg, M. J. A., Wolterbeek, H. T., Verburg, T. G., Boye, M. and de Baar, H. J. W. 'Kinetic study reveals weak Fe-binding ligand, which affects the solubility of Fe in the Scheldt estuary'. *Marine Chemistry* (2007). **103**(1-2) pp. 30–45.

Gledhill, M. and Buck, K. N. 'The organic complexation of iron in the marine environment: a review'. *Frontiers in Microbiology* (2012). **3** p. 69.

Gledhill, M., van den Berg, C., Nolting, R. and Timmermans, K. 'Variability in the speciation of iron in the northern North Sea'. *Marine Chemistry* (1998). **59**(3-4) pp. 283–300.

Gledhill, M. and van den Berg, C. M. G. 'Determination of Complexation of Iron(III) with Natural Organic Complexing Ligands in Seawater Using Cathodic Stripping Voltammetry'. *Marine Chemistry* (1994). **47**(1) pp. 41–54.

Hassler, C. S., Legiret, F. and Butler, E. C. V. 'Measurement of iron chemical speciation in seawater at 4 °C: The use of competitive ligand exchange–adsorptive cathodic stripping voltammetry'. *Marine Chemistry* (2013). **149** pp. 63–73.

Hassler, C. S. and Schoemann, V. 'Bioavailability of organically bound Fe to model phytoplankton of the Southern Ocean'. *Biogeosciences* (2009). **6**(10) pp. 2281–2296.

Hawkes, J. A., Connelly, D. P., Gledhill, M. and Achterberg, E. P. 'The stabilisation and transportation of dissolved iron from high temperature hydrothermal vent systems'. *Earth and Planetary Science Letters* (2013a). **375** pp. 280–290.

Hawkes, J. A., Gledhill, M., Connelly, D. P. and Achterberg, E. P. 'Characterisation of iron binding ligands in seawater by reverse titration'. *Analytica Chimica Acta* (2013b). **766**(53-60).

He, Y., Zheng, Y. and Locke, D. C. 'Differential pulse cathodic stripping voltammetric determination of nanomolar levels of dissolved sulfide applicable to field analysis of groundwater'. *Analytica Chimica Acta* (2002). **459**(2) pp. 209–217.

Hiemstra, T. and van Riemsdijk, W. H. 'Biogeochemical speciation of Fe in ocean water'. *Marine Chemistry* (2006). **102**(3 - 4) pp. 181 – 197.

Hitch, J. *Spectroscopic Analysis of Hydrothermal Plume Particles from the Scotia Sea*. Master's thesis, University of Southampton (2012).

Homoky, W. B., Hembury, D. J., Hepburn, L. E., Mills, R. A., Statham, P. J., Fones, G. R. and Palmer, M. R. 'Iron and manganese diagenesis in deep sea volcanogenic sediments and the origins of pore water colloids'. *Geochimica et Cosmochimica Acta* (2011). **75**(17) pp. 5032–5048.

Honeyman, B. D. and Santschi, P. H. 'A Brownian-Pumping Model for Oceanic Trace-Metal Scavenging - Evidence from Th-Isotopes'. *Journal of Marine Research* (1989). **47**(4) pp. 951–992.

Honeyman, B. D. and Santschi, P. H. 'Coupling adsorption and particle aggregation - Laboratory studies of colloidal pumping using Fe-59 labeled hematite'. *Environmental Science & Technology* (1991). **25**(10) pp. 1739–1747.

Hsu-Kim, H., Mullaugh, K. M., Tsang, J. J., Yucel, M. and Luther, G. W. 'Formation of Zn- and Fe-sulfides near hydrothermal vents at the Eastern Lau Spreading Center: implications for sulfide bioavailability to chemoautotrophs'. *Geochemical Transactions* (2008). **9** p. 14.

Hudson, R. J. M. and Morel, F. M. M. 'Iron transport in marine-phytoplankton - Kinetics of cellular and medium coordination reactions'. *Limnology and Oceanography* (1990). **35**(5) pp. 1002–1020.

Hunter, K. A. and Boyd, P. W. 'Iron-binding ligands and their role in the ocean biogeochemistry of iron'. *Environmental Chemistry* (2007). **4**(4) pp. 221–232.

Hunter, K. A. and Liss, P. S. 'Organic-Matter and the Surface-Charge of Suspended Particles in Estuarine Waters'. *Limnology and Oceanography* (1982). **27**(2) pp. 322–335.

Hutchins, D. A., Witter, A. E., Butler, A. and Luther, G. W. 'Competition among marine phytoplankton for different chelated iron species'. *Nature* (1999). **400**(6747) pp. 858–861.

Ishibashi, J.-i., Sano, Y., Wakita, H., Gamo, T., Tsutsumi, M. and Sakai, H. 'Helium and carbon geochemistry of hydrothermal fluids from the Mid-Okinawa Trough Back Arc Basin, southwest of Japan'. *Chemical Geology* (1995). **123**(1) pp. 1–15.

James, R. H., Green, D. R. H., Stock, M. J., Connelly, D. P., Alker, B. J., Banerjee, N., Cole, C., German, C. R., Huvenne, V. A. I. and Powell, A. 'Geochemistry of hydrothermal fluids and associated mineralisation on the East Scotia Ridge' (in prep.).

Jeandel, C. and Minster, J.-F. 'Isotope dilution measurement of inorganic chromium(III) and total chromium in seawater'. *Marine Chemistry* (1984). **14**(4) pp. 347 – 364.

Jeandel, C. and Minster, J. F. 'Chromium behavior in the ocean: Global versus regional processes'. *Global Biogeochemical Cycles* (1987). **1**(2) pp. 131–154.

Johnson, K. S., Gordon, R. M. and Coale, K. H. 'What controls dissolved iron concentrations in the world ocean?' *Marine Chemistry* (1997). **57**(3-4) pp. 137–161.

Karl, D. M. *The Microbiology of deep-sea hydrothermal vents*. Extreme and Unusual Environments. CRC Press Inc., Roca Raton, FL (1995).

Kelley, D. S. 'Methane-rich fluids in the oceanic crust'. *Journal of Geophysical Research* (1996). **101**(B2) p. 2943.

Kelley, D. S. and Fruh-Green, G. 'Volatiles in mid-ocean ridge environments'. *Special Papers-Geological Society Of America* (2000). pp. 237–260.

Klevenz, V., Bach, W., Schmidt, K., Hentscher, M., Koschinsky, A. and Petersen, S. 'Geochemistry of vent fluid particles formed during initial hydrothermal fluid-seawater mixing along the Mid-Atlantic Ridge'. *Geochemistry Geophysics Geosystems* (2011). **12**(10) p. Q0AE05.

Klinkhammer, G., Elderfield, H., Greaves, M., Rona, P. and Nelsen, T. 'Manganese geochemistry near high-temperature vents in the Mid-Atlantic Ridge rift-valley'. *Earth and Planetary Science Letters* (1986). **80**(3-4) pp. 230–240.

Klinkhammer, G., Elderfield, H. and Hudson, A. 'Rare earth elements in seawater near hydrothermal vents'. *Nature* (1983). **305** pp. 195–188.

Klunder, M. B., Bauch, D., Laan, P., De Baar, H. J., Van Heuven, S. and Ober, S. 'Dissolved iron in the Arctic shelf seas and surface waters of the central Arctic Ocean: Impact of Arctic river water and ice-melt'. *Journal of Geophysical Research* (2012). **117**(C1) p. C01,027.

Klunder, M. B., Laan, P., Middag, R., De Baar, H. J. W. and van Ooijen, J. C. 'Dissolved iron in the Southern Ocean (Atlantic sector)'. *Deep-Sea Research Part I-Oceanographic Research Papers* (2011). **58**(25-26) pp. 2678–2694.

Kondo, Y., Takeda, S. and Furuya, K. 'Distinct trends in dissolved Fe speciation between shallow and deep waters in the Pacific Ocean'. *Marine Chemistry* (2012). **134-135**(0) pp. 18 – 28.

Koschinsky, A., Garbe-Schonberg, D., Sander, S., Schmidt, K., Gennerich, H. H. and Strauss, H. 'Hydrothermal venting at pressure-temperature conditions above the critical point of seawater, 5 degrees S on the Mid-Atlantic Ridge'. *Geology* (2008). **36**(8) pp. 615–618.

Koschinsky, A. and Hein, J. R. 'Uptake of elements from seawater by ferromanganese crusts: solid-phase associations and seawater speciation'. *Marine Geology* (2003). **198**(3) pp. 331–351.

Kuma, K., Nakabayashi, S. and Matsunaga, K. 'Photoreduction Of Fe(III) By

Hydroxycarboxylic Acids In Seawater'. *Water Research* (1995). **29**(6) pp. 1559–1569.

Kuma, K., Nakabayashi, S., Suzuki, Y., Kudo, I. and Matsunaga, K. 'Photo-Reduction Of Fe (III) By Dissolved Organic-Substances And Existence Of Fe (II) In Seawater During Spring Blooms'. *Marine Chemistry* (1992). **37**(1-2) pp. 15–27.

Kuma, K., Nishioka, J. and Matsunaga, K. 'Controls on iron (III) hydroxide solubility in seawater: The influence of pH and natural organic chelators'. *Limnology and Oceanography* (1996). pp. 396–407.

Laglera, L. M., Battaglia, G. and van den Berg, C. M. G. 'Effect of humic substances on the iron speciation in natural waters by CLE/CSV'. *Marine Chemistry* (2011). **127**(1-4) pp. 134–143.

Laglera, L. M., Downes, J. and Santos-Echeandía, J. 'Comparison and combined use of linear and non-linear fitting for the estimation of complexing parameters from metal titrations of estuarine samples by CLE/AdCSV'. *Marine Chemistry* (2013).

Laglera, L. M. and Tovar-Sánchez, A. 'Direct recognition and quantification by voltammetry of thiol/thioamide mixes in seawater'. *Talanta* (2012). **89** pp. 496–504.

Laglera, L. M. and van den Berg, C. M. G. 'Evidence for geochemical control of iron by humic substances in seawater'. *Limnology and Oceanography* (2009). **54**(2) pp. 610–619.

Landing, W. M. and Bruland, K. W. 'The contrasting biogeochemistry of iron and manganese in the Pacific Ocean'. *Geochimica et Cosmochimica Acta* (1987). **51**(1) pp. 29–43.

Lang, S. Q., Butterfield, D. A. and Lilley, M. D. 'Dissolved organic carbon in ridge-axis and ridge-flank hydrothermal systems'. *Geochimica et Cosmochimica Acta* (2006). **70** p. 3830.

Larter, R. D. and others. 'Discovery of a young, hydrothermally active submarine caldera on the South Sandwich volcanic arc' (in prep.).

Lavelle, J., Cowen, J. and Massoth, G. 'A model for the deposition of hydrothermal manganese near ridge crests'. *Journal of Geophysical Research: Oceans (1978–2012)* (1992). **97**(C5) pp. 7413–7427.

Leat, P., Livermore, R., Millar, I. and Pearce, J. 'Magma supply in back-arc spreading centre segment E2, East Scotia Ridge'. *Journal of Petrology* (2000). **41**(6) pp. 845–866.

Leat, P., Pearce, J., Barker, P., Millar, I., Barry, T. and Larter, R. 'Magma genesis and mantle flow at a subducting slab edge: the South Sandwich arc-basin system'. *Earth and Planetary Science Letters* (2004). **227**(1) pp. 17–35.

Lewis, E. and Wallace, D. W. R. *Program Developed for CO2 System Calculations*. Carbon Dioxide Information Analysis Center, Oak Ridge National Laboratory, U.S. Department of Energy, Oak Ridge, TN, USA (1998).

Leybourne, M. I., Schwarz-Schampera, U., de Ronde, C. E. J., Baker, E. T., Faure, K., Walker, S. L., Butterfield, D. A., Resing, J. A., Lupton, J. E., Hannington, M. D., Gibson, H. L., Massoth, G. J., Embley, R. W., Chadwick, W. W., Jr., Clark, M. R., Timm, C., Graham, I. J. and Wright, I. C. 'Submarine Magmatic-Hydrothermal Systems at the Monowai Volcanic Center, Kermadec Arc'. *Economic Geology* (2012). **107**(8, SI) pp. 1669–1694.

Lilley, M. D. 'Anomalous CH4 and NH4+ concentrations at an unsedimented mid-ocean-ridge hydrothermal system'. *Nature* (1993). **364** p. 45.

Liu, X. and Millero, F. J. 'The Solubility of Iron in Seawater'. *Marine Chemistry* (2002). **77** p. 43.

Livermore, R., Cunningham, A., Vanneste, L. and Larter, R. 'Subduction influence on magma supply at the East Scotia Ridge'. *Earth and Planetary Science Letters* (1997). **150**(3-4) pp. 261–275.

Livermore, R. A. *Back-arc spreading and mantle flow in the East Scotia Sea*, volume 219 of *Intra-Oceanic Subduction Systems: Tectonic and Magmatic Processes*. Geological Society, London, Special Publications (2003).

Loscher, B. M., De Baar, H. J. W., De Jong, J. T. M., Veth, C. and Dehairs, F. 'The distribution of Fe in the antarctic circumpolar current'. *Deep Sea Research Part II: Topical Studies in Oceanography* (1997). **44**(1-2) pp. 143–187.

Lupton, J., Delaney, J., Johnson, H. and Tivey, M. 'Entrainment And Vertical Transport Of Deep-Ocean Water By Buoyant Hydrothermal Plumes'. *Nature* (1985). **316**(6029) pp. 621–623.

Luther, G. and Rickard, D. 'Metal sulfide cluster complexes and their biogeochemical importance in the environment'. *Journal of Nanoparticle Research* (2005). **7**(4-5) pp. 389–407.

Luther, G. W. and Ferdelman, T. G. 'Voltammetric Characterization of Iron(II) Sulfide Complexes in Laboratory Solutions and in Marine Waters and Porewaters'. *Environmental Science & Technology* (1993). **27** pp. 1154–1163.

Luther, G. W., Glazer, B., Ma, S., Trouwborst, R., Shultz, B. R., Druschel, G. and Kraiya, C. 'Iron and sulfur chemistry in a stratified lake: Evidence for iron-rich sulfide complexes'. *Aquatic Geochemistry* (2003). **9**(2) pp. 87–110.

Luther, G. W., Rickard, D. T., Theberge, S. and Olroyd, A. 'Determination of Metal (Bi)Sulfide Stability Constants of Mn2+, Fe2+, Co2+, Ni2+, Cu2+ and Zn2+ by Voltammetric Methods'. *Environmental Science & Technology* (1996). **30** pp. 671–679.

Luther, G. W. and Tsamakis, E. 'Concentration and form of dissolved sulfide in the oxic water column of the ocean'. *Marine Chemistry* (1989). **27**(3) pp. 165–177.

Luther III, G. W. and Wu, J. 'What controls dissolved iron concentrations in the world ocean?: a comment'. *Marine Chemistry* (1997). **57** pp. 173 – 179.

Mackey, D. and Zirino, A. 'Comments On Trace-Metal Speciation In Seawater Or Do Onions Grow In The Sea'. *Analytica Chimica Acta* (1994). **284**(3) pp. 635–647.

Marbler, H., Koschinsky, A., Pape, T., Seifert, R., Weber, S., Baker, E., de Carvalho, L. and Schmidt, K. 'Geochemical and physical structure of the hydrothermal plume at the ultramafic-hosted Logatchev hydrothermal field at 14 45' N on the Mid-Atlantic Ridge'. *Marine Geology* (2010). **271**(3) pp. 187–197.

Marsh, R., Mills, R. A., Green, D. R., Salter, I. and Taylor, S. 'Controls on sediment geochemistry in the Crozet region'. *Deep Sea Research Part II: Topical Studies in Oceanography* (2007). **54**(18-20) pp. 2260 – 2274.

Marshall, J. and Speer, K. 'Closure of the meridional overturning circulation through Southern Ocean upwelling'. *Nature Geoscience* (2012). **5**(3) pp. 171–180.

Martin, J. H. and Fitzwater, S. E. 'Iron-deficiency limits phytoplankton growth in the northeast Pacific subarctic'. *Nature* (1988). **331**(6154) pp. 341–343.

Martin, J. H., Fitzwater, S. E., Michael Gordon, R., Hunter, C. N. and Tanner, S. J. 'Iron, primary production and carbon-nitrogen flux studies during the JGOFS North Atlantic Bloom Experiment'. *Deep Sea Research Part II: Topical Studies in Oceanography* (1993). **40**(1) pp. 115–134.

Martin, J. H., Gordon, R. M., Fitzwater, S. and Broenkow, W. W. 'VERTEX: Phytoplankton/iron studies in the Gulf of Alaska'. *Deep Sea Research Part A. Oceanographic Research Papers* (1989). **36**(5) pp. 649–680.

Massoth, G., Baker, E., Worthington, T., Lupton, J., de Ronde, C., Arculus, R., Walker, S., Nakamura, K.-i., Ishibashi, J.-i., Stoffers, P. et al. 'Multiple hydrothermal sources along the south Tonga arc and Valu Fa Ridge'. *Geochemistry, Geophysics, Geosystems* (2007). **8**(11).

Massoth, G. J., De Ronde, C. E., Lupton, J. E., Feely, R. A., Baker, E. T., Lebon, G. T. and Maenner, S. M. 'Chemically rich and diverse submarine hydrothermal plumes of the southern Kermadec volcanic arc (New Zealand)'. *Geological Society, London, Special Publications* (2003). **219**(1) pp. 119–139.

McGillicuddy, D. J., Anderson, L. A., Bates, N. R., Bibby, T., Buesseler, K. O., Carlson, C. A., Davis, C. S., Ewart, C., Falkowski, P. G., Goldthwait, S. A. et al. 'Eddy/wind interactions stimulate extraordinary mid-ocean plankton blooms'. *Science* (2007). **316**(5827) pp. 1021–1026.

Metz, S. and Trefry, J. H. 'Field and laboratory studies of metal uptake and release by hydrothermal precipitates'. *Journal of Geophysical Research* (1993). **98**(B6) pp. 9661–9666.

Michard, A., Albarede, F., Michard, G., Minster, J. and Charlou, J. 'Rare-Earth Elements And Uranium In High-Temperature Solutions From East Pacific Rise Hydrothermal Vent Field (13-Degrees-N)'. *Nature* (1983). **303**(5920) pp. 795–797.

Millero, F. J. and Pierrot, D. 'The activity coefficients of Fe(III) hydroxide complexes in NaCl and NaClO4 solutions'. *Geochimica et Cosmochimica Acta* (2007). **71**(20) pp. 4825–4833.

Millero, F. J., Sotolongo, S. and Izaguirre, M. 'The oxidation kinetics of Fe(II) in seawater'. *Geochimica et Cosmochimica Acta* (1987). **51**(4) pp. 793–801.

Millero, F. J., Woosley, R., Ditrolio, B. and Waters, J. 'Effect of Ocean Acidification on the Speciation of Metals in Seawater'. *Oceanography* (2009). **22**(4) pp. 72–85.

Millero, F. J., Yao, W. S. and Aicher, J. 'The speciation of Fe(II) and Fe(III) in natural waters'. *Marine Chemistry* (1995). **50**(1-4) pp. 21–39.

Moore, J. K. and Braucher, O. 'Sedimentary and mineral dust sources of dissolved iron to the world ocean'. *Biogeosciences* (2008). **5**(3) pp. 631–656.

Morel, F. M., Kustka, A. and Shaked, Y. 'The role of unchelated Fe in the iron nutrition of phytoplankton'. *Limnology and Oceanography* (2008). pp. 400–404.

Mosley, L. M., Hunter, K. A. and Ducker, W. A. 'Forces between colloid particles in natural waters'. *Environmental Science & Technology* (2003). **37**(15) pp. 3303–3308.

Mosselmans, J. F. W., Quinn, P. D., Dent, A. J., Cavill, S. A., Moreno, S. D., Peach, A., Leicester, P. J., Keylock, S. J., Gregory, S. R., Atkinson, K. D. et al. 'I18-the microfocus spectroscopy beamline at the Diamond Light Source'. *Journal of Synchrotron Radiation* (2009). **16**(6) pp. 818–824.

Mottl, M. J. and McConachy, T. F. 'Chemical Processes in Buoyant Hydrothermal Plumes on the East Pacific Rise near 21-Degrees-N'. *Geochimica et Cosmochimica Acta* (1990). **54**(7) pp. 1911–1927.

Mottl, M. J., Seewald, J. S., Wheat, C. G., Tivey, M. K., Michael, P. J., Proskurowski, G., McCollom, T. M., Reeves, E., Sharkey, J., You, C. F., Chan, L. H. and Pichler, T. 'Chemistry of hot springs along the Eastern Lau Spreading Center'. *Geochimica et Cosmochimica Acta* (2011). **75**(4) pp. 1013–1038.

Mottl, M. J. and Wheat, C. G. 'Hydrothermal circulation through mid-ocean ridge flanks: Fluxes of heat and magnesium'. *Geochimica et Cosmochimica Acta* (1994). **58**(10) pp. 2225–2237.

Nagai, T., Imai, A., Matsushige, K., Yokoi, K. and Fukushima, T. 'Voltammetric determination of dissolved iron and its speciation in freshwater'. *Limnology* (2004). **5** pp. 87–94.

Naveira-Garabato, A., Heywood, K. and Stevens, D. 'Modification and pathways of Southern Ocean Deep Waters in the Scotia Sea'. *Deep-Sea Research Part I-Oceanographic Research Papers* (2002). **49**(4) pp. 681–705.

Nelsen, T. A., Klinkhammer, G. P., Trefry, J. H. and Trocine, R. P. 'Real-time observation of dispersed hydrothermal plumes using nephelometry - Examples

from the Mid-Atlantic Ridge'. *Earth and Planetary Science Letters* (1987). **81**(2-3) pp. 245–252.

Nishioka, J., Obata, H. and Tsumune, D. 'Evidence of an extensive spread of hydrothermal dissolved iron in the Indian Ocean'. *Earth and Planetary Science Letters* (2013). **361** pp. 26–33.

Nishioka, J., Takeda, S., de Baar, H. J. W., Croot, P. L., Boye, M., Laan, P. and Timmermans, K. R. 'Changes in the concentration of iron in different size fractions during an iron enrichment experiment in the open Southern Ocean'. *Marine Chemistry* (2005). **95**(1-2) pp. 51–63.

Nishioka, J., Takeda, S., Wong, C. S. and Johnson, W. K. 'Size-fractionated iron concentrations in the northeast Pacific Ocean: distribution of soluble and small colloidal iron'. *Marine Chemistry* (2001). **74**(2-3) pp. 157–179.

Nodwell, L. M. and Price, N. M. 'Direct use of inorganic colloidal iron by marine mixotrophic phytoplankton'. *Limnology and Oceanography* (2001). **46**(4) pp. 765–777.

Nolting, R. F., De Baar, H. J. W., Van Bennekom, A. J. and Masson, A. 'Cadmium, copper and iron in the Scotia Sea, Weddell Sea and Weddell/Scotia Confluence (Antarctica)'. *Marine Chemistry* (1991). **35**(1-4) pp. 219–243.

Nuester, J. and van den Berg, C. M. G. 'Determination of metal speciation by reverse titrations'. *Analytical Chemistry* (2005). **77**(1) pp. 11–19.

Olivarez, A. M. and Owen, R. M. 'REE/Fe variations in hydrothermal sediments: Implications for the REE content of seawater'. *Geochimica et Cosmochimica Acta* (1989). **53**(3) pp. 757–762.

Pohl, C. and Fernandez-Otero, E. 'Iron distribution and speciation in oxic and anoxic waters of the Baltic Sea'. *Marine Chemistry* (2012). **145** pp. 1–15.

Poulton, S. W. and Canfield, D. E. 'Co-diagenesis of iron and phosphorus in hydrothermal sediments from the southern East Pacific Rise: Implications for the evaluation of paleoseawater phosphate concentrations'. *Geochimica et Cosmochimica Acta* (2006). **70**(23) pp. 5883–5898.

Reeves, E. P., Seewald, J. S., Saccocia, P., Bach, W., Craddock, P. R., Shanks, W. C., Sylva, S. P., Walsh, E., Pichler, T. and Rosner, M. 'Geochemistry of hydrothermal fluids from the PACMANUS, Northeast Pual and Vienna Woods hydrothermal fields, Manus Basin, Papua New Guinea'. *Geochimica et Cosmochimica Acta* (2011). **75**(4) pp. 1088–1123.

Resing, J., Lebon, G., Baker, E., Lupton, J., Embley, R., Massoth, G., Chadwick, W. and De Ronde, C. 'Venting of acid-sulfate fluids in a high-sulfidation setting at NW Rota-1 submarine volcano on the Mariana Arc'. *Economic Geology* (2007). **102**(6) pp. 1047–1061.

Resing, J. A., Baker, E. T., Lupton, J. E., Walker, S. L., Butterfield, D. A., Massoth, G. J. and Nakamura, K.-i. 'Chemistry of hydrothermal plumes above submarine

volcanoes of the Mariana Arc'. *Geochemistry Geophysics Geosystems* (2009). **10**(2) p. Q02,009.

Rich, H. and Morel, F. 'Availability Of Well-Defined Iron Colloids To The Marine Diatom Thalassiosira-Weissflogii'. *Limnology and Oceanography* (1990). **35**(3) pp. 652–662.

Rickard, D. and Luther, G. W. 'Kinetics of pyrite formation by the H2S oxidation of iron (II) monosulfide in aqueous solutions between 25 and 125 ° C: The mechanism'. *Geochimica et Cosmochimica Acta* (1997). **61**(1) pp. 135–147.

Rickard, D., Oldroyd, A. and Cramp, A. 'Voltammetric evidence for soluble FeS complexes in anoxic estuarine muds'. *Estuaries and Coasts* (1999). **22**(3) pp. 693–701.

Risso, C., Scasso, R. A. and Aparicio, A. 'Presence of large pumice blocks on Tierra del Fuego and South Shetland Islands shorelines, from 1962 South Sandwich Islands eruption'. *Marine Geology* (2002). **186**(3–4) pp. 413 – 422.

Rogers, A. D., Tyler, P. A., Connelly, D. P., Copley, J. T., James, R., Larter, R. D., Linse, K., Mills, R. A., Garabato, A. N., Pancost, R. D., Pearce, D. A., Polunin, N. V. C., German, C. R., Shank, T., Boersch-Supan, P. H., Alker, B. J., Aquilina, A., Bennett, S. A., Clarke, A., Dinley, R. J. J., Graham, A. G. C., Green, D. R. H., Hawkes, J. A., Hepburn, L., Hilario, A., Huvenne, V. A. I., Marsh, L., Ramirez-Llodra, E., Reid, W. D. K., Roterman, C. N., Sweeting, C. J., Thatje, S. and Zwirglmaier, K. 'The Discovery of New Deep-Sea Hydrothermal Vent Communities in the Southern Ocean and Implications for Biogeography'. *PLoS Biology* (2012). **10**(1) p. e1001,234.

Roth, S. E. and Dymond, J. 'Transport and settling of organic material in a deep-sea hydrothermal plume: evidence from particle flux measurements'. *Deep Sea Research Part A. Oceanographic Research Papers* (1989). **36**(8) pp. 1237–1254.

Rudnicki, M. D. and Elderfield, H. 'A Chemical-Model of the Buoyant and Neutrally Buoyant Plume above the Tag Vent Field, 26 Degrees-N, Mid-Atlantic Ridge'. *Geochimica et Cosmochimica Acta* (1993). **57**(13) pp. 2939–2957.

Rue, E. L. and Bruland, K. W. 'Complexation of Fe(III) by natural organic ligands in the Central North Pacific as determined by a new competitive ligand equilibration adsorptive cathodic stripping voltammetric method'. *Marine Chemistry* (1995). **50**(1-4) pp. 117–138.

Rue, E. L. and Bruland, K. W. 'The role of organic complexation on ambient iron chemistry in the equatorial Pacific Ocean and the response of a mesoscale iron addition experiment'. *Limnology and Oceanography* (1997). **42**(5) pp. 901–910.

Ruzic, I. 'Theoretical aspects of the direct titration of natural waters and its information yield for trace metal speciation'. *Analytica Chimica Acta* (1982). **140**(1) pp. 99–113.

Sander, S. and Koschinsky, A. 'Onboard-ship redox speciation of chromium in diffuse

hydrothermal fluids from the North Fiji Basin'. *Marine Chemistry* (2000). **71**(1) pp. 83–102.

Sander, S. G. and Koschinsky, A. 'Metal flux from hydrothermal vents increased by organic complexation'. *Nature Geoscience* (2011). **4**(3) pp. 145–150.

Sands, C. M., Connelly, D. P., Statham, P. J. and German, C. R. 'Size fractionation of trace metals in the Edmond hydrothermal plume, Central Indian Ocean'. *Earth and Planetary Science Letters* (2012). **319** pp. 15–22.

Sanudo-Wilhelmy, S. A., Rivera-Duarte, I. and Flegal, A. R. 'Distribution of colloidal trace metals in the San Francisco Bay estuary'. *Geochimica et Cosmochimica Acta* (1996). **60**(24) pp. 4933–4944.

Schaller, T., Morford, J., Emerson, S. R. and Feely, R. A. 'Oxyanions in metalliferous sediments: tracers for paleoseawater metal concentrations?' *Geochimica et Cosmochimica Acta* (2000). **64**(13) pp. 2243–2254.

Schlosser, C., De La Rocha, C. L., Streu, P. and Croot, P. L. 'Solubility of iron in the Southern Ocean'. *Limnology and Oceanography* (2012). **57**(3) p. 684.

Schlosser, C., Rocha, C. D. L. and Croot, P. 'Effects of iron surface adsorption and sample handling on iron solubility measurements'. *Marine Chemistry* (2011). **127**(1 - 4) pp. 48 – 55.

Sedwick, P., Mcmurtry, G. and Macdougall, J. 'Chemistry Of Hydrothermal Solutions From Pele Vents, Loihi Seamount, Hawaii'. *Geochimica et Cosmochimica Acta* (1992). **56**(10) pp. 3643–3667.

Seyfried, W. and Ding, K. 'The effect of redox on the relative solubilities of copper and iron in Cl-bearing aqueous fluids at elevated temperatures and pressures: An experimental study with application to subseafloor hydrothermal systems'. *Geochimica et Cosmochimica Acta* (1993). **57**(9) pp. 1905–1917.

Shaked, Y., Kustka, A. and Morel, F. 'A general kinetic model for iron acquisition by eukaryotic phytoplankton'. *Limnology and Oceanography* (2005). **50**(3) pp. 872–882.

Shaked, Y. and Lis, H. 'Disassembling iron availability to phytoplankton'. *Frontiers in Microbiology* (2012). **3**.

Sherrell, R. M., Field, M. P. and Ravizza, G. 'Uptake and fractionation of rare earth elements on hydrothermal plume particles at 9 45' N, East Pacific Rise'. *Geochimica et Cosmochimica Acta* (1999). **63**(11) pp. 1709–1722.

Shi, D., Xu, Y., Hopkinson, B. M. and Morel, F. M. M. 'Effect of Ocean Acidification on Iron Availability to Marine Phytoplankton'. *Science* (2010). **327**(5966) pp. 676–679.

Statham, P., Yeats, P. and Landing, W. 'Manganese in the eastern Atlantic Ocean: processes influencing deep and surface water distributions'. *Marine Chemistry* (1998). **61**(1) pp. 55–68.

Statham, P. J., German, C. R. and Connelly, D. P. 'Iron (II) distribution and oxidation kinetics in hydrothermal plumes at the Kairei and Edmond vent sites, Indian Ocean'. *Earth and Planetary Science Letters* (2005). **236** p. 588.

Statham, P. J., Jacobson, Y. and van den Berg, C. M. G. 'The measurement of organically complexed Fe-II in natural waters using competitive ligand reverse titration'. *Analytica Chimica Acta* (2012). **743** pp. 111–116.

Staudigel, H., Hart, S. R., Koppers, A. A., Constable, C., Workman, R., Kurz, M. and Baker, E. T. 'Hydrothermal venting at Vailulu'u Seamount: The smoking end of the Samoan chain'. *Geochemistry, Geophysics, Geosystems* (2004). **5**(2).

Stock, M. J. *A Preliminary Petrological Investigation of the JC42 (East Scotia Ridge) Rocks.* Master's thesis, University of Southampton, National Oceanography Centre Southampton (2012).

Stockdale, A., Tipping, E., Hamilton-Taylor, J. and Lofts, S. 'Trace metals in the open oceans: speciation modelling based on humic-type ligands'. *Environmental Chemistry* (2011). **8**(3) pp. 304–319.

Sugie, K., Nishioka, J., Kuma, K., Volkov, Y. N. and Nakatsuka, T. 'Availability of particulate Fe to phytoplankton in the Sea of Okhotsk'. *Marine Chemistry* (2013).

Sutherland, F. L. 'Dispersal of Pumice, Supposedly from the 1962 South Sandwich Islands Eruption, on Southern Australian Shores'. *Nature* (1965). **207** pp. 1332–1335.

Tagliabue, A., Bopp, L., Dutay, J. C., Bowie, A. R., Chever, F., Jean-Baptiste, P., Bucciarelli, E., Lannuzel, D., Remenyi, T., Sarthou, G., Aumont, O., Gehlen, M. and Jeandel, C. 'Hydrothermal contribution to the oceanic dissolved iron inventory'. *Nature Geoscience* (2010). **3**(4) pp. 252–256.

Thomas, C., Livermore, R. and Pollitz, F. 'Motion of the Scotia Sea plates'. *Geophysical Journal International* (2003). **155**(3) pp. 789–804.

Toner, B. M., Kafra, S. C. and Manganini, S. J. 'Preservation of iron(II) by carbon-rich matrices in a hydrothermal plume'. *Nature Geoscience* (2009). **2** p. 197.

Trocine, R. P. and Trefry, J. H. 'Distribution and chemistry of suspended particles from an active hydrothermal vent site on the Mid-Atlantic Ridge at 26 °N'. *Earth and Planetary Science Letters* (1988). **88**(1) pp. 1–15.

Turner, J. *Buoyancy Effects in Fluids.* Cambridge University Press (1973).

Urabe, T., Baker, E., Ishibashi, J., Feely, R., Marumo, K., Massoth, G., Maruyama, A., Shitashima, K., Okamura, K., Lupton, J. et al. 'The effect of magmatic activity on hydrothermal venting along the superfast-spreading East Pacific Rise'. *Science* (1995). **269**(5227) pp. 1092–1095.

Ussher, S. J., Achterberg, E. P., Sarthou, G. R., Laan, P., de Baar, H. J. W. and

Worsfold, P. J. 'Distribution of size fractionated dissolved iron in the Canary Basin'. *Marine Environmental Research* (2010). **70**(1) pp. 46–55.

Van Den Berg, C. M. G. 'Determination of Copper Complexation with Natural Organic Ligands in Sea Water by Equilibration with Manganese Di Oxide 1. Theory'. *Marine Chemistry* (1982). **11**(4) pp. 307–322.

Van Den Berg, C. M. G. 'Evidence for organic complexation of iron in seawater'. *Marine Chemistry* (1995). **50**(1-4) pp. 139–157.

van den Berg, C. M. G. 'Chemical speciation of iron in seawater by cathodic stripping voltammetry with dihydroxynaphthalene'. *Analytical Chemistry* (2006). **78**(1) pp. 156–163.

Von Damm, K. 'Seafloor hydrothermal activity: black smoker chemistry and chimneys'. *Annual Review of Earth and Planetary Sciences* (1990). **18** p. 173.

Von Damm, K. 'Controls on the chemistry and temporal variability of seafloor hydrothermal fluids'. *Geophysical Monograph Series* (1995). **91** pp. 222–247.

Von Damm, K. L., Buttermore, L. G., Oosting, S. E., Bray, A. M., Fornari, D. J., Lilley, M. D. and Shanks, W. C. 'Direct observation of the evolution of a seafloor 'black smoker' from vapor to brine'. *Earth and Planetary Science Letters* (1997). **149**(1-4) pp. 101–111.

Von Damm, K. L., Edmond, J. M., Grant, B., Measures, C. I., Walden, B. and Weiss, R. F. 'Chemistry of submarine hydrothermal solutions at 21 °N, East Pacific Rise'. *Geochimica et Cosmochimica Acta* (1985). **49**(11) pp. 2197–2220.

Wang, H., Yang, Q., Ji, F., Lilley, M. D. and Zhou, H. 'The geochemical characteristics and Fe(II) oxidation kinetics of hydrothermal plumes at the Southwest Indian Ridge'. *Marine Chemistry* (2012). **134** pp. 29–35.

Wang, W.-X. and Dei, R. C. 'Bioavailability of iron complexed with organic colloids to the cyanobacteria Synechococcus and Trichodesmium'. *Aquatic Microbial Ecology* (2003). **33**(3) pp. 247–259.

Welhan, J. and Craig, H. *Methane, hydrogen and helium in hydrothermal fluids at 21 N on the East Pacific Rise*, volume 12 of *NATO conference series. IV, Marine sciences*. Plenum Press, New York, N.Y. (1983).

Welhan, J. A. 'Origins of methane in hydrothermal systems'. *Chemical Geology* (1988). **71**(1) pp. 183–198.

Wells, M. 'Manipulating iron availability in nearshore waters'. *Limnology and Oceanography* (1999). **44**(4) pp. 1002–1008.

Wheat, G. C., Feely, R. A. and Mottl, M. J. 'Phosphate removal by oceanic hydrothermal processes: An update of the phosphorus budget in the oceans'. *Geochimica et Cosmochimica Acta* (1996). **60**(19) pp. 3593–3608.

Wilkin, R., Barnes, H. and Brantley, S. 'The size distribution of framboidal pyrite in

modern sediments: An indicator of redox conditions'. *Geochimica et Cosmochimica Acta* (1996). **60**(20) pp. 3897–3912.

Witter, A. E., Hutchins, D. A., Butler, A. and Luther, G. W. 'Determination of conditional stability constants and kinetic constants for strong model Fe-binding ligands in seawater'. *Marine Chemistry* (2000). **69**(1-2) pp. 1–17.

Witter, A. E. and Luther, G. W. 'Variation in Fe-organic complexation with depth in the Northwestern Atlantic Ocean as determined using a kinetic approach'. *Marine Chemistry* (1998). **62** pp. 241 – 258.

Wu, J., Boyle, E., Sunda, W. and Wen, L. S. 'Soluble and colloidal iron in the oligotrophic North Atlantic and North Pacific'. *Science* (2001). **293**(5531) pp. 847–849.

Wu, J. and Luther, G. W. 'Complexation of Fe(III) by natural organic ligands in the Northwest Atlantic Ocean by a competitive ligand equilibration method and a kinetic approach'. *Marine Chemistry* (1995). **50**(1-4) pp. 159–177.

Wu, J., Wells, M. L. and Rember, R. 'Dissolved iron anomaly in the deep tropical-subtropical Pacific: Evidence for long-range transport of hydrothermal iron'. *Geochimica et Cosmochimica Acta* (2011). **75**(2) pp. 460–468.

Yang, K. and Scott, S. D. 'Magmatic degassing of volatiles and ore metals into a hydrothermal system on the modern sea floor of the eastern Manus back-arc basin, western Pacific'. *Economic Geology* (2002). **97**(5) pp. 1079–1100.

Yücel, M., Gartman, A., Chan, C. S. and Luther, G. 'Hydrothermal vents as a kinetically stable source of iron-sulphide-bearing nanoparticles to the ocean'. *Nature Geoscience* (2011). **4**(6) pp. 367–371.

Yücel, M. and Luther, G. W. 'Temporal trends in vent fluid iron and sulfide chemistry following the 2005/2006 eruption at East Pacific Rise, 9 ° 50âĂš N'. *Geochemistry, Geophysics, Geosystems* (2013).

Zeng, Z., Wang, X., Zhang, G., Yin, X., Chen, D. and Wang, X. 'Formation of Fe-oxyhydroxides from the East Pacific Rise near latitude 13 ° N: Evidence from mineralogical and geochemical data'. *Science in China Series D: Earth Sciences* (2008). **51**(2) pp. 206–215.